Fabrication of the 6.5 m primary mirror for the first Magellan Telescope

December 23, 1998

Steward Observatory Mirror Lab
University of Arizona

1. Project summary

The first Magellan primary mirror was cast, generated and polished by the Steward Observatory Mirror Lab during the period February 1994 - November 1998. The casting procedure is described by Olbert *et al.*[1] Generating and polishing procedures were similar to those used for the MMT primary mirror and described by Martin *et al.* (1997).[2] This report documents the quality of the finished mirror in terms of mechanical geometry, surface finish, figure accuracy and inferred image quality.

The mirror promises excellent performance. The structure is sound and has the superb mechanical and thermal characteristics of the honeycomb sandwich. The mirror is diffraction-limited (Strehl ratio > 0.8) down to $\lambda = 400$ nm, and at 500 nm focuses 80% of the light into a diameter well under $0.1''$.

We generated and polished the rear surface and edges with the mirror supported by the "spider" handling fixture attached to the front surface. We used the Large Optical Generator (LOG) for all generating and lapping operations. We chose the position of the mechanical axis to match the centroid of a set of 30 rib intersections distributed symmetrically over the full mirror. We measured the radial positions of these rib intersections by viewing them through index matching oil with a CCD camera which was attached to the generating spindle. We chose the tilt of the mechanical axis to minimize wedge in the backplate, as determined by ultrasonic thickness measurements at a set of 60 cells. We generated and polished the rear surface and all four edges (inner and outer, top and bottom) at this time.

We marked the locations and orientations of the support load spreaders by grinding shallow rings 1 mm in diameter with a dremel tool attached to the generating spindle. We centered the pattern of load spreader locations at the mechanical axis and chose its rotation angle to give the best average agreement with a set of 84 rib intersections. We bonded the load spreaders to the rear surface with Dow Corning Q3-6093 silicone adhesive, then turned the mirror over and set it on its polishing support.

We generated the front surface with a sequence of diamond wheels: a cup wheel with 30 mesh diamonds in a metal bond, the same wheel with 100 mesh diamonds in a metal bond, and a spherical wheel with 120 mesh diamonds in a resin bond. We monitored faceplate thickness with the ultrasonic gauge and overall thickness with calipers, and measured the surface profile using the LOG as a profilometer. The accuracy of this measurement is limited to that of the LOG's motion, on the order of 10 microns rms.

On completion of generating, we installed the 1.2 m stressed lap and started loose-abrasive grinding in March 1998. We placed small ceramic tiles on the pitch and used aluminum oxide abrasives of 25 and 9 micron. The initial optical measurements were made with an IR interferometer and null lens after just enough lapping to achieve continuous interference fringes. They showed a surface error of 70 microns peak-to-valley, dominated by a trefoil error of 50 microns peak-to-valley. We believe this was caused by flexure of the turntable bearing under the uneven load of the mirror and cell. We were able to remove it rapidly by varying the lap pressure dynamically.

In May we removed the ceramic tiles, replaced the pitch, and started polishing. We used, at different times, bare pitch and thin plastic pads on pitch. We also used cerium oxide and rouge as the abrasive at different times. We found that bare pitch with rouge gave the best surface finish (microroughness) and used that combination for the final few weeks.

We made the first measurements at visible wavelength in June. All visible measurements were made with a 531 nm laser interferometer and a refractive null lens. The mirror was figured to match a template defined by a computer-generated hologram. Measurements of the hologram revealed a substantial error in the null lens (290 parts per million in conic constant). We are still trying to determine the source of that error.

We used the stressed lap to remove both axisymmetric and asymmetric large-scale figure errors and to obtain passive smoothing on scales less than about 10 cm. We also ran axisymmetric strokes with passive laps between 10 cm and 30 cm diameter to remove narrow high zones. We reached the final accuracy in November 1998.

2. Specifications

2.1 Prescription

The optical prescription is a paraboloid. For purposes of tolerance analysis, we treat it as a conic section defined by the radius of curvature R and conic constant k. The surface height z as a function of distance r from the axis of symmetry is

$$z(r) = \frac{r^2}{R + \sqrt{R^2 - (k+1)r^2}}. \tag{1}$$

The values and tolerances of the radius of curvature and conic constant are given by the Technical Specifications and Requirements[3]:

$$R = 16256 \pm 3 \text{ mm}, \tag{2}$$

$$k = -1.0000 \pm 0.0002, \tag{3}$$

and the errors in R and k must satisfy

$$\left|\Delta R + (3.2\times10^5 \text{mm})\Delta k\right| < 40 \text{ mm}. \tag{4}$$

The last condition constrains the conic error to roughly ± 0.00012.

2.2 Figure error

The figure specification is given by a wavefront structure function $\delta^2(r)$, the mean square wavefront difference between points in the aperture as a function of separation r. It is the structure function produced by the standard model of atmospheric seeing, with two modifications. The standard atmospheric structure function is

$$\delta^2 = \left(\frac{\lambda}{2\pi}\right)^2 6.88\left(\frac{r}{r_0}\right)^{5/3}, \tag{5}$$

where r_0 is the Fried parameter, related to image FWHM θ as

$$\theta = 0.980\left(\frac{\lambda}{r_0}\right). \tag{6}$$

The first modification tightens the specification at large separations by removing that part of the atmospheric structure function corresponding to mean wavefront tilt. (This is done because autoguiding will remove mean tilt, or image motion, in the telescope, and the laboratory figure measurements are insensitive to it.) Hufnagel[4] gives an approximate expression for this correction, which depends only on telescope diameter D. The second modification is a relaxation at small separations corresponding to scattering a fraction L of the light outside of the seeing disk. The scattering loss is related to the small-scale rms phase error σ as

$$L = 1 - e^{-\sigma^2}. \tag{7}$$

The full specification is then

$$\delta^2 = \left(\frac{\lambda}{2\pi}\right)^2 \left\{ 6.88 \left(\frac{r}{r_0}\right)^{5/3} \left[1 - 0.975 \left(\frac{r}{D}\right)^{1/3} \right] + 2\sigma^2 \right\}. \tag{8}$$

The two parameters that fix its amplitude are

$$r_0 = 1.18 \text{ m}, \tag{9}$$

$$L = 0.015, \tag{10}$$

both defined at $\lambda = 500$ nm. This specification is plotted along with the measured structure functions in Figures 4 and 8.

2.3 Clear aperture

The clear aperture is defined as the annular region with

$$\text{ID} = 923 \text{ mm}, \tag{11}$$

$$\text{OD} = 6478 \text{ mm}. \tag{12}$$

The structure function is evaluated over this clear aperture, which extends to within about 11 mm of each edge of the polished surface.

2.4 Mechanical dimensions

Mechanical dimensions are given by drawing 1168, Rev. C. The following tolerances are listed in the Technical Specifications and Requirements.

1. centration of optical axis with respect to mechanical center: 1 mm
2. vertex thickness: 385.1 ± 0.5 mm
3. wedge angle: 30″

3. Conventions and notation

3.1 Orientation of coordinates

All figure maps show the optical surface as viewed face-on with the mirror horizon-pointing. Rotation angles quoted throughout this report use the same view. The x and y axes are in the usual sense, x increasing to the right and y increasing upward. Angles increase counter-clockwise from 0 in the positive x direction. This convention holds for descriptions of the back plate as well as the optical surface, i. e. one views the back plate through the mirror.

3.2 Zernike polynomial coefficients

We use Zernike polynomial coefficients to describe the aberrations of focus, astigmatism, coma and spherical aberration. Throughout this report, amplitudes of these aberrations are given in terms of the Zernike coefficient of surface error. The symbols used for coefficients and the associated polynomials are given in Table 1. The polynomials are expressed as functions of the dimensionless radius ρ normalized to 1 at the edge of the mirror.

Table 1. Zernike polynomial coefficients

aberration	coefficient	polynomial
focus	R_2^0	$2\rho^2 - 1$
astigmatism (0°)	R_2^2	$\rho^2\cos(2\theta)$
astigmatism (45°)	R_2^{-2}	$\rho^2\sin(2\theta)$
coma (0°)	R_3^1	$(3\rho^3 - 2\rho)\cos\theta$
coma (90°)	R_3^{-1}	$(3\rho^3 - 2\rho)\sin\theta$
spherical aberration	R_4^0	$6\rho^4 - 6\rho^2 + 1$

We sometimes describe astigmatism by the combined Zernike coefficient

$$R_{22} = [(R_2^2)^2 + (R_2^{-2})^2]^{1/2} \tag{13}$$

and the rotation angle

$$\theta_{22} = \frac{1}{2}\text{atan}\left(\frac{R_2^{-2}}{R_2^2}\right) \tag{14}$$

at which the high occurs.

Spherical aberration is equivalent to a change in conic constant; the relation between Zernike coefficient R_4^0 and conic change Δk is

$$\Delta k = 6144 f^3 \frac{R_4^0}{D}, \tag{15}$$

where $f = 1.25$ is the focal ratio and $D = 6.5$ m is the diameter. If Δk is expressed in parts per million,

$$\frac{\Delta k}{1 \text{ ppm}} = 1.846 \left(\frac{R_4^0}{1 \text{ nm}} \right). \tag{16}$$

Positive spherical aberration corresponds to a less negative conic constant.

3.3 Uncertainties

All uncertainties quoted in this report represent our best estimate of two standard deviations. In other words, a value quoted as $x \pm \Delta x$ means that we estimate that the value lies within that range with 95% probability. This interpretation is valid only for anticipated sources of error.

4. Procedure for figure measurements and analysis

4.1 Measurement system

Optical tests were performed from the center of curvature with the mirror mounted on its polishing support cell. The measurement system comprises a Shack-cube interferometer, a stabilized frequency-doubled YAG laser at 531 nm, an imaging system with CCD camera, and an Offner-type refractive null corrector. The measurement is made by phase-shifting interferometry, in which the phase variations across the pupil are determined from a series of intensity patterns with phase shifts between them. The Shack cube is translated with piezoelectric transducers to introduce a phase shift, constant across the pupil, between successive intensity patterns. Intensity patterns are recorded at a 200 Hz frame rate, and reduced to phase measurements using a commercial system from Phase Shift Technology. The CCD camera has square pixels and a resolution of 197 pixels across the mirror in the full-aperture measurement.

4.2 Measurement noise

Any single phase map contains random errors due to local air turbulence (seeing) and vibration. They are reduced by taking many phase maps and averaging. The error in an individual full-aperture map, computed as the difference between that map and the average of all maps, is 40-60 nm rms. These errors average out as random noise, with the possible exception of large-scale features which may persist for 10 s or more and therefore correlate among two or more maps. The full-aperture map presented here is an average of 150 individual maps, while the subaperture maps are averages of 50 maps. We estimate that the contribution of seeing and vibration in the average map is less than 10 nm rms surface error. Some of this is in the form of astigmatism, which is ignored. The contribution to the structure function at the critical 5-10 cm separations is not significant.

4.3 Mirror support

The mirror is supported on passive hydraulic cylinders that match the telescope support system in location and force. Differences between the support mechanisms in the polishing cell and the telescope cell are expected to cause force differences on the order of 10 N. Certain support units exhibited inconsistencies of up to 30 N from day to day, apparently because of friction in the vertical motion of the unit. These force variations cause significant changes in astigmatism and smaller changes in other flexible bending modes. Most of their effects will be removed through the empirical optimization of support forces in the telescope cell.

Plastic skirts used to collect polishing slurry at the inner and outer edges of the mirror were removed for all tests, so the only mechanical contact with the mirror was through the 104 supports and the 3 tangent rods that provide a kinematic constraint against translation and rotation.

4.4 Thermal equilibration

Temperature differences on the order of 1 K can develop within the mirror during a polishing run, causing thermo-elastic deflections of the mirror. We ventilate the mirror after each polishing run, reducing the temperature differences to about 0.2 K, roughly equal to the sensitivity of the temperature measurement system in the mirror and polishing cell. All figure measurements reported here were made after at least 24 hours of passive equilibration following the ventilation, adequate to erase any effects of the final polishing run.

4.5 Removal of test optics errors

We determine the errors in the test optics by measuring a computer-generated hologram (the primary hologram) that mimics the ideal primary mirror. The principles and procedure are described in Section 7.3. We subtract a Zernike polynomial representation of the primary hologram map from all maps of the primary mirror. The map of the primary hologram contains spherical aberration with a Zernike coefficient of -155 nm, equivalent to an error in conic constant of -290 parts per million (ppm). This is believed to come from refractive index variations in the large relay element of the null lens. The relay lens has been measured with a hologram as described in Section 7.5. Its transmitted wavefront error is consistent with the error in spherical aberration seen in the map of the primary hologram.

As a separate and independent verification, we plan to remeasure the mirror with a new interferometer before the mirror is removed from the polishing cell. The new interferometer will subsequently be used for all optical testing after the mirror is installed in the telescope cell. It operates at a different wavelength (633 nm) and therefore requires a respacing of the null lens elements. The accuracy of the modified null lens will be verified with a new primary hologram.

4.6 Treatment of tilt, defocus and coma

The test optics are mounted in a stiff frame that is positioned relative to the mirror with remotely controlled translation and rotation stages. These stages are used to align the test optics in five degrees of freedom: horizontal and vertical translations and tilt in both directions. This alignment is adjusted to minimize tilt, defocus and coma in the reflected wavefront as judged by visual inspection of the interference pattern. Residual aberrations of these forms are subtracted from the measured phase map. The aberrations of tilt, defocus and coma are constrained by measured limits on wedge, radius of curvature and centration of the optical axis, respectively. These quantities are measured separately as described in Section 6.

4.7 Treatment of astigmatism and spherical aberration

We measured varying amounts of astigmatism throughout the fabrication process, including the final figure measurements. We believe the variations are related to support forces. The astigmatism varied in magnitude from about 200 to 400 nm among figure measurements made on different days after polishing was completed. These variations did not come from noise in the data, for the variations among maps measured on a given day were much smaller. We estimated the support forces necessary to cause this much astigmatism from a modal analysis of the BCV finite-

element analysis.[5,6] Astigmatism with a Zernike coefficient of 400 nm would be caused by an optimized set of forces whose extreme values are ±2 N, or by random force errors on the order of 14 N rms. In the telescope, astigmatism will be determined entirely by support forces rather than the relaxed mirror's figure.

Spherical aberration varied by about ±10 nm among measurements made after polishing was completed. The variation is probably caused by small temperature gradients. The final full-aperture map has 45 nm of spherical aberration, equivalent to an error of 80 parts per million in conic constant. Spherical aberration can be treated as an error in conic constant rather than a figure error.

We present full-aperture maps and structure functions with and without astigmatism and spherical aberration. The synthetic images are made from the maps with both aberrations subtracted.

4.8 Measured aperture

The physical size of the measured aperture is determined by placing fiducial markers at known locations on the mirror surface, and measuring their location in the image. We placed small annular markers at four positions near the edge, at a radius of 2.98 m. Scaling from the image coordinates of these markers to the edge of the image gives a diameter of 6.485 m between the centers of the outermost pixels in the full-aperture map. Since the pixels are 33 mm wide, the image covers a diameter of 6.518 m, 18 mm larger than the polished surface. This introduces some noise in the outer ring of pixels. We attempt to eliminate its effect on the structure function and point-spread function by sampling only inside the clear aperture.

4.9 Subaperture measurements

We measured three subapertures across the elevation axis. The resolution is 2.2 times that of the full-aperture map, limited by the need to maintain a certain intensity per pixel. We can shift the centroid of the interferometer's intensity pattern to each subaperture, but we cannot focus it to increase the intensity.

For off-axis subaperture measurements, alignment aberrations and astigmatism are indistinguishable from the spherical aberration due to the null lens. We therefore subtract focus, coma, astigmatism and spherical aberration from each subaperture map, and make no explicit correction for the null lens. In some cases this may cause an incomplete removal of null lens errors and/or an artificial reduction in large-scale aberrations, but it should have virtually no effect on the structure function at separations below about 10 cm.

The mapping from image to mirror coordinates is done as for the full-aperture maps, with four small fiducial markers placed at known positions in each subaperture. We verified that the measured aperture extends at least as far as the clear aperture, both by scaling from these fiducials and by placing other fiducial markers at the edge of the mirror and noting their appearance in the image.

4.10 Calculation of structure function

The wavefront structure function is defined as the mean square difference in wavefront error between randomly selected points as a function of their separation in the aperture. For comparison with the specification, we plot the square root of this quantity along with the corresponding curve for the specification.

To compute the structure function, we first define a 50×50 square grid of points over the aperture. The grid has uniform spacing in physical coordinates on the mirror. The subset of these points that lie on the mirror is the set of first points of pairs used to calculate the rms difference. Each first point is transformed to image coordinates (fractional pixels) using a magnification in each dimension based on the known size of the measured aperture. The wavefront error at each first point is interpolated bilinearly from the four pixels surrounding the transformed coordinates.

For each separation, the rms wavefront difference is calculated as follows. For each first point, five second points are chosen at the appropriate separation, in five directions at equal intervals of $72°$. We use five directions in order to avoid any symmetries of the mirror, supports, and camera. Each second point that lies on the mirror is transformed to image coordinates and its wavefront error is interpolated. The rms difference over all pairs is recorded.

We have performed numerical experiments to verify that the results of this calculation do not depend on arbitrary details such as the number of points or directions. There is, however, some smoothing caused by the interpolation. We have also calculated the structure function using discrete pixels, and therefore discrete separations, without interpolation. This method is probably more accurate but has several drawbacks related to the finite number of small separations. Only certain directions are sampled at small separations, and the method of binning (or not binning) separations strongly affects the plots. This method is more strongly affected by noise in single pixels.

We present structure functions calculated with and without interpolation. For the interpolated values, we use two separations per octave from 2.5 cm to 3.2 m for the full-aperture measurement, and from 1.25 cm to 1.6 m for the subaperture measurements. For the discrete-pixel calculations, we bin the separations into four bins per octave centered at 2.5 cm to 0.4 m for the full aperture and 1.25 cm to 0.2 m for the subaperture. (We skip the larger separations for this case because the calculation is slow, and the two methods differ most at small separations.) Some bins contain no separations.

5. Figure measurements

5.1 Full-aperture maps and structure functions

Figures 1-3 are gray-scale contour maps and synthetic interference patterns made from the full-aperture measurements. All measurements have been corrected for errors in the null lens as determined by the hologram. The three cases are: the original map including astigmatism and spherical aberration; the map with astigmatism subtracted; and the map with astigmatism and spherical aberration subtracted. The interference patterns are calculated for a wavelength of 531 nm and contain 10 waves of tilt. Table 2 gives statistics of the maps. Figure 4 shows the wavefront structure function, calculated over the clear aperture, for all three cases.

Table 2. Statistics of full-aperture maps

map	rms surface error	R_{22}	θ_{22}	R_4^0
original	110 nm	270 nm	–34°	40 nm
astigmatism subtracted	23 nm			40 nm
astigmatism and spherical aberration subtracted	14 nm			

5.2 Synthetic images

We calculated synthetic images from the map of Figure 3, with astigmatism and spherical aberration subtracted, using the clear aperture. The calculation covers a 4 arcsecond field, with sampling of 250 points across the clear aperture. Figure 5 shows the point-spread functions of the actual and perfect mirrors. Figure 6 shows encircled energy diagrams for the actual mirror and a perfect mirror, in perfect seeing and 0.25 arcsecond seeing. Seeing is included by convolving the mirror's PSF with that of the seeing, calculated from its structure function.

5.3 Subaperture maps and structure functions

Figure 7 shows the subaperture maps obtained with 15 mm pixels, 2.2 times the resolution of the full-aperture map. Focus, coma, astigmatism and spherical aberration have been subtracted. Table 3 gives the dimensions and rms surface errors, and Figure 8 shows the structure functions.

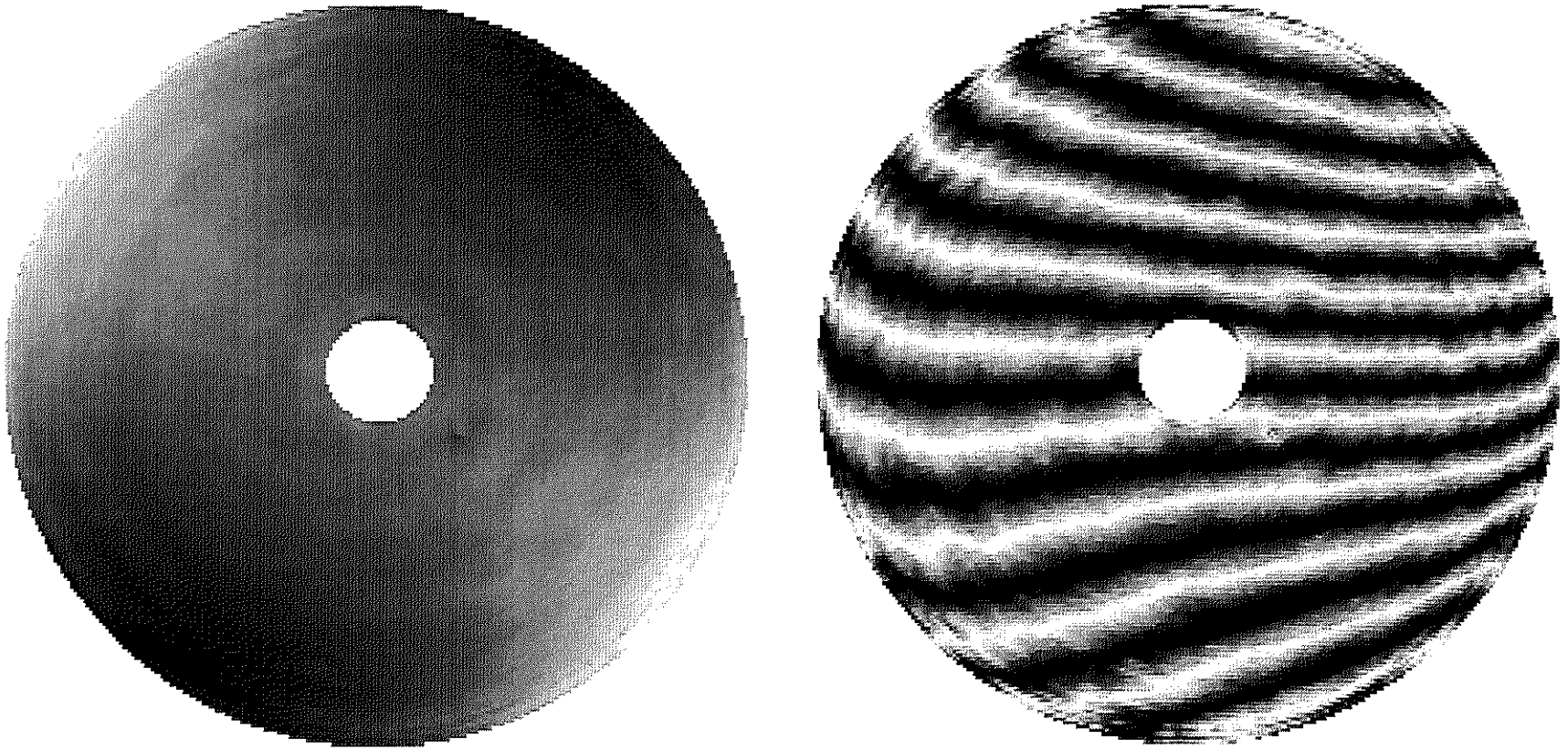

Figure 1. Gray-scale map of the mirror surface and synthetic interference pattern for the original map. The gray scale covers ±300 nm of surface.

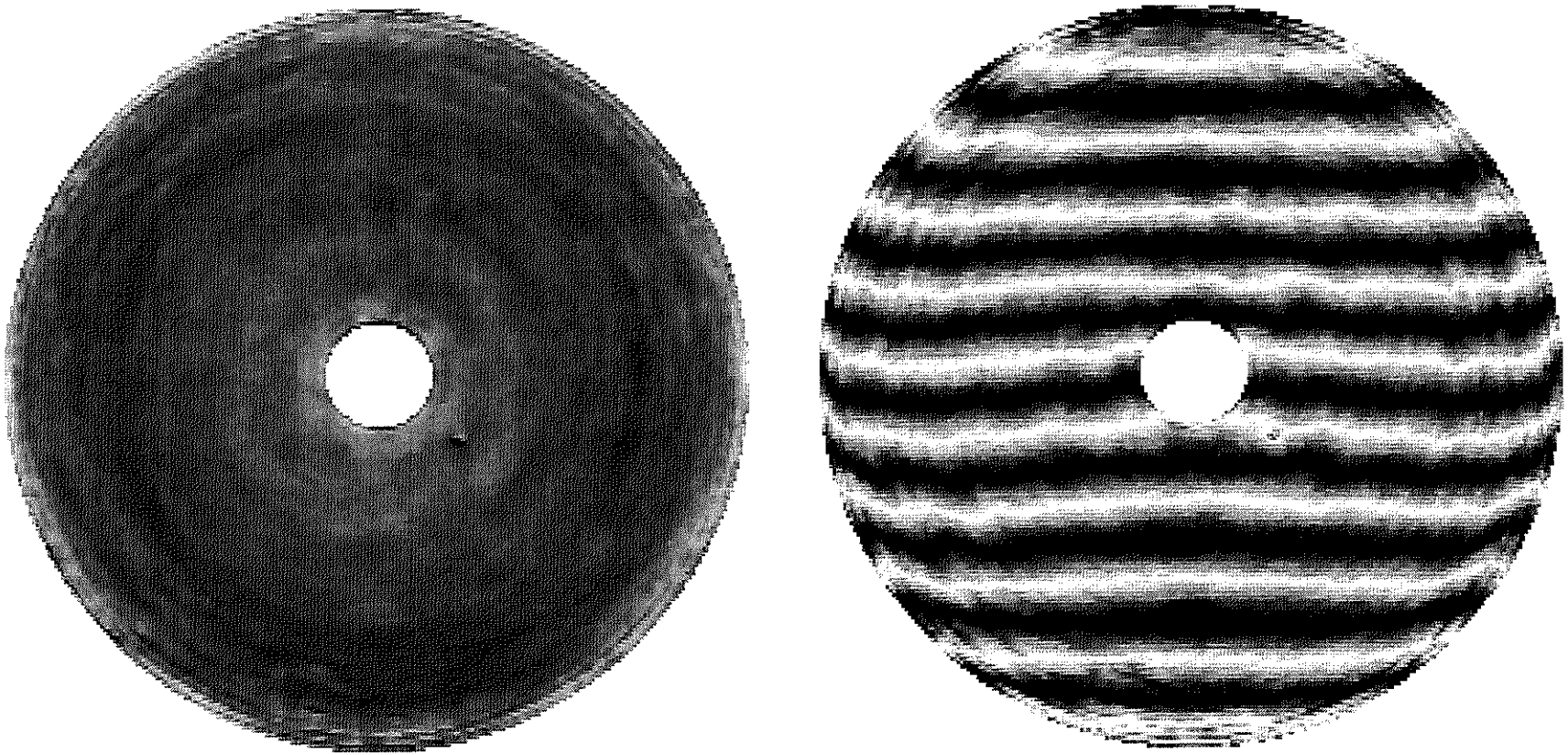

Figure 2. Gray-scale map of the mirror surface and synthetic interference pattern with astigmatism subtracted. The gray scale covers ±100 nm of surface.

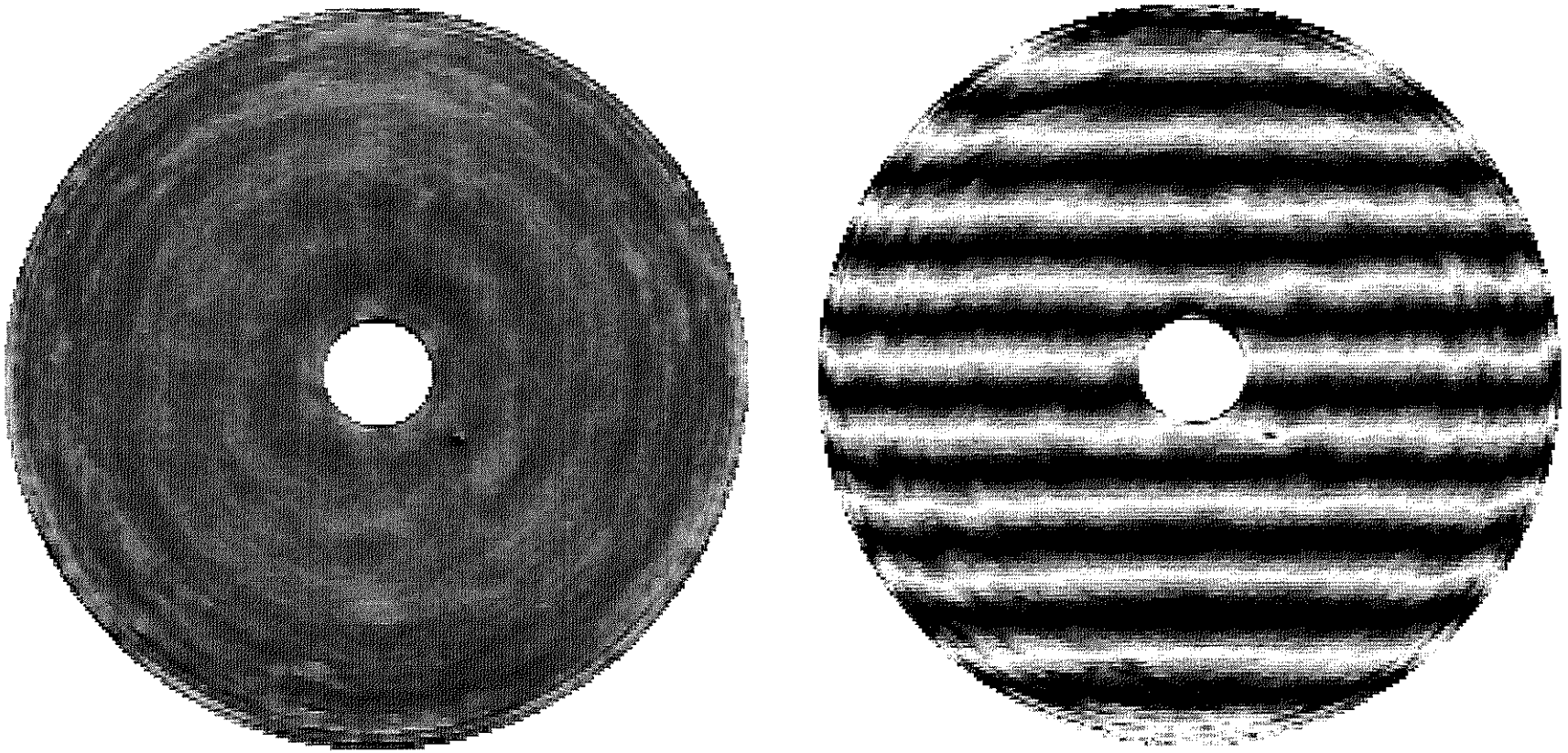

Figure 3. Gray-scale map of the mirror surface and synthetic interference pattern with astigmatism and spherical aberration subtracted. The gray scale covers ±100 nm of surface.

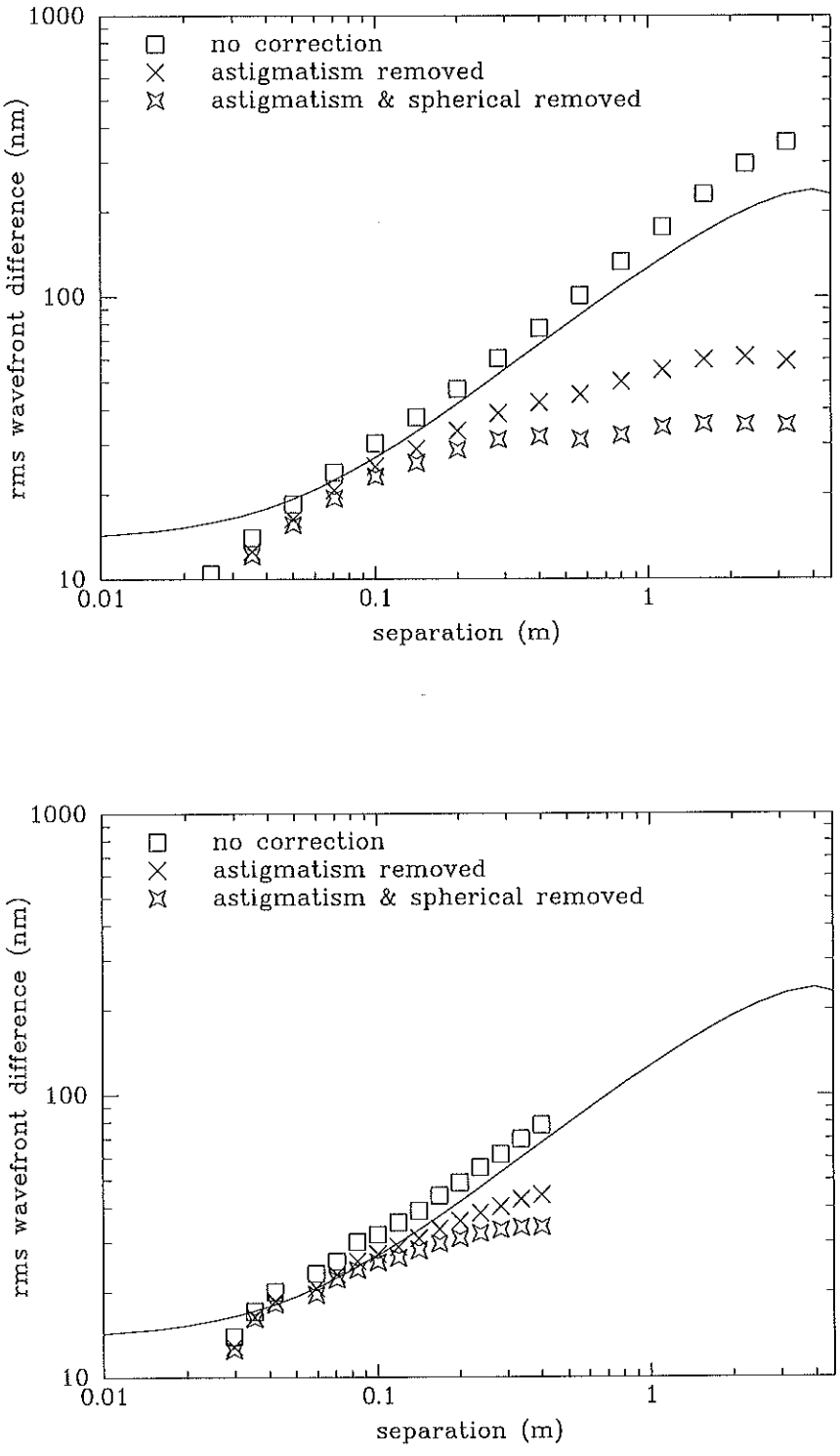

Figure 4. Square root of the wavefront structure function for the maps shown in Figures 1-3. Top: calculated at regular intervals in separation, with phase values interpolated. Bottom: calculated at discrete separations corresponding to the pixel spacing without interpolation, and binned with 4 bins per octave in separation. The curve is the goal.

Figure 5. Synthetic images at 0.5 micron for the actual mirror of Figure 3 (left) and a perfect mirror (right). The images are separated by 0.5 arcsecond.

Table 3. Statistics of subaperture maps

map	dimensions (H × V in m)	rms surface error
A	2.78 × 3.48	12 nm
B	2.89 × 3.52	13 nm
C	2.96 × 3.67	12 nm

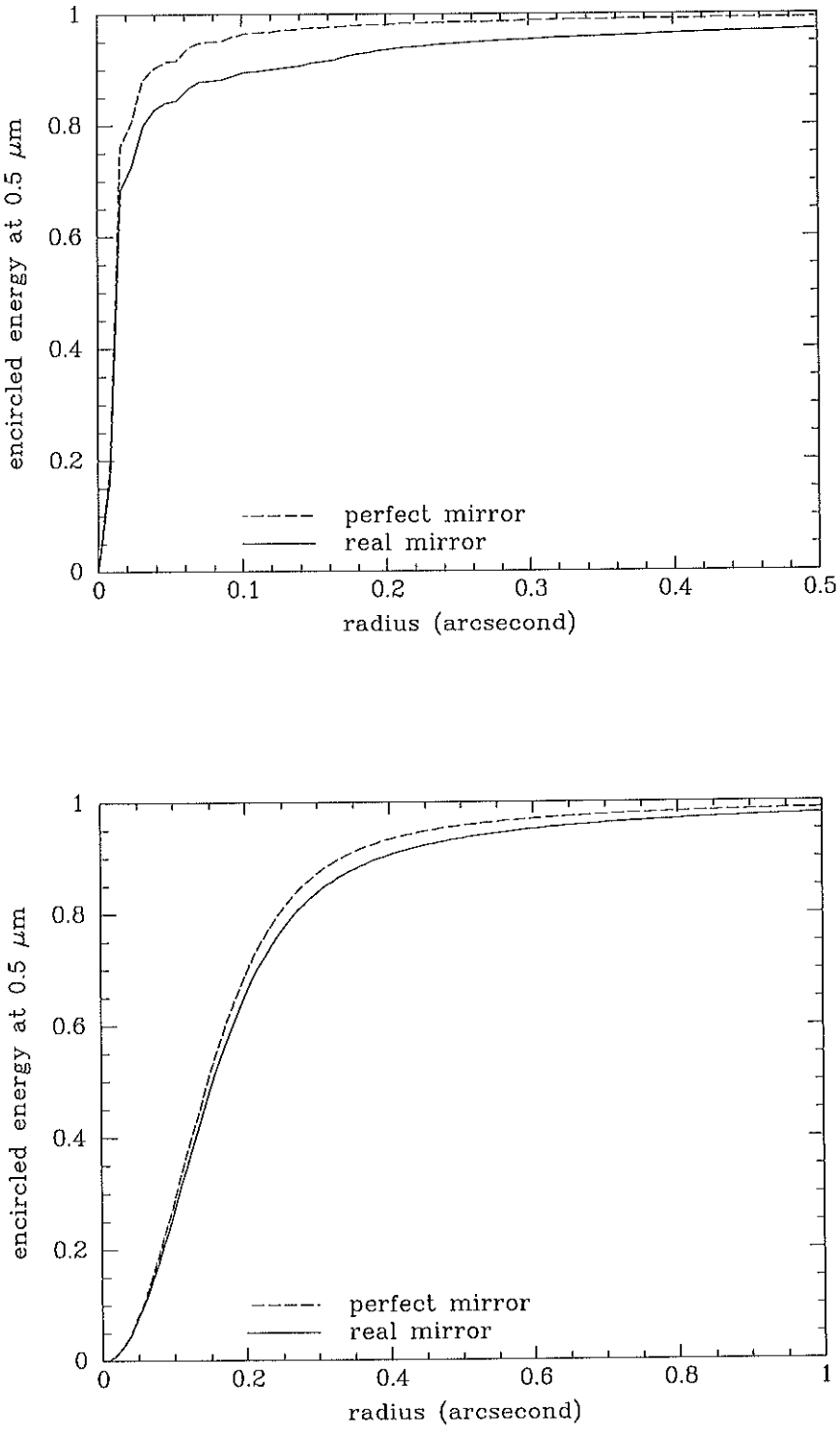

Figure 6. Encircled energy diagram with no seeing for the mirror of Figure 3 and a perfect mirror. Top: in perfect seeing. Bottom: in 0.25 arcsecond (FWHM) seeing.

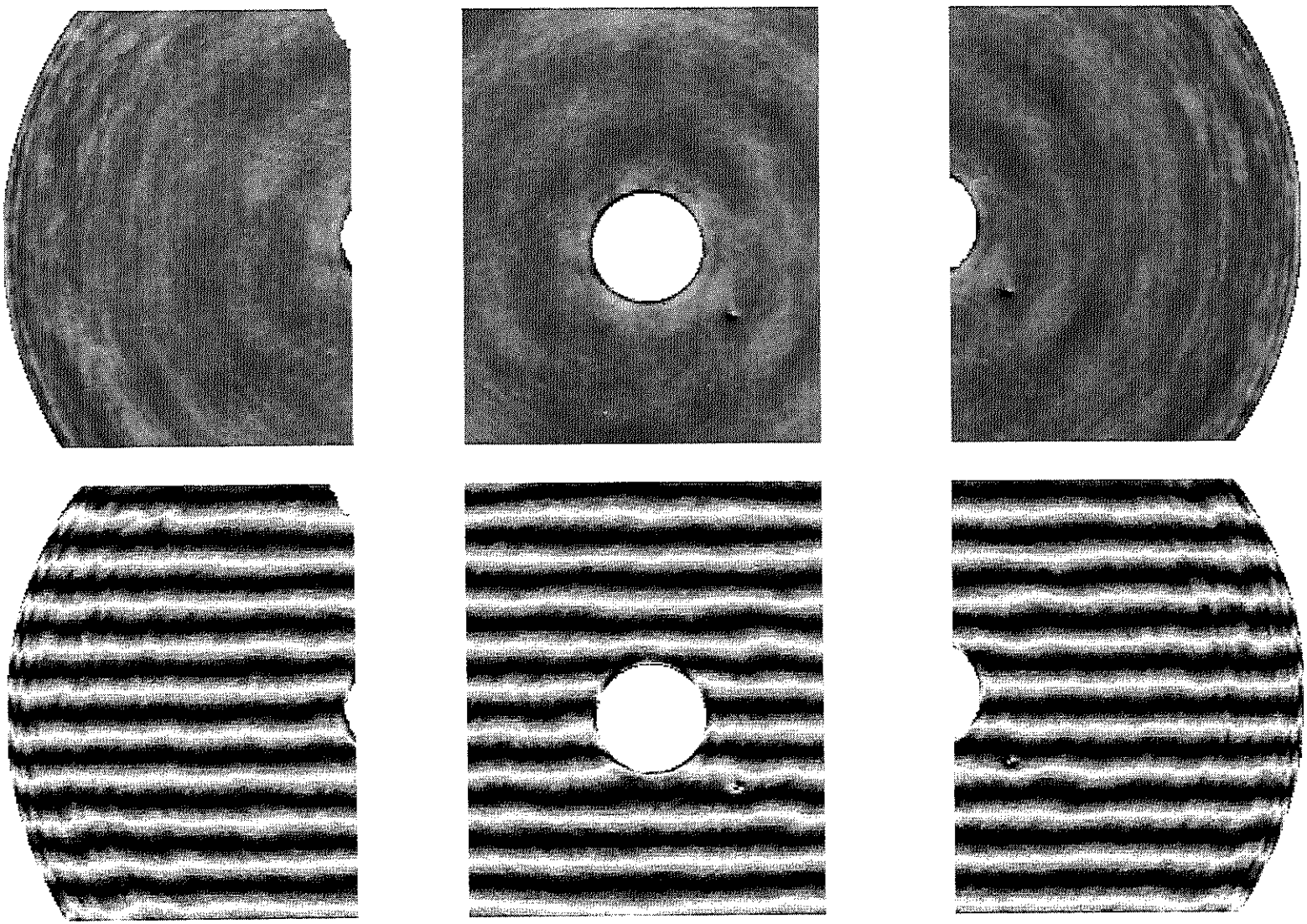

Figure 7. Gray-scale maps and synthetic interference patterns for three subapertures (A, B and C from left to right). The gray scale covers ±100 nm of surface. The interference pattern is calculated for a wavelength of 531 nm. The displays extend to the edges of the polished surface.

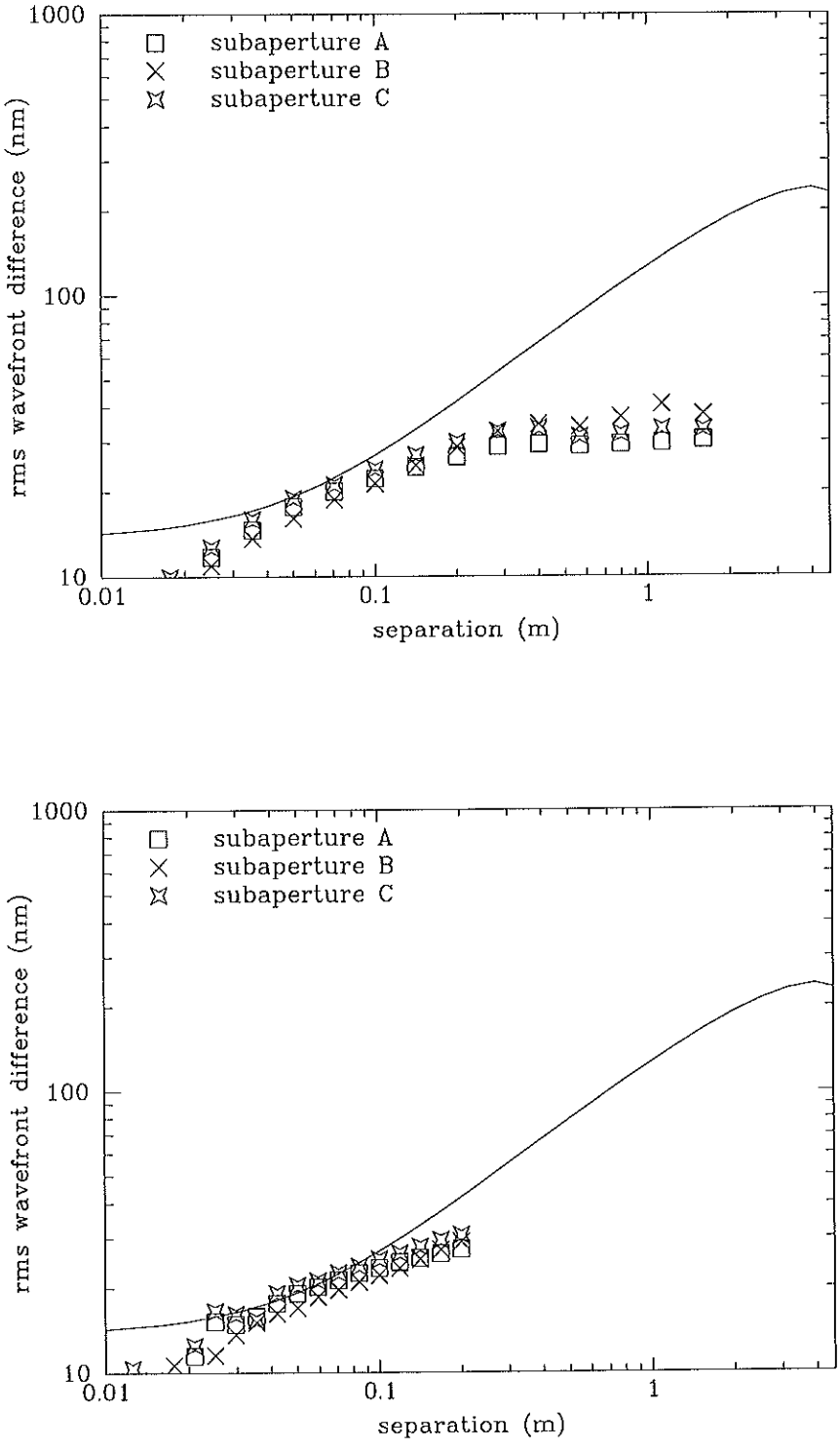

Figure 8. Square root of the wavefront structure function for the subaperture maps shown in Figure 7. Top: calculated at regular intervals in separation, with phase values interpolated. Bottom: calculated at discrete separations corresponding to the pixel spacing without interpolation, and binned with 4 bins per octave in separation. The curve is the goal.

6. Other measurements

6.1 Mechanical dimensions

We generated the mirror according to drawing 1168, Rev. C. Table 4 gives the finished dimensions, in inches to match the drawing. The inner and outer diameters, and bevel widths, match the drawing within the specified tolerances. The edge thickness given in drawing 1168, Rev. C fails to take account of the bevel. The correct value is 27.95 inches as listed in Table 4.

Table 4. Mechanical dimensions in inches

dimension	per drawing 1168, Rev. C	measured	uncertainty
front plate OD	256.40	256.42	0.01
back plate OD	256.40	256.42	0.01
front plate ID	35.00	34.97	0.005
back plate ID	37.00	36.97	0.005
polished surface OD	255.90	255.87	0.01
polished surface ID	35.50	35.45	0.01
edge thickness	27.950	27.970	0.002
wedge	0.0	0.005	0.002

The vertex thickness is calculated from the measured edge thickness and radius of curvature. Its value is 385.7 ± 0.1 mm, slightly over the specified thickness. The wedge angle is $4 \pm 2''$, well within the tolerance.

6.2 Faceplate thicknesses

We measured faceplate thicknesses with an ultrasonic gauge at 60 uniformly spaced cells. Table 5 gives the mean thickness, wedge, and radial variation for both faceplates. A positive radial variation means the outer edge is thicker. The values for the back plate are final values after loose-abrasive grinding. We last measured the front plate thickness after generating, and subtract the measured removal of 0.26 mm during loose-abrasive grinding to obtain the mean thickness listed in the table.

6.3 Radius of curvature

We measured the vertex radius of curvature with a steel tape certified by NIST. The vertex radius of curvature is defined as the distance from the paraxial center of curvature to the vertex of the primary mirror. Since neither the vertex nor the center of curvature present a mechanical refer-

Table 5. Faceplate thicknesses in mm

	mean	wedge (p-v)	rotation angle of maximum	radial variation (p-v)
front plate	29.3	0.1	−124°	0.8
back plate	26.7	0.3	65°	0.0

ence, we measure their separation indirectly by summing distances between intermediate surfaces.

The computer-generated hologram used to measure the null lens (see Section 7.3) is designed to return a null wavefront when it is placed at the paraxial center of curvature. We align the null lens at best focus of the primary mirror, as in the measurement of the primary mirror, and install the hologram mounted on a 5-axis stage. We adjust the stage to align the hologram to the null lens, thereby placing the hologram at the center of curvature. The lower reference is a two-ball locating jig that rests on the primary mirror surface near the edge of the center hole. We use the tape to measure from the 5-axis stage to the locating jig. The radius of curvature is the sum of this distance, the distance from the stage to the hologram, and the distance from the locating jig to the vertex, which is calculated from the approximate radius of curvature.

The final radius measurement was made on November 19, 1998. The result is

$$R = 16257.1 \pm 0.5 \text{ mm}. \tag{17}$$

6.4 Conic constant

The conic constant of the best-fit conic section is a sum of three terms:

1. spherical aberration in the final surface map;
2. correction for null lens error, based on the hologram;
3. correction for conic error caused by an error in radius of curvature.

The conic constant is sensitive to an error in the primary's radius of curvature because (a) the null lens and interferometer are positioned at best focus above the mirror, and (b) the test wavefront becomes more spherical as it propagates. The error in conic constant is related to the error in radius by

$$\frac{\Delta k}{k} = -\frac{\Delta R}{R}. \tag{18}$$

Table 6 gives the measured values and uncertainties for these terms. The uncertainty in spherical aberration for the final map is dominated by the presumably thermal variations in the actual mirror figure. The uncertainty in the hologram correction is discussed in Section 7.3. The uncertainty in the radius correction comes directly from the uncertainty in radius.

Table 6. Measurement of conic constant

term	R_4^0 (nm)	Δk (ppm)
uncorrected final map	-150 ± 10	-280 ± 20
hologram correction	155±40	290±70
radius correction	35±15	70±30
net error	40±40	80±80

Most of the spherical aberration in the final figure is due to an error in calculating the hologram correction, which was not caught until after polishing was completed. The hologram correction listed in Table 6 is the correct value.

From Table 6, the conic constant is

$$k = -0.99992 \pm 0.00008 . \tag{19}$$

If it were to turn out that the null lens is correct and the hologram is in error, then we would eliminate the hologram correction (but replace its uncertainty with that of the null lens, 110 ppm), and the conic constant would be

$$k' = -1.00021 \pm 0.00012 . \tag{20}$$

6.5 Centration of the optical axis

We determined the displacement of the optical axis relative to the mechanical axis (defined by the machined cylindrical surfaces at the outer edge of the mirror) by measuring the change in coma when the mirror is rotated around its mechanical axis. If the optical and mechanical axes were coincident, rotating the mirror would introduce no coma. If they are not, rotating the mirror 180° changes coma by an amount equal to twice the coma corresponding to the displacement of the two axes.

The interferometer is aligned with the mirror at the standard rotation angle (0°) and the mirror is measured, yielding coma coefficients $R_3^{\pm 1}\big|_0$. The mirror is then moved back to the turntable, rotated 180°, and returned to the test tower. Radial and vertical displacement are monitored with dial indicators to insure that the mechanical axis repeats within 0.1 mm. The mirror is tilted to obtain tilt-free fringes, but is not translated, and the interferometer is not moved. The mirror is then remeasured, yielding coma coefficients $R_3^{\pm 1}\big|_{180}$. The coma that would be seen if the interferometer were aligned with the mechanical axis, and the mirror at 0°, is half the difference of these two measurements:

$$R_3^{\pm 1}\Big|_m = \frac{R_3^{\pm 1}\Big|_0 - R_3^{\pm 1}\Big|_{180}}{2}. \tag{21}$$

These coefficients are related to the displacement of the optical axis by[7]

$$R_3^{1}\Big|_m = \frac{\Delta x}{384 f^3}, \tag{22}$$

$$R_3^{-1}\Big|_m = \frac{\Delta y}{384 f^3}, \tag{23}$$

where f is the focal ratio. A positive coefficient implies that the optical axis is displaced in the positive direction.

We made the final centration measurement on September 9, 1998. Further polishing after that date removed far too little glass to affect coma. Table 7 gives the measurements and inferred displacement of the optical axis. Values are given for the x and y components of coma and displacement, with uncertainty determined by repeating the procedure of rotating the mirror and measuring. The net displacement is given at the bottom.

Table 7. Measurement of decenter coma

	value		uncertainty	
parameter	x	y	x	y
$R_3^{\pm 1}\Big\|_0$ (μm)	0.03	0.10	0.3	0.3
$R_3^{\pm 1}\Big\|_{180}$ (μm)	−1.28	0.63	0.3	0.3
$R_3^{\pm 1}\Big\|_m$ (μm)	0.66	−0.26	0.2	0.2
Δx, Δy (mm)	0.49	−0.20	0.15	0.15
Δr (mm)	0.53			
θ	−22°			

6.6 Microroughness

We measured the microroughness at three locations on the mirror by making RTV replications and having them measured with a WYKO phase-shifting microscope interferometer. Three measurements were made at different positions on each 60 mm replication. The results are listed in Table 8, with locations given as rib intersections. All results are under the specified roughness of 20 Angstroms. The average roughness is 11 Angstroms.

Table 8. Microroughness measurements

rib intersection	radius (m)	sample 1 (Angstroms)	sample 2 (Angstroms)	sample 3 (Angstroms)	average (Angstroms)
F2/A45/A60	0.77	8.4	9.3	7.9	8.5
F8/A123/A133	1.92	9.9	8.0	12.7	10.2
F14/A167/A170	3.08	11.7	17.1	14.0	14.3
average					11.0

6.7 Scratches, digs and bubbles

We inspected the mirror thoroughly at completion of polishing. Detailed results including photographs of some defects will be given in a separate report.

There are no scratches in which the actual scratch width is greater than 200 microns. Two scratches include intermittent chips about 300 microns wide. A series of small fractures appears to be the remnant of a bad scratch that disappeared during loose-abrasive grinding. It comprises about 50 fractures on the order of 2 mm long, most of which lie within a 300 mm span. We ground out and bevelled one large scratch early in the polishing process, leaving a trough about 60 mm long and 40 mm wide. Some small fractures remain in the trough.

There are no digs greater than 200 microns wide.

The surface contains one bubble 13 mm wide and 8 bubbles between 3 mm and 6 mm wide. These were bevelled but not plugged. Three defects were ground out to leave spherical depressions between 3 mm and 10 mm wide. Three shallow spherical depressions about 6 mm wide remain from divots introduced to monitor removal during loose-abrasive grinding. We estimate that the surface contains about 150 bubble larger than 1 mm, and on the order of 1500 smaller bubbles that can be detected.

6.8 Internal flaws

Inspection and treatment of internal flaws is described in detail in a separate document. We briefly describe the two main categories of flaws here.

There are 12 regions with fractures in ribs and/or large chips removed from the inner surface of the back plate. We treated them by stop-drilling and grinding as necessary to prevent propagation.

A large number of cells exhibited a network of shallow fractures over the inner surface of the back plate. After polishing the back surface, when accurate visual inspection was possible, we removed the damaged layer by sandblasting until the worst remaining fractures were less than 2 mm deep.

7. Null lenses

7.1 Summary

We used two null lenses during the project: one for the 10.6 micron interferometer used during loose-abrasive grinding and early polishing, and one for the 531 nm interferometer used for the final figuring. With each null lens we measured a computer-generated hologram that was designed to mimic a perfect primary mirror. This hologram test is described by Burge[8,9] (Appendix 3). The measurement of the visible hologram indicated that the visible null lens produces a conic error of –290 ppm, outside the combined uncertainty of the null lens (110 ppm) and hologram (70 ppm). The final IR measurements were in better agreement with the visible hologram than with the visible null lens. We remeasured all mechanical dimensions of the null lens and found no error, but suspected that there might be a problem with the refractive index of the thick relay lens. We measured the wavefront transmitted by the relay lens with a separate relay hologram. This wavefront was found to have spherical aberration consistent with that seen in the hologram test of the full null lens, but the test does not establish that the error in the relay lens fully accounts for the error in the null lens. We proceeded to figure the mirror using the visible hologram as a reference. We are continuing to investigate the discrepancy.

7.2 Optical design and measured parameters

The optical designs of the two null lenses are given in Appendices 1 and 2. The preliminary designs and tolerance analysis are given by Burge[8] (Appendix 4). The infrared null lens consists of an aspheric diverging lens and two positive lenses in an Offner null arrangement. Its input is a collimated beam from a Twyman-Green interferometer. The larger plano-convex lens is called the relay lens and the smaller lens the field lens. The visible null lens includes the Shack-cube interferometer, a Fizeau interferometer with a point light source at the center of curvature of its spherical reference surface. A relay lens and two field lenses provide the aspheric compensation. The design is extremely well corrected, with a wavefront error (twice the corresponding mirror surface error) of 12 nm peak-to-valley.

A tolerance analysis determined the allowed error in each parameter. We separate errors into those that cause an axisymmetric wavefront error and those that cause asymmetric errors. Since the measurements of the primary mirror are insensitive to focus, axisymmetric errors are primarily spherical aberration, equivalent to an error in conic constant. In addition, departure from the nominal primary radius of curvature introduces a conic error as described in Section 6.4.

Table 9 gives the final design parameters of the visible null lens, the specified tolerances, as-built dimensions, and uncertainties or measured errors. For most parameters, the final design incorporates the measured values. In a few cases, subsequent measurements that depart from the design are listed in the table. Refractive indices are taken from the melt data supplied by the manufacturer. The glass is Ohara BSL7 (Ohara's version of Schott BK7) for the relay lens and field lens 2, and Schott BK7 for field lens 1. For both glasses the specified uncertainty in mean index is 10^{-5} and the specified homogeneity is 10^{-6} peak-to-valley. The net uncertainty of the null lens, excluding the primary radius of curvature, is 110 ppm in conic constant and 20 nm residual rms

surface error. The residual error ignores tilt and coma, which are eliminated by alignment of the interferometer relative to the primary mirror.

Table 9. Dimensions of visible null lens (mm unless listed)

parameter	design value	tolerance	measured	uncertainty
Shack cube:				
radius of curvature	29.490	0.005	29.480	0.014
airspace	784.497	0.020	784.497	0.020
relay lens:				
radius surface 1	2518.3 ccv	0.5	2518.3	0.1
thickness	55.495	0.010	55.495	0.005
radius surface 2	206.253 cvx	0.010	206.252	0.005
airspace	440.953	0.020	440.953	0.020
field lens 1:				
radius surface 1	198.118 ccv	0.005	198.118	0.002
thickness	18.110	0.005	18.114	0.006
radius surface 2	210.770 cvx	0.005	210.770	0.002
airspace	113.022	0.010	113.022	0.010
field lens 2:				
curvature surface 1	0.18×10^{-6} mm^{-1} cvx	0.13×10^{-6} mm^{-1}	0.20×10^{-6} mm^{-1}	0.03×10^{-6} mm^{-1}
thickness	14.366	0.010	14.358	0.011
radius surface 2	582.047	0.010	582.047	0.008

The corresponding predicted uncertainties for the IR null lens are 160 ppm in conic constant and 1.5 micron residual rms surface error. The predicted rms surface error is dominated by possible refractive index variations within the large germanium relay lens, and could contain an axisymmetric component that would contribute to the uncertainty in conic constant. In fact, how-

ever, the hologram measurement with the IR null lens gave only 0.2 micron rms surface error, including spherical aberration, implying that the germanium is much more uniform than we thought.

7.3 Corrections with computer-generated holograms

We calibrated each null lens with a computer-generated hologram. The design and fabrication of the hologram is independent of the design and fabrication of the null lens, except that both are derived from the prescription of the primary mirror. The hologram consists of many thin concentric circles of reflective material deposited on a thick flat glass substrate placed at the paraxial center of curvature. The radial line spacing is designed to diffract each ray back along its incident path exactly as it would be reflected by a perfect primary mirror. Both holograms were fabricated at the Institute of Automation and Electrometry (IAE) in Novosibirsk, Russia.

The wavefront diffracted by the hologram is very sensitive to laser wavelength. For the visible hologram, a change in wavelength by 0.1 nm causes 310 nm of spherical aberration, or a conic error of 560 ppm. Our frequency-doubled YAG laser's wavelength is unstable at that level, so we measure its wavelength at the same time we measure the hologram and correct the hologram measurement accordingly. Table 10 lists the effects of wavelength uncertainty and other significant terms in the visible hologram's error budget. In the table and throughout this section, we quote spherical aberration and conic errors to a precision of 5 nm in ΔR_4^0 and almost equivalently 10 ppm in Δk.

Table 10. Error budget for visible hologram

source	ΔR_4^0 (nm)	Δk (ppm)
writing error of 0.5 μm over 68 mm radius	15	30
wavelength error of 0.01 nm	30	60
noise in phase measurement	10	20
sum in quadrature	35	70

The IR hologram measurement was not intended to be a definitive measurement of conic constant, but it does provide additional information which may be useful, especially in light of the large error measured in the visible. We estimate that the IR hologram measurement has a conic uncertainty of about 200 ppm.

We measure the hologram exactly as we measure the primary mirror. All large-scale errors in the resulting map are interpreted as errors in the null lens. The map also contains some small-scale features due to the hologram or noise in the measurement. We average a number of maps with the hologram at two or more rotation angles in order to average out some of its non-axisymmetric errors. We filter out spurious small-scale structure by fitting Zernike polynomials to the map and using the polynomial representation. We fit 36 polynomials, but only retain those coeffi-

cients whose absolute values in the average map exceed their standard deviations among the individual maps.

Figure 9 and Table 11 show the result of the visible hologram measurement, along with the correction for wavelength. The hologram is designed for a wavelength of 530.662 nm, and the correction for the measured wavelength (530.778 ± 0.01 nm) reverses the sign of spherical aberration. Apart from the spherical aberration, the errors are less than those predicted by the tolerance analysis of the null lens.

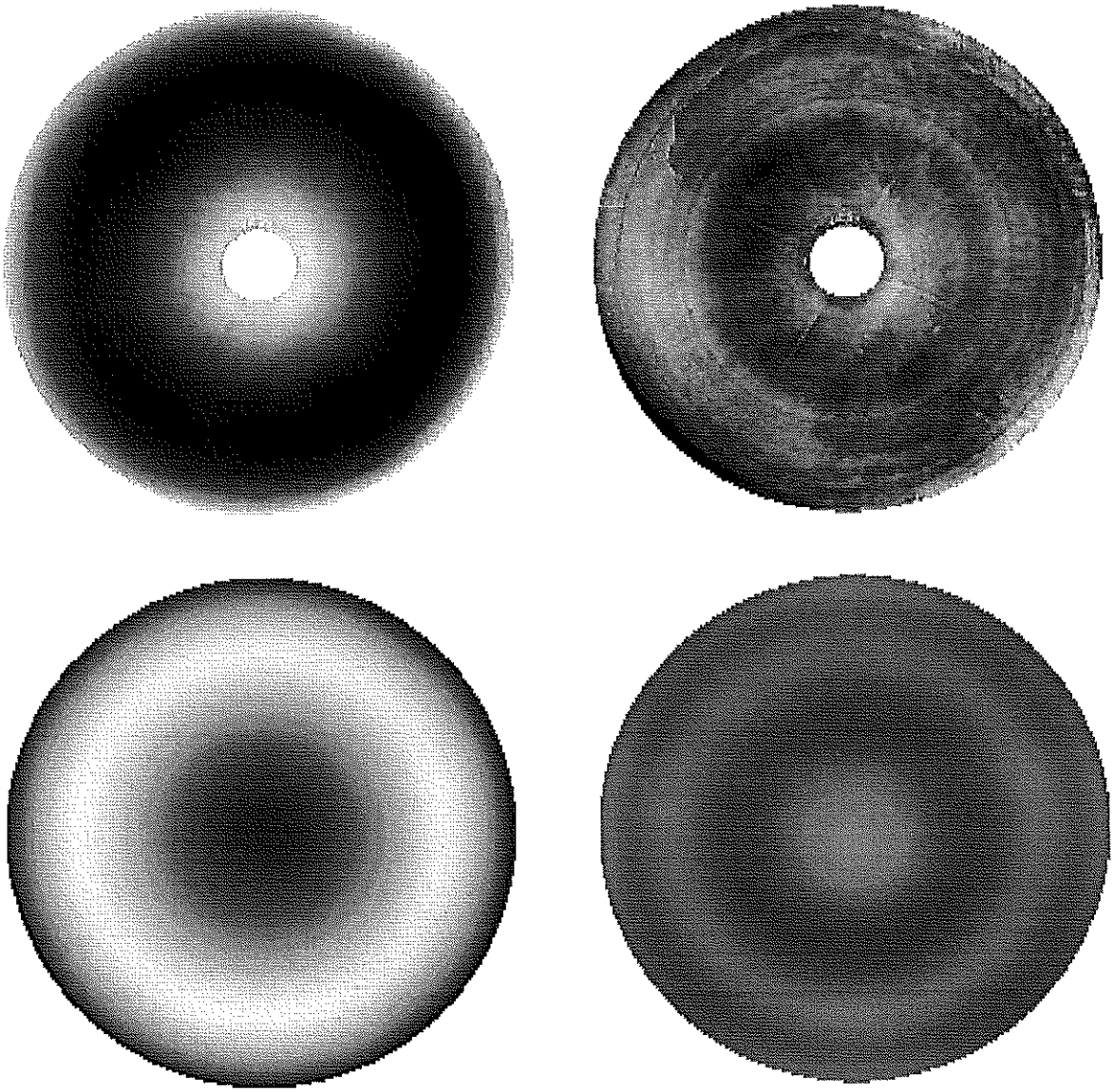

Figure 9. Surface maps representing the error in the visible null lens as determined by measurement of the hologram. Upper left: uncorrected map of hologram, with 200 nm spherical aberration; gray scale covers ±150 nm. Upper right: same map with spherical aberration removed, with an rms error of 14 nm; gray scale covers ±50 nm. Lower left: polynomial fit to map of hologram, corrected for wavelength, with –155 nm spherical aberration; gray scale covers ±150 nm. Lower right: same map with spherical aberration removed, with an rms error of 5.5 nm; gray scale covers ±50 nm.

Table 11. Spherical aberration in measurement of visible hologram

term	value (nm)
measured R_4^0	200
wavelength correction	–355
net R_4^0	–155

The disagreement between the visible null lens and hologram is disturbing. We have attempted to resolve it in several ways, including remeasurement of all mechanical dimensions of the null lens, measuring the diameter of the outer ring of the hologram, and measuring the wavefront transmitted by the large relay lens (Section 7.5). We have also made a careful comparison of the visible and IR measurements at the time of hand-off from IR to visible testing (Section 7.4).

Figure 10 shows the result of the infrared hologram measurement. No correction for wavelength was made. The map contains 70 nm of spherical aberration. The corresponding conic error of 130 ppm is within the expected uncertainty of both the IR null lens and the IR hologram.

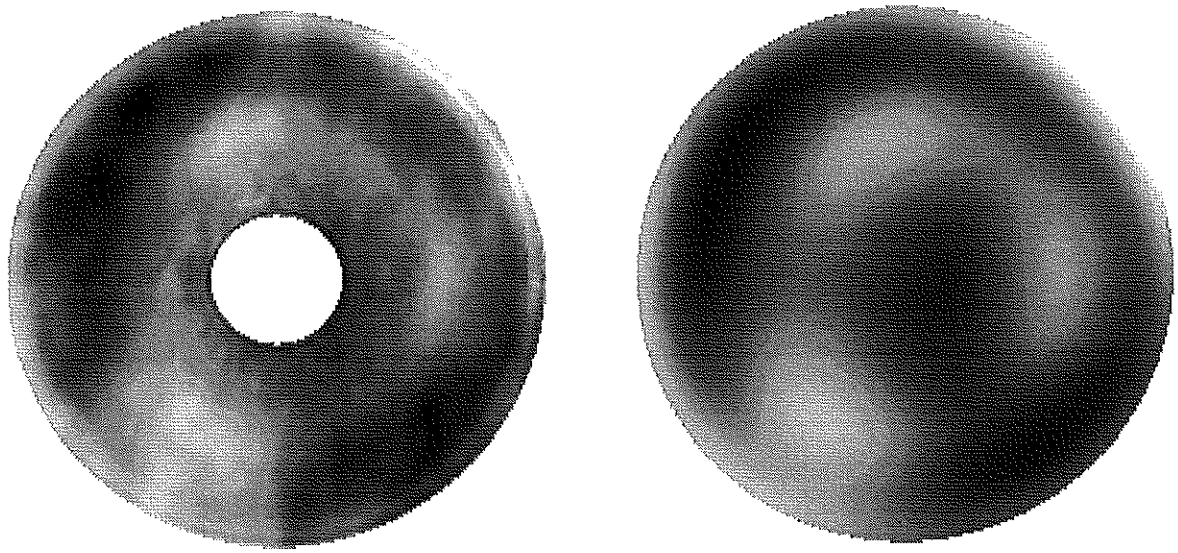

Figure 10. Surface maps representing the error in the IR null lens as determined by the hologram measurement. Left: map of hologram, with 70 nm spherical aberration; gray scale covers ±600 nm. Right: polynomial fit to map of hologram; gray scale covers ±600 nm.

7.4 Comparison of visible and IR measurements

The visible measurements are expected to be more accurate than the IR measurements in all respects. We do, however, expect the two measurements to agree within the uncertainty of the IR measurements. Given the large discrepancy between the visible null lens and visible hologram, the IR measurements can help distinguish which is correct. We measured the mirror with both in-

terferometers on June 9, 1998. (This was the first visible measurement.) Figure 11 compares the results, with and without correcting each measurement with the hologram. With the exception of the uncorrected IR map, there is good agreement in the overall figure.

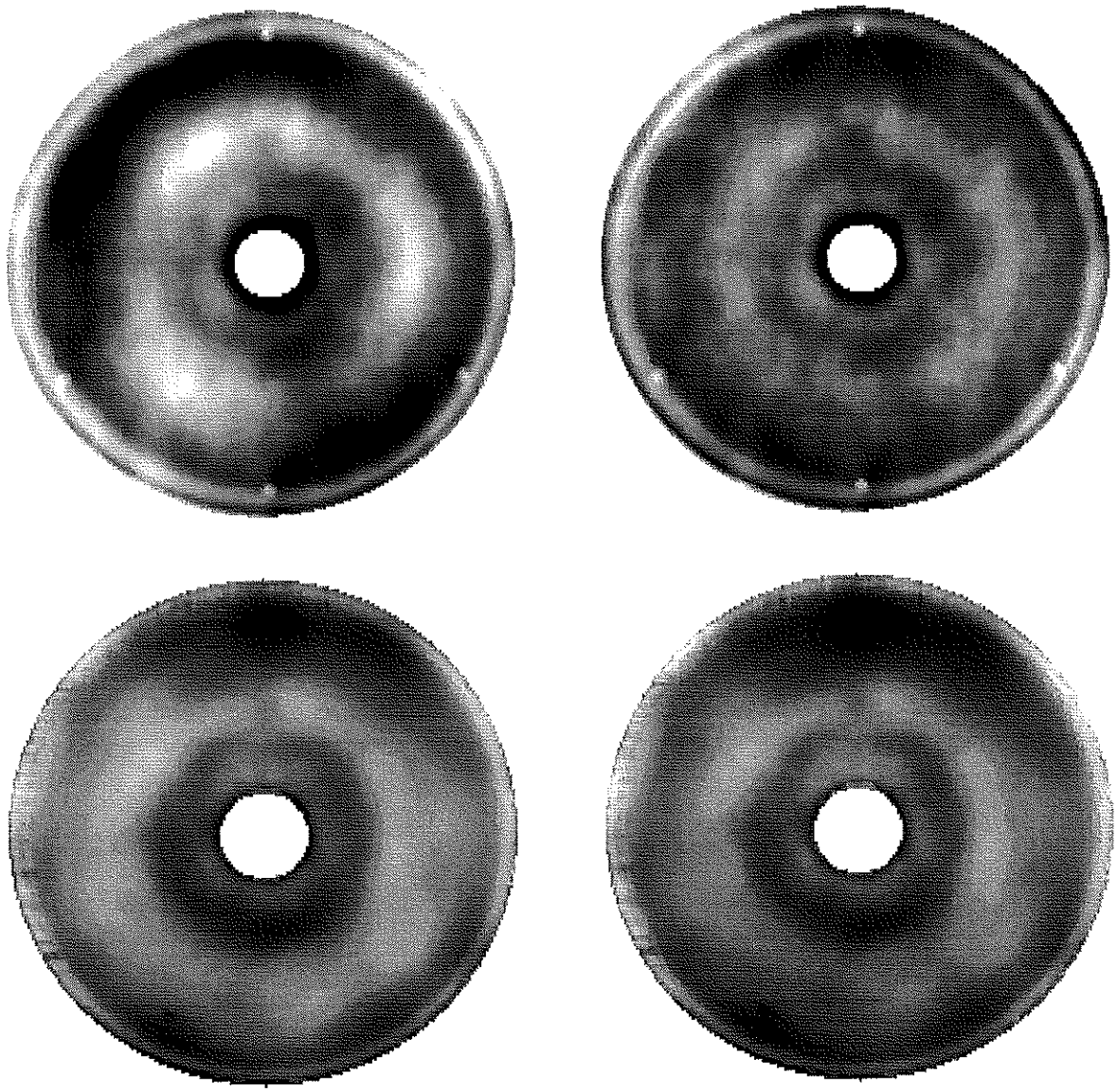

Figure 11. Visible and IR measurements of the mirror made on June 9, 1998, with and without subtraction of the corresponding hologram map. Upper left: uncorrected IR map. Upper right: corrected IR map (uncorrected map - hologram map). Lower left: uncorrected visible map. Lower right: corrected visible map. The gray scale covers ±500 nm for all maps. The visible maps cover only 6.36 m diameter because of the high slopes near the outer edge at the time of this measurement.

At each wavelength we have two measurements of spherical aberration: one determined by measuring the mirror with the null lens alone, and another by applying the hologram correction. The four measurements are plotted as a conic error in Figure 12. The error bars are dominated by the expected uncertainty in the null lens or hologram. A second, smaller term, the

uncertainty in determining spherical aberration from the surface map, is obtained by fitting different numbers of polynomials and comparing the fitted value of third-order spherical aberration, R_4^0. The values plotted in Figure 12 should be used only to compare the different measurements and not to indicate the conic constant of the finished mirror. No conic correction has been made for the mirror's radius of curvature, and the figure changed substantially after these measurements were made.

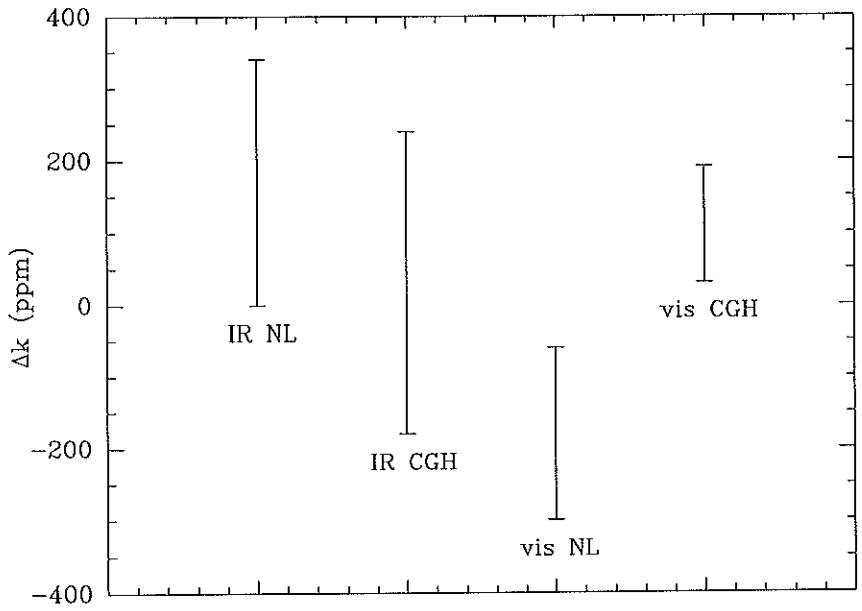

Figure 12. Conic error inferred from IR and visible measurements made on June 9, 1998. Values labelled NL are based on the null lens; those labelled CGH are based on the hologram. These values serve as a comparison only and do not reflect the actual conic constant of the finished mirror.

The comparison reveals that the visible hologram and IR null lens agree almost perfectly, the visible null lens disagrees substantially with the visible hologram, and the IR hologram is consistent with all the other measurements. Resolving the discrepancy between the visible null lens and visible hologram is a high priority. In the meantime, we have chosen to trust the visible hologram, primarily because its uncertainties are smaller and better understood than those of the null lens. The IR measurements support that choice, although not definitively.

7.5 CGH test of the relay lens

Our measurements of mechanical dimensions of the null lens did not reveal any significant source of spherical aberration in the null lens. A remaining possibility is that the glass has a refractive index that was different from the reported value or varied within a lens. The thick relay lens is the most likely candidate for index errors. We therefore measured the transmitted wavefront from this lens alone, using a hologram test similar to that for the full null lens. The hologram was again fabricated by the IAE and has a predicted accuracy of 2.7 nm surface spherical aberration. It covers only the inner 190 mm diameter of the relay lens while the measurement of the primary mirror uses 242 mm on the relay lens. The measured spherical aberration must therefore be

scaled to the full diameter for comparison with the measurement of the full null lens. A wavelength correction is applied as for the test of the full null lens. The design wavelength was 530.669 nm while the measured wavelength was 530.778 nm.

The results are summarized in Table 12. There is significant spherical aberration, indicating an error in the index of the relay lens, and the amount of spherical aberration agrees with that measured in the null lens. Whether the error in the relay lens fully explains the spherical aberration in the null lens depends on the precise form of the error. The relay measurement can be explained by a quadratic radial variation in index with an amplitude of 18 ppm, 18 times the specified variation. This error would cause spherical aberration in the full null lens with an amplitude about 80% of the measured value, consistent within the uncertainties. But the relay measurement can also be explained by an error in mean index of 27 ppm, 2.7 times the specified accuracy, with no radial variation. This error would produce only 20% of the spherical aberration seen in the test of the null lens. At the present, we cannot distinguish among these and other possibilities.

Table 12. Measurement of the relay lens hologram

	value (nm)	uncertainty (nm)
measured R_4^0	55	5
wavelength correction	–125	10
net R_4^0 over 190 mm	–70	10
R_4^0 projected to 242 mm	–176	30

All measurements are consistent with the hypothesis that the primary mirror's conic constant has the value -0.99992 ± 0.00008. We rely heavily on a single measurement, the hologram measurement of the full null lens, to establish that accuracy. We plan to make a separate measurement of the null lens after respacing the elements to work with a HeNe laser at 633 nm. This measurement will have the advantage of a much smaller uncertainty in wavelength. It may be, however, that the issue will be completely resolved only with the prime focus tests of the MMT 6.5 m mirror, which was made using the same null lens.

8. References

1. B. Olbert, J. R. P. Angel, J. M. Hill and S. F. Hinman, "Casting 6.5 meter mirrors for the MMT Conversion and Magellan", *Advanced Technology Optical Telescopes V*, ed. L. M. Stepp, Proc. SPIE 2199, p. 144 (1994).
2. H. M. Martin, J. H. Burge, D. A. Ketelsen and S. C. West, "Fabrication of the 6.5 m primary mirror for the Multiple Mirror Telescope Conversion", *Optical Telescopes of Today and Tomorrow*, ed. A. Ardeberg, Proc. SPIE 2871, p. 399 (1997).
3. Technical Specifications and Requirements for the Second Magellan 6.5 Meter Telescope Primary Mirror, November 18, 1996; revised May 21, 1997; Magellan Project Document No. 96PR0105.
4. R. E. Hufnagel, "Propagation through Atmospheric Turbulence", Ch. 6 of The Infrared Handbook, ed. W. L. Wolfe and G. J. Zissis, p. 6-32 (Washington: U. S. Govt. Printing Office, 1978).
5. BCV MMT Conversion Project: Primary Mirror, Rep. # 8 Rev. 0, "Mirror 6.5m f/1.25 axial supports influence functions".
6. H. M. Martin, S. P. Callahan, B. Cuerden, W. B. Davison, S. T. DeRigne, L. R. Dettmann, G. Parodi, T. J. Trebisky, S. C. West and J. T. Williams, "Active supports and force optimization for the MMT primary mirror", *Advanced Technology Optical/IR Telescopes VI*, ed. L. M. Stepp, Proc. SPIE 3352, p. 412.
7. J. Lubliner and J. E. Nelson, "Stressed mirror polishing. 1: A technique for producing nonaxisymmetric mirrors", Applied Optics, **19**, 2332 (1980).
8. J. H. Burge, *Advanced Techniques for Measuring Primary Mirrors for Astronomical Telescopes*, Ph. D. Dissertation, University of Arizona (1993).
9. J. H. Burge, D. S. Anderson, D. A. Ketelsen and S. C. West, "Null test optics for the MMT and Magellan 6.5-m f/1.25 primary mirrors", *Advanced Technology Optical Telescopes V*, ed. L. M. Stepp, Proc. SPIE 2199, p. 658 (1994).

9. Appendices

1. Infrared null lens design
2. Visible null lens design
3. Chapter 6 from Burge's dissertation, Reference 8
4. Appendices C and D from Burge's dissertation, Reference 8

stem/Prescription Data

le : D:\Mirror Projects\Magellan Primary\Null Lens\mmtir.zmx
Title: MMT NULL LENS
Date : MON JAN 4 1999

NERAL LENS DATA:

Surfaces	18
Stop	9
stem Aperture	Float By Stop Size = 3256
y aiming	Paraxial Reference, cache on
X Pupil shift	0
Y Pupil shift	0
Z Pupil shift	0
odization	Uniform, factor = 0.00000E+000
f. Focal Len.	100.0007 (in air)
Eff. Focal Len.	100.0007 (in image space)
Back Focal Len.	0.000671643
tal Track	17378.84
age Space F/#	2.72477
ra. Wrkng F/#	2.72477
Working F/#	2.677627
Obj. Space N.A.	1.83503e-009
op Radius	3256
rax. Ima. Hgt.	0
Parax. Mag.	0
Entr. Pup. Dia.	36.70059
Entr. Pup. Pos.	-0.001095654
it Pupil Dia.	36.70019
it Pupil Pos.	99.9989
Field Type	Angle in degrees
Maximum Field	0
imary Wave	10.553
ns Units	Millimeters
gular Mag.	0

Fields : 1
eld Type: Angle in degrees

	X-Value	Y-Value	Weight
1	0.000000	0.000000	1.000000

ignetting Factors

VDX	VDY	VCX	VCY
0.000000	0.000000	0.000000	0.000000

Wavelengths : 1
its: Microns

	Value	Weight
1	10.553000	1.000000

SURFACE DATA SUMMARY:

rf	Type	Comment	Radius	Thickness	Glass	Diameter	Conic
OBJ	STANDARD		Infinity	Infinity		0	0
1	STANDARD		Infinity	28.88		38.02686	0
2	STANDARD		77.964	12.007	2.402200, 0.000	50	0
3	EVENASPH		-60.56	140.513		44	0
4	STANDARD		Infinity	28.069	4.002800, 0.000	200	0
5	STANDARD		-355.906	429.983		200	0
6	STANDARD		-8027000	13.852	2.402200, 0.000	80	0
7	STANDARD		-625.8	369.5379		80	0
8	STANDARD		Infinity	16256		130.6196	0
STO	STANDARD		-16256	-16256	MIRROR	6512	-1
10	STANDARD		Infinity	-369.5379		130.6302	0
11	STANDARD		-625.8	-13.852	2.402200, 0.000	80	0
12	STANDARD		-8027000	-429.983		80	0
13	STANDARD		-355.906	-28.069	4.002800, 0.000	200	0
14	STANDARD		Infinity	-140.513		200	0
15	EVENASPH		-60.56	-12.007	2.402200, 0.000	44	0
16	STANDARD		77.964	-28.88		50	0
17	PARAXIAL		-	-100		38.02349	-
IMA	STANDARD		Infinity			0.0083269	0

INDEX OF REFRACTION DATA:

urf	Glass	10.553000
0		1.00000000
1		1.00000000
2	<MODEL>	2.40220000
3		1.00000000
4	<MODEL>	4.00280000
5		1.00000000
6	<MODEL>	2.40220000
7		1.00000000
8		1.00000000
9	MIRROR	1.00000000

10		1.00000000
11	<MODEL>	2.40220000
12		1.00000000
13	<MODEL>	4.00280000
14		1.00000000
15	<MODEL>	2.40220000
16		1.00000000
17		1.00000000
18		1.00000000

THERMAL COEFFICIENT OF EXPANSION DATA:

Surf	Glass	TCE
0		0.00000000
1		0.00000000
2	<MODEL>	7.10000000
3		0.00000000
4	<MODEL>	5.70000000
5		0.00000000
6	<MODEL>	7.10000000
7		0.00000000
8		0.00000000
9	MIRROR	0.00000000
10		0.00000000
11	<MODEL>	7.10000000
12		0.00000000
13	<MODEL>	5.70000000
14		0.00000000
15	<MODEL>	7.10000000
16		0.00000000
17		0.00000000
18		0.00000000

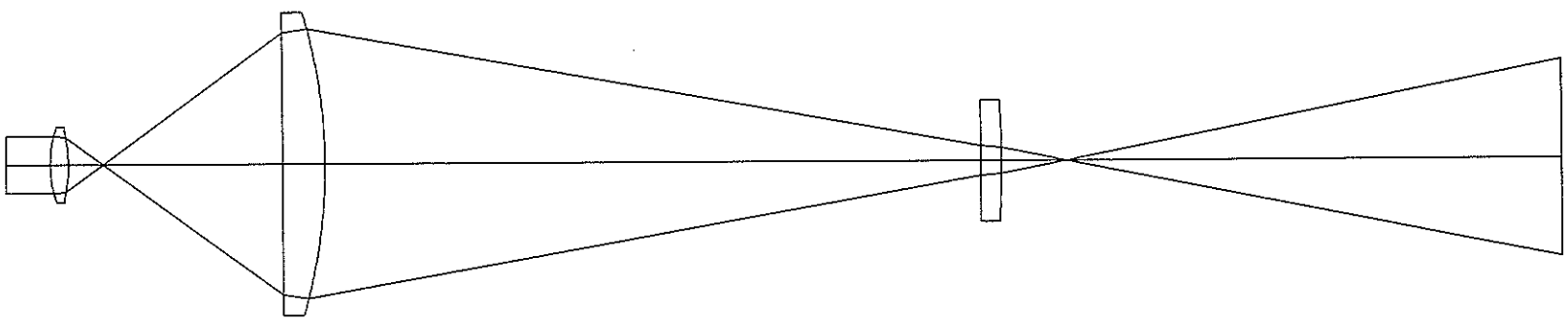

LAYOUT

MMT NULL LENS
MON JAN 4 1999
TOTAL LENGTH: 1022.84186 MM

LEE DETTMANN
SOML

D:\MIRROR PROJECTS\MAGELLAN PRIMARY\NULL LENS\MMTIR.ZMX

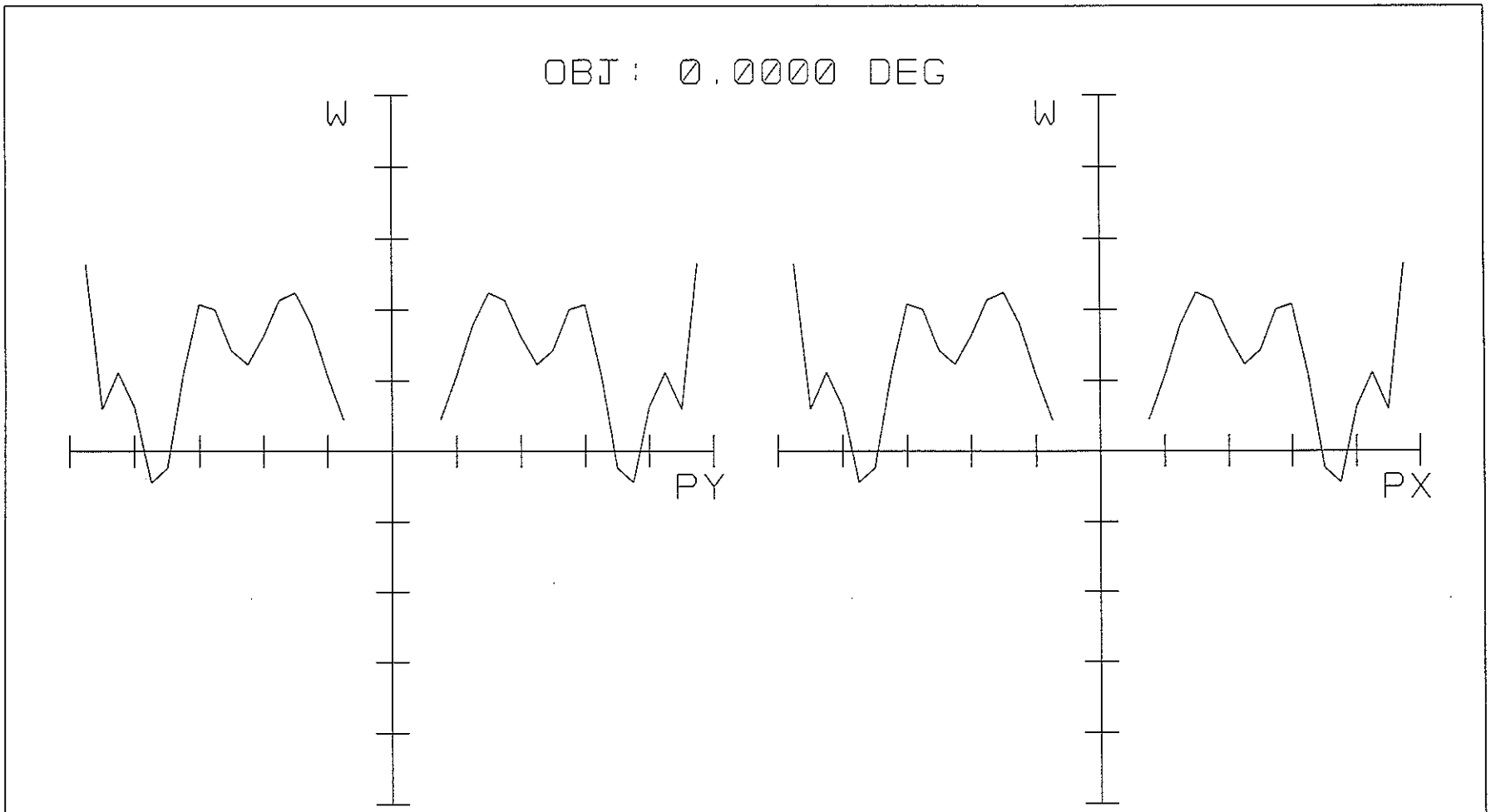

OPTICAL PATH DIFFERENCE

MMT NULL LENS
MON JAN 4 1999
MAXIMUM SCALE: +/- 0.010 WAVES.
10.553

LEE DETTMANN
SOML

D:\MIRROR PROJECTS\MAGELLAN PRIMARY\NULL LENS\MMTIR.ZMX

/stem/Prescription Data

.le : D:\Mirror Projects\Magellan Primary\Null Lens\mmtvis 12-9-98 Jim meas melt data.zmx
Title: MMT NULL LENS 12/9/98
Date : MON JAN 4 1999

ENERAL LENS DATA:

Surfaces	:	18
Stop	:	9
/stem Aperture	:	Float By Stop Size = 3250
ıy aiming	:	Paraxial Reference, cache on
X Pupil shift	:	0
Y Pupil shift	:	0
Z Pupil shift	:	0.5
›odization	:	Uniform, factor = 0.00000E+000
ff. Focal Len.	:	-25.99613 (in air)
Eff. Focal Len.	:	-25.99613 (in image space)
Back Focal Len.	:	26.00775
›tal Track	:	17967.27
ıage Space F/#	:	1.029107
ıara. Wrkng F/#	:	2.057753
Working F/#	:	2.36715
Obj. Space N.A.	:	0.2395859
Stop Radius	:	3250
ıarax. Ima. Hgt.	:	0
Parax. Mag.	:	0
Entr. Pup. Dia.	:	25.26088
ıtr. Pup. Pos.	:	-105.4556
Exit Pupil Dia.	:	17.29287
Exit Pupil Pos.	:	-52.00388
Field Type	:	Angle in degrees
Maximum Field	:	0
Primary Wave	:	0.53066
ens Units	:	Millimeters
ngular Mag.	:	0

Fields : 1
ield Type: Angle in degrees

	X-Value	Y-Value	Weight
1	0.000000	0.000000	1.000000

ignetting Factors

VDX	VDY	VCX	VCY
0.000000	0.000000	0.000000	0.000000

Wavelengths : 1
nits: Microns

	Value	Weight
1	0.530660	1.000000

URFACE DATA SUMMARY:

urf	Type	Comment	Radius	Thickness	Glass	Diameter	Conic
OBJ	STANDARD		Infinity	29.49	SILICA	0	0
1	STANDARD		-29.49	784.497		8.530215	0
2	STANDARD		-2518.3	55.495	1.519930, 0.000	270	0
3	STANDARD		-206.253	440.953		270	0
4	STANDARD		-198.118	18.11	1.519618, 0.000	90	0
5	STANDARD		-210.77	113.022		90	0
6	STANDARD		5555555	14.366	1.519185, 0.000	64	0
7	STANDARD		-582.047	255.3391		64	0
8	STANDARD		Infinity	16256		129.9059	0
STO	STANDARD		-16256	-16256	MIRROR	6500	-1
10	STANDARD		Infinity	-255.3391		129.9023	0
11	STANDARD		-582.047	-14.366	1.519185, 0.000	27.73821	0
12	STANDARD		5555555	-113.022		23.80224	0
13	STANDARD		-210.77	-18.11	1.519618, 0.000	24.54979	0
14	STANDARD		-198.118	-440.953		28.85051	0
15	STANDARD		-206.253	-55.495	1.519930, 0.000	241.4549	0
16	STANDARD		-2518.3	-784.497		237.1396	0
17	STANDARD		-29.49	-29.49	SILICA	8.523776	0
IMA	STANDARD		Infinity			0.004720699	0

INDEX OF REFRACTION DATA:

urf	Glass	0.530660
0	SILICA	1.46076862
1		1.00000000
2	<MODEL>	1.51993000
3		1.00000000
4	<MODEL>	1.51961800
5		1.00000000
6	<MODEL>	1.51918500
7		1.00000000
8		1.00000000
9	MIRROR	1.00000000

10		1.00000000
11	<MODEL>	1.51918500
12		1.00000000
13	<MODEL>	1.51961800
14		1.00000000
15	<MODEL>	1.51993000
16		1.00000000
17	SILICA	1.46076862
18		1.00000000

THERMAL COEFFICIENT OF EXPANSION DATA:

Surf	Glass	TCE
0	SILICA	0.00000000
1		0.00000000
2	<MODEL>	0.00000000
3		0.00000000
4	<MODEL>	0.00000000
5		0.00000000
6	<MODEL>	6.20000000
7		0.00000000
8		0.00000000
9	MIRROR	0.00000000
10		0.00000000
11	<MODEL>	6.20000000
12		0.00000000
13	<MODEL>	0.00000000
14		0.00000000
15	<MODEL>	0.00000000
16		0.00000000
17	SILICA	0.00000000
18		0.00000000

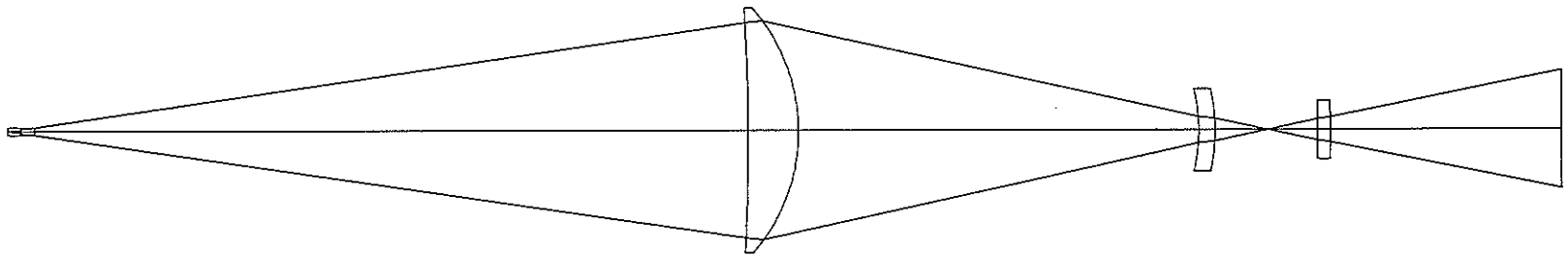

LAYOUT

MMT NULL LENS 12/9/98
MON JAN 4 1999
TOTAL LENGTH: 1711.27197 MM

LEE DETTMANN
SOML

D:\MIRROR PROJECTS\MAGELLAN PRIMARY\NULL LENS\MMTVIS 12-9-98 JIM MERS MELT DATA.ZMX

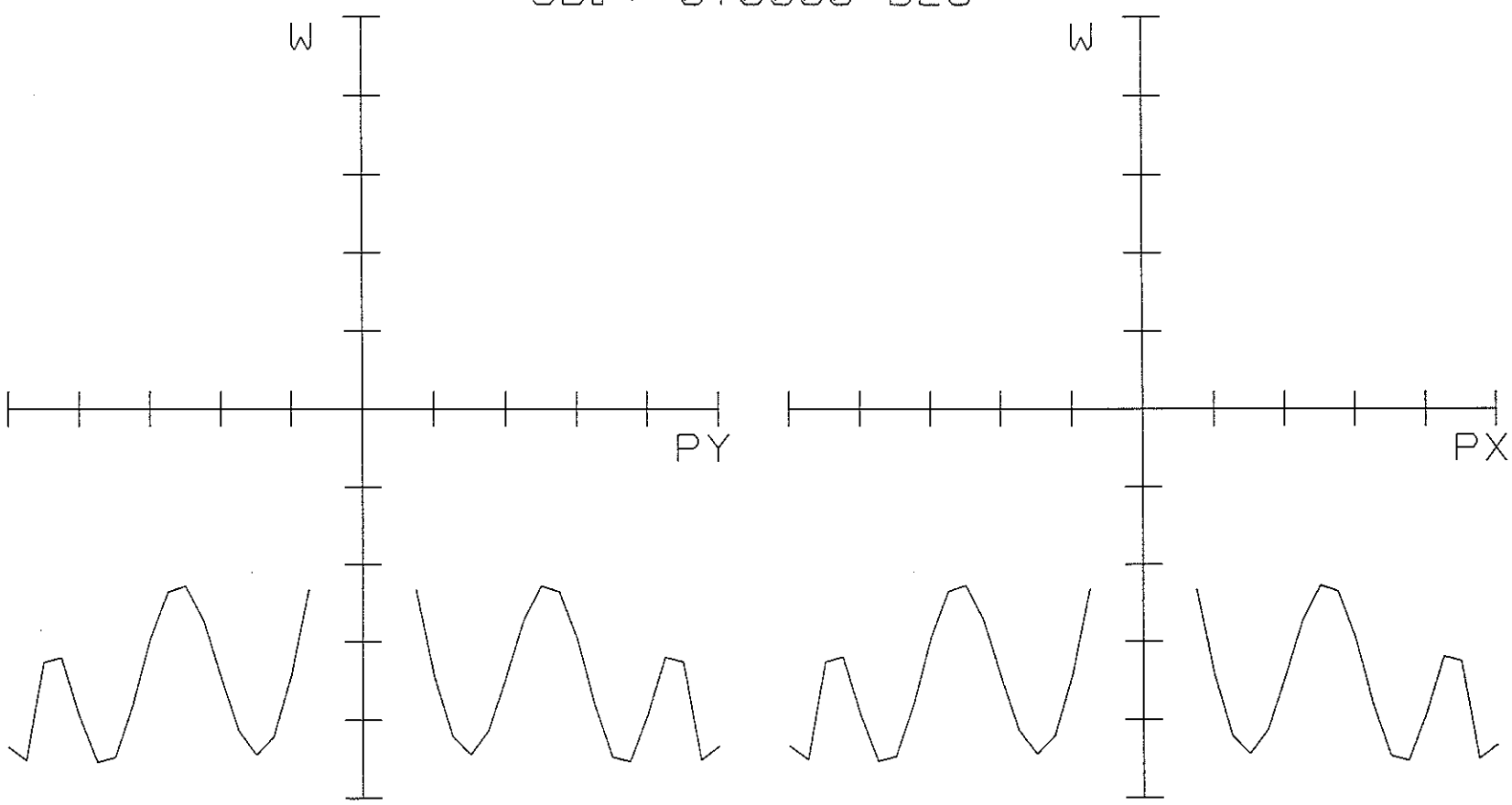

OPTICAL PATH DIFFERENCE

MMT NULL LENS 12/9/98
MON JAN 4 1999
MAXIMUM SCALE: +/- 0.050 WAVES.
0.531

LEE DETTMANN
SOML

D:\MIRROR PROJECTS\MAGELLAN PRIMARY\NULL LENS\MMTVIS 12-9-98 JIM MEAS MELT DATA.ZMX

CHAPTER 6

HOLOGRAPHIC MEASUREMENT OF NULL CORRECTORS: THEORY AND DESIGN

6.1. INTRODUCTION

An optical test has been devised to test and qualify null correctors that are used for measuring highly aspheric primary mirrors. The technique employs a rotationally symmetric computer-generated hologram (CGH) that tests the null corrector directly by synthesizing a wavefront that would be returned by a perfect primary mirror. The test, which is quick and highly accurate, has been demonstrated on null correctors for two 3.5-m primary mirrors.

Large primary mirrors for optical telescopes are interferometrically tested from center of curvature using null correctors. In fabricating a primary mirror, the optical surface is polished to precisely match the wavefront generated by the null corrector. There is always a possibility that the null corrector could be flawed, resulting in the final shape of the mirror being incorrect. Two recent telescopes had their primary mirrors made to the wrong shape because of errors in the null correctors -- the Hubble Space Telescope or HST (Allen *et al.* 1990) and the New Technology Telescope or NTT (Wilson *et al.* 1991). If accurate testing of the null correctors had been performed, the errors would have been discovered and corrected in the shop. Instead, the errors were not discovered until the finished mirrors were in their telescopes on a mountain top or in orbit.

The holographic test of null correctors fills an important gap in the fabrication of highly aspheric optics. Because the null correctors introduce hundreds of waves of asphericity, they are complex and sensitive to manufacturing errors. A small manufacturing flaw or oversight may cause significant aberration in the null lens resulting in a mirror finished to the wrong shape. For this reason the verification of the test optics is viewed as a critical step in the fabrication of highly aspheric optics. One method of verifying the optical test is to compare results from two independent null lenses. This is expensive and can be inconclusive. (What if the two null lenses do *not* agree?) Another technique is to perform an independent test on the completed mirror such as a scanning pentaprism test. Accurate tests of this type are difficult and expensive. These tests must be performed on a completed mirror, which involves some risk to the surface. Also, if an error is detected in the finished mirror, either the mirror or the telescope must be corrected.

This chapter gives a general description and analysis of this new method of testing null correctors. The following chapter gives results and analysis from actual measurements. Readers interested only in the results of this test should read the description in Sec. 6.2 and skip to Ch. 7.

This chapter gives a complete description of the principles, design, and analysis of the CGH test for null correctors. The test geometry and principles used for the null lens test are described in Sec. 6.2. Section 6.3 gives a brief background and history of optical testing with CGH. The emphasis is placed on techniques similar to those used in the null lens test. The design and fabrication techniques used for making the CGH are described in Sec. 6.4. The CGH phase function is explicitly derived and analyzed in this section. Approximations that are used in the error analysis are also given. The complete process of specifying and fabricating the CGH

is summarized. Design considerations for optimizing the test to give maximum contrast and complete rejection of stray orders are described in Sec. 6.5. A thorough error analysis is presented in Secs. 6.5 - 6.7 that includes errors in the fabrication of the CGH, errors in performing the test, and errors in the data analysis. These sections show the derivation of the error terms and include little discussion of specific applications. The following chapter uses the equations for error analyses of specific tests with little discussion of the derivation.

6.2. DESCRIPTION OF HOLOGRAPHIC NULL LENS TEST

In the CGH null lens test, a computer-generated hologram of the mirror is tested by the null lens. The hologram is made so it will appear to the test lenses as if it were a perfect primary mirror. The test is insensitive to alignment errors and uses no optics other than the hologram. Since the null corrector and CGH are fabricated independently, agreement between the two indicates a high probability that both are correct.

The hologram is simply a circular grating or zone plate. It is made of a circular ring pattern fabricated onto a flat glass substrate. The CGH is fabricated using electron beam lithography that has been developed for the production of integrated circuits. The spacing of the grooves is determined by the mirror surface that the hologram replaces. The groove depth and width are optimized to minimize fabrication costs, while giving the correct intensity of the diffracted light.

A layout of the CGH null test, shown in Fig. 6.1, depicts the null lens and CGH. No modifications are made to the null lens to perform this test. The null corrector tests the hologram exactly as if a real mirror was being measured.

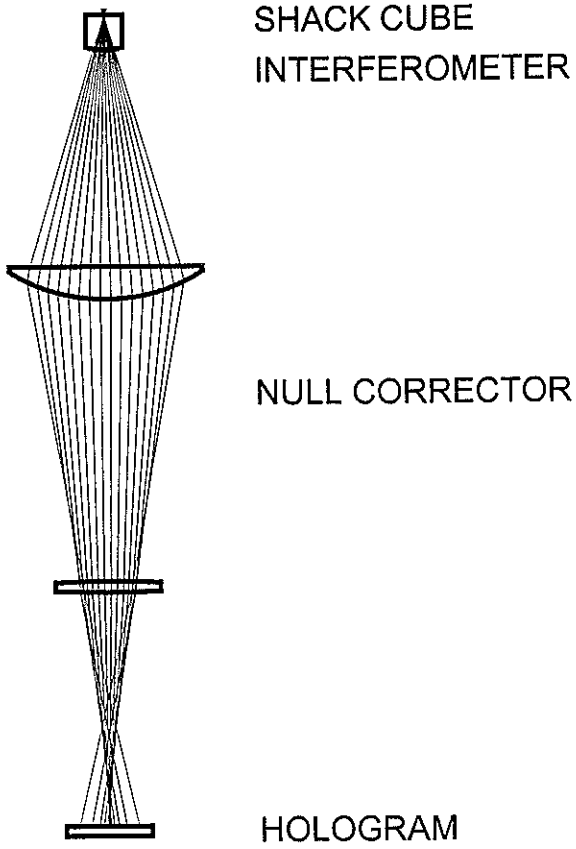

Figure 6.1. Layout of CGH test of null lens. The use of the CGH involves simply positioning the hologram at the correct location and making the measurement as if the mirror itself was being tested.

The use of the hologram to test the null corrector is surprisingly simple. The CGH is positioned in the light beam coming from the null corrector. Once the CGH is near the correct position, the fringe patterns in the interferometer are used to align the hologram. Since the CGH appears to the null corrector to be a complete primary mirror with the correct shape, the alignment of the hologram is exactly like that of the actual primary. When testing the primary mirror, the optician positions the null corrector in lateral translation, tip/tilt, and vertical translation to eliminate tilt, coma,

and focus from the interferogram (See 5.4). The alignment for the hologram follows the same procedure.

The holograms are designed to give about 4% diffraction efficiency into the desired order. This gives a high contrast interference pattern that maximizes the signal-to-noise ratio of the measurement. A pinhole positioned near the Shack cube rejects the stray orders of diffraction and lets only the desired order through. The size of the pinhole is optimized so that the area corresponding to the entire tested region of the mirror is free from spurious orders.

6.3. OPTICAL TESTING WITH COMPUTER-GENERATED HOLOGRAMS

BACKGROUND ON CGH AND OPTICAL TESTING

Optical testing of aspheric surfaces using computer-generated holograms has been used for over twenty years. An excellent overview of CGH optical testing is given by Loomis (1980a). Some more recent work in the field is given in a thorough review by Creath and Wyant (1992).

A hologram is generally used to modulate the phase or amplitude of a wavefront, causing it to propagate such that it forms a desired phase front or intensity distribution. A photographically produced hologram may be used to store and play back an existing wavefront (Leith and Upatnieks 1962). Synthetic holograms may also be specified by a computer and written with an electronic plotter (Brown and Lohmann 1966).

Computer-generated holograms fall into three classes -- Fourier, Fresnel, and image holograms, depending on the propagation from the CGH (Bryngdahl and Wyrowski 1990). The far-field or Fourier hologram, widely used in signal processing, uses a modulating screen to create a desired pattern at the Fourier plane.

The computation of the CGH pattern requires a Fourier transform of the desired field distribution. There are numerous applications and methods for making this type of CGH (Brown and Lowmann 1966, 1969; Lowmann and Paris 1967; Lee 1970; Lesem, Hirsch, and Jordan 1969; Chu, Feinup, and Goodman 1973). The second type of CGH, the Fresnel hologram, is seldom used because it is computationally intensive to create and difficult to implement (Bryngdahl and Wyrowski 1990). The computation of the Fresnel CGH pattern requires a Fresnel transform of the desired light distribution.

The third type of CGH, the image hologram, is created by plotting a ruling similar to an interferogram (Wyant and Bennett 1972; Lee 1974). Because this CGH only creates a phase distribution, the computation is direct. The ruling pattern corresponds to the interferogram that would be created at the CGH plane if the incident beam were interfered with the desired beam. Diffraction from the CGH also creates several undesired wavefronts that must be filtered out. These multiple diffracted orders can be separated at the Fourier transform plane, where a correctly positioned aperture will pass only the desired wavefront. It is this type of CGH that is commonly used in optical testing, so the following discussion will be limited to this "interferogram-type" of CGH.

Pastor (1969) first suggested the testing of aspheres using a computer-generated hologram. He described testing with a binary CGH as a moiré effect. The first CGH testing was performed by MacGovern and Wyant (1971) using a Lohmann-type CGH (Lohmann and Paris 1967) to test an F/5 paraboloid. They pointed out that this type of hologram has apertures that lie along the fringe maxima of a conventional film hologram. Wyant and Bennett (1972) abandoned the established Lee (1970) and Lohmann encoding methods and used a vector plotter to trace the fringe positions.

They give a detailed error analysis and results from testing wavefronts with aspheric departures of up to 65 waves. Wyant and O'Neill (1974) demonstrated the value of a CGH in combination with a null corrector for measuring more highly aspheric optics. CGH optical testing is now used routinely for measuring aspheric surfaces (Larionov *et al.* 1979; Smith 1981; Arnold 1989). Commercial interferometers specifically designed to utilize CGH testing have been built (Emmel and Leung 1979; Arnold 1992).

The computer-generated hologram of the image- or interferogram-type may be thought of as locally acting like a simple diffraction grating. The light diffracted from this ruling splits into distinct orders given by the grating equation

$$\begin{gathered} OPD = d_o + d_m = m\lambda \\ \text{or} \\ s(\sin\theta_0 + \sin\theta_m) = m\lambda \end{gathered} \tag{6.1}$$

where the geometry is shown in Fig. 6.2 and the terms are defined as

OPD = optical path difference for light through adjacent slits

d_0, d_m = incident and diffracted path length

θ_0, θ_m = incident and diffracted angle

m = order of diffraction

s = local ruling spacing.

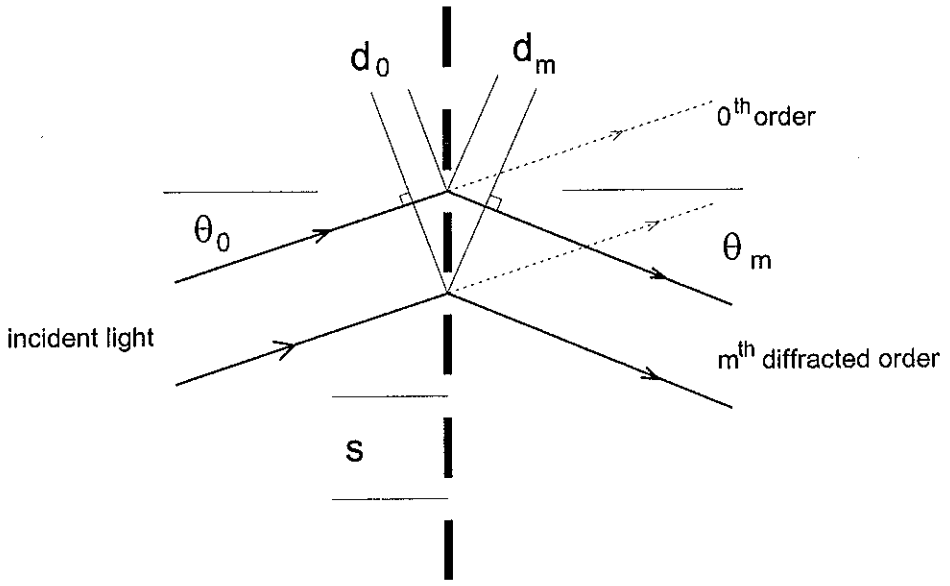

Figure 6.2. Cross-section of a transmissive diffraction ruling.

The CGH is a diffraction grating that uses a spatial variation in ruling frequency to create a desired change in wavefront. The CGH may be interpreted as causing a change in ray directions according to the grating equation (6.1), or equivalently as directly changing the wavefront phase. When used in m^{th} order, the CGH adds m waves of optical path to the wavefront for each ruling cycle.

Optical testing with a CGH is commonly performed using a configuration similar to that shown in Fig. 6.3 (Wyant and Bennett 1972; Arnold 1989). The spatial filter is required to block the unwanted orders of diffraction. The diverger lens need not be perfect, but only well known because the CGH can be designed to correct for the mirror-lens combination (Wyant and Bennett 1972).

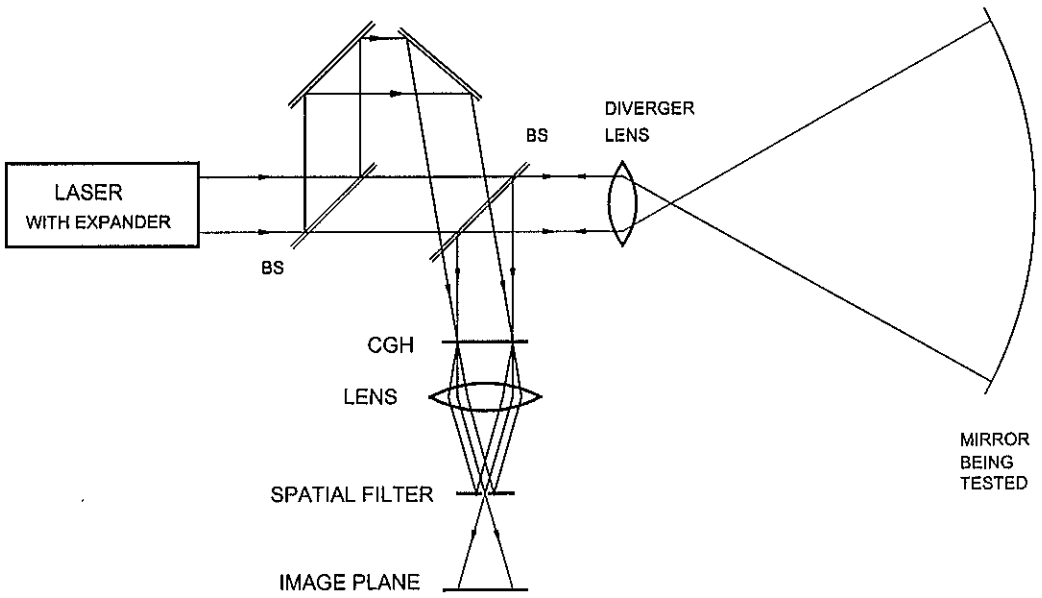

Figure 6.3. Modified Twyman-Green interferometer for testing an aspheric mirror with a CGH.

A large amount of tilt must be created by the CGH to cause the orders to fan out, enabling the isolation of a pure reference and pure test beam (Loomis 1980b). This wavefront tilt, which causes a carrier frequency in the ruling, must be three times larger than the maximum slope of the aspheric wavefront to insure complete separation of orders (Yatagai and Saito 1978).

Since the CGH is nothing more than a pattern drawn on film, its errors take the form of spatial distortion in that pattern. The magnitude of the wavefront error due to the distortion is given by Fercher (1976) as the scalar product of the wavefront gradient and the vector distortion $\varepsilon(x,y)$. This leads to

$$\Delta W(x,y) = -\nabla W_\lambda(x,y) \cdot E(x,y), \tag{6.2}$$

where ΔW = wavefront phase error due to distortion

W_λ = wavefront CGH is generating (in waves)

$\varepsilon(x,y)$ = vector CGH position error (actual position - desired position)

(x,y) = position at CGH.

One fringe represents m waves OPD, so Eq. (6.2) may also be written

$$\Delta W(x,y) = -m\lambda \frac{\varepsilon_s(x,y)}{s(x,y)}, \tag{6.3}$$

where $\varepsilon_S(x,y)$ = CGH position error in direction perpendicular to fringes

$s(x,y)$ = local center-to-center fringe spacing.

Testing with a CGH may be thought of in terms of a moiré effect. The CGH is a binary representation of the expected fringe pattern formed by an aspheric test beam and a reference beam. When the live interference pattern is superimposed on the CGH, a moiré, or spatial frequency "beating" effect is observed. When properly filtered in the frequency domain, these moiré fringes directly give the shape difference between the two wavefronts, thus the shape error in the asphere.

CGH FABRICATION

To make a CGH for optical testing, the desired wavefront $W_C(x,y)$ must be calculated. This may be done using ray-trace software (Sweatt 1977; Chen 1980), or in the case of the null lens test, it is analytically derived. Methods for encoding this into an interferogram-type CGH are described by Leung *et al.* (1980), Arnold (1988),

and Logue (1988). To encode the CGH to be used at the m^{th} order, the n^{th} fringe is drawn as a half-fringe wide contour with its edges specified by the locus of points meeting the relation

$$W_C(x,y) = n \times m \times \lambda \pm \frac{\lambda}{4}. \tag{6.4}$$

This fringe contour must be approximated and digitized for the computer-controlled writer. The resolution element used for digitizing the pattern must be chosen small enough that it creates an acceptably small error in the wavefront (Chen and Osborne 1987).

The CGH may be fabricated using technology developed for making integrated circuit masks. A large-scale master may be plotted and photographically reduced (Lohmann and Paris 1967b; Lee and Casasent 1987). The accuracy of this method is limited by the distortion in photo reduction and errors in the plotter (Wyant and O'Neill 1974; Fercher 1976; Ono and Wyant 1984). The CGH may be optically written full-scale using specialized equipment (Biedermann and Holmgren 1977; Caulfield *et al.* 1981; Kajanto *et al.* 1989; Baber 1989). Currently, the most accurate method for writing IC masks and CGH's is electron beam lithography (Leung, Lindquist, and Shepherd 1980; Leung, Arnold and Lindquist 1981; Arnold 1985; 1989).

Electron beam lithography uses a collimated electron beam to write the pattern onto a resist coated glass plate. The electron resist changes chemical properties when exposed to the electron beam enabling the resist to be dissolved in a developing chemical. The electron beam is raster scanned over small cells (~1 mm) that are stitched together by translating the workpiece using a computer-controlled stage. This method can write patterns with features as small as 0.5 μm to an accuracy of

$\pm 0.15\ \mu$m over areas as large as 150 mm square (Logue 1988). Since they are written full-scale, these masters may be used directly or they may be replicated using contact printing. The final holograms may use amplitude modulation, created by opaque fringes drawn on clear glass. Alternatively, they may use phase modulation, created by etched grooves in the glass.

CIRCULAR HOLOGRAMS

Circular holograms have been used in optical testing and are used for the CGH null lens test. Rather than using a tilt carrier to fan out the orders laterally, the rotational CGH disperses the orders axially. The use of circular holograms for optical testing was first demonstrated by Buynov *et al.* (1971). Ichioka and Lohmann (1972) discuss the use of a quadratic (focus) carrier to shift the longitudinal focus position of the unwanted orders. They used a small aperture at the focus of the desired order to restrict the interference of spurious orders to a small central area of the optic. They also show that the actual number of fringes plotted may be less for a circular hologram than for a linear hologram. Circular holograms with cone shaped carrier wavefronts were discussed by Bryngdahl and Lee (1974). In this case, the desired diffraction order was separated with an annular mask. Further comparisons between circular and tilt carrier holograms are given by Mercier (1977), and Mercier and Lowenthal (1980).

There are several advantages of using rotational holograms for testing axisymmetric optics. By preserving the axial symmetry, the hologram design and analysis are reduced from two dimensions to one. The alignment of the centered system is straightforward using conventional techniques (Mercier and Lowenthal 1980). The symmetry also allows direct certification of the hologram by measuring

ring diameters (Lukin and Mustafin 1979). For testing optics with annular apertures, the inability to test the central region is inconsequential (Aver'yanova *et al.* 1975). For testing a mirror with no central obscuration, the central region generally has very little asphericity and can be tested conventionally (Larionov *et al.* 1980).

The use of circular holograms is ideal for conditions when the desired order comes to a sharp, unaberrated focus. At this point, a small pinhole will allow the desired light cone through while blocking all other orders. Background light and spurious fringes may be further reduced by physically masking off the inner region of the light cone, corresponding to the center hole in the primary.

6.4. DESIGN AND FABRICATION OF CGH FOR NULL LENS TEST

The CGH ring pattern is computed assuming only on the shape of the primary mirror and not any specific null lens. The radial ring positions are chosen based on an exact analytical model of the rays normal to the primary mirror. Since the wavefront created by the CGH has a cusp at the center, the common method of designing the CGH by optimizing aspheric coefficients does not work well. For this design, a model is constructed using basic algebra and trigonometry that has been verified numerically. Fig. 6.4 below shows the geometry and the important dimensions. The derivation of the CGH profile is given below for the general case, but the CGH for null lens testing is optimized for use at paraxial focus ($h = 0$).

DERIVATION OF CGH PHASE FUNCTION

The phase function of the CGH is derived and specified using an exact geometrical model. The parameters for this derivation are shown below in Fig. 6.4. This model is constructed by computing the absolute path length, along the direction

of propagation, between the mirror and the hologram plane. The variation in path length across the mirror defines the wavefront that the hologram must create to appear as a perfect primary mirror.

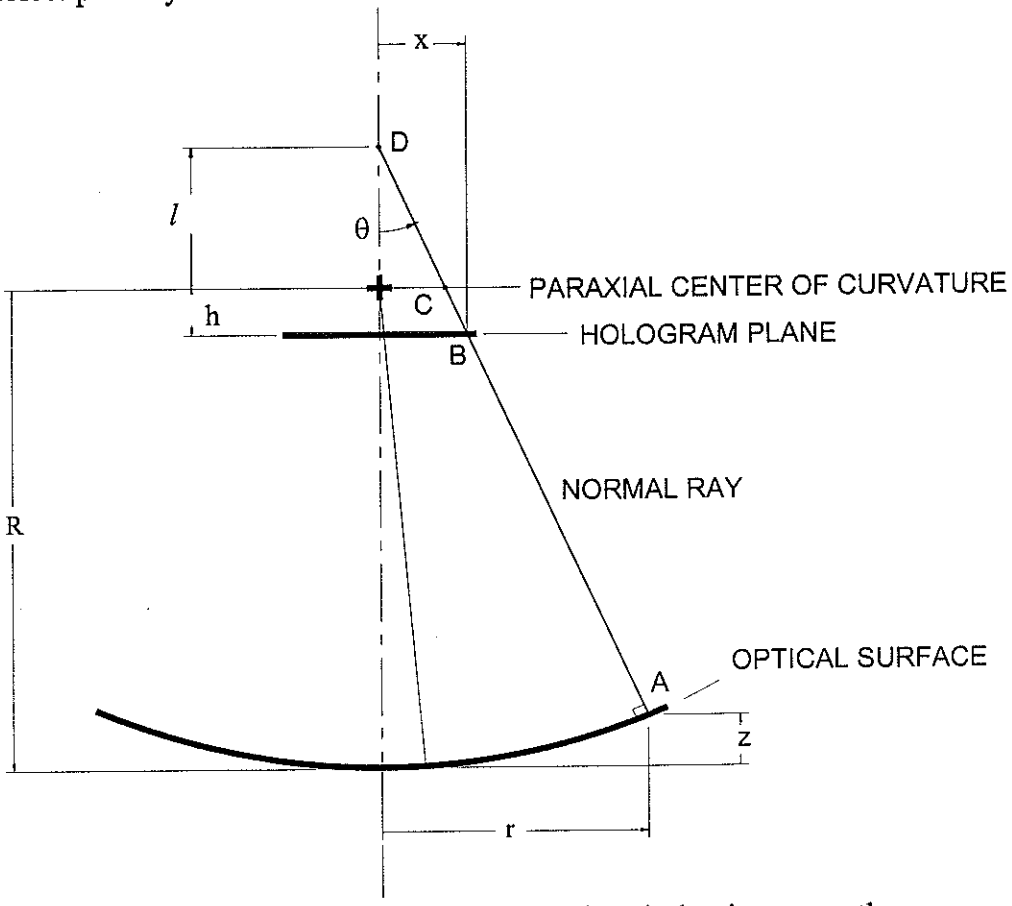

Figure 6.4. Geometry for defining a CGH such that it returns the same wavefront as a perfect primary mirror.

The variables shown in Fig. 6.4 are defined as

r = radial mirror position

R = vertex (paraxial) radius of curvature of mirror

K = conic constant of mirror

$z(r)$ = mirror surface profile

h = hologram distance from paraxial center of curvature

$x(r)$ = ray intercept position on hologram

$l(r)$ = distance from paraxial center of curvature to zonal center of curvature (longitudinal spherical aberration)

$\theta(r)$ = slope of normal ray

AD, BD = distance between points.

The shape of the optical surface is given by

$$z(r) = \frac{r^2}{R + \sqrt{R^2 - (K+1)r^2}}. \tag{6.5}$$

It is easily shown (Buchroeder *et al.* 1972) for a conic of revolution,

$$l = -Kz. \tag{6.6}$$

Trigonometry and algebra provide the following useful relations:

$$\tan\theta = \frac{r}{R - (K+1)z} \tag{6.7}$$

$$x = (h - Kz)\tan\theta \tag{6.8}$$

$$AD = \sqrt{R^2 - Kr^2} \tag{6.9}$$

$$\sin\theta = \frac{r}{AD} \tag{6.10}$$

$$DB = \frac{x}{\sin\theta} = AD\,\frac{x}{r}. \tag{6.11}$$

These equations lead to the optical path length (OPL) from the surface of the mirror to the hologram plane

$$OPL = AD - DB. \tag{6.12}$$

The OPL variation across the hologram is the wavefront function or optical path difference (OPD). Choosing the arbitrary reference point as the center, the OPD across the CGH is

$$OPD = OPL - (R - h) \tag{6.13}$$

The CGH is encoded by specifying a phase function for the diffraction to create. For use in the m^{th} order, this CGH will consist of one plotted fringe for every m waves in the phase function. The CGH's for testing the null correctors are used in reflection, so the phase functions must be twice the OPD given above. This gives ring positions for every $m \times \lambda/2$ of the OPD. The radial spacing s of these rings is easily calculated from the grating equation (6.1) as

$$s = \frac{m\lambda}{2\sin\theta}. \tag{6.14}$$

The shape of the OPD function (see Fig 6.5) looks conical with little slope change over most of the CGH. This fortunate shape allows the CGH to work with no carrier at all. The radial slope in the wavefront itself is sufficient to act as a circular carrier with ring spacing nearly constant over most of the hologram (See Fig. 6.6).

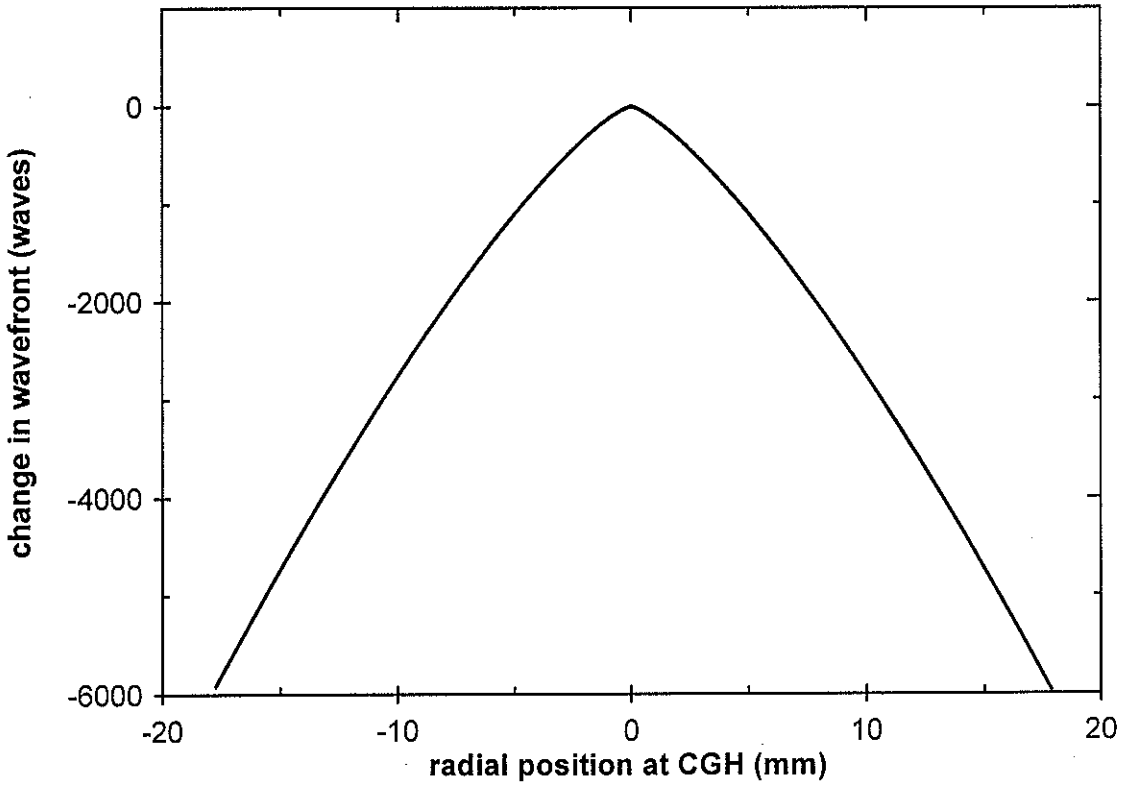

Figure 6.5. Wavefront phase function required of a paraxial-focus CGH to test a null corrector for a 3.5-m $f/1.75$ primary mirror.

The CGH function shown in Fig. 6.5 shows why the conventional method of specifying CGH functions as a power series with even terms fails to converge for designing this hologram. There is a cusp at the center that is poorly modeled using a power series with a reasonable number of terms.

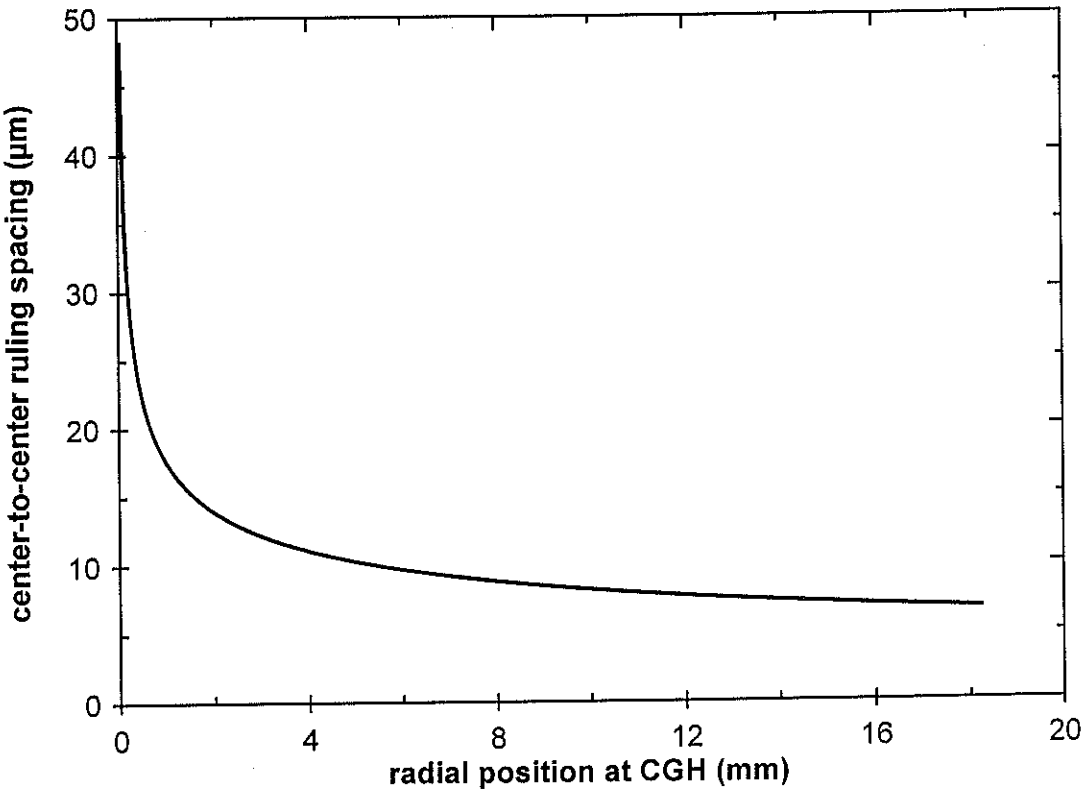

Figure 6.6. Center-to-center groove spacing for a paraxial-focus CGH used in third order to test a null corrector for a 3.5-m $f/1.75$ primary mirror.

The CGH is specified using a computer program to compute the above OPD given the appropriate values for R, K, and h. The software that digitizes the CGH into machine language calls a subroutine to return the phase function given x, the position at the CGH. The subroutine first calculates the corresponding position on the primary mirror r using Newton's method (Arfken 1985). Having found r, the computation of the OPD follows the equations above. Since the equations are exact and no integration is performed, the calculation errors in the floating point operations are negligible.

The common place to put a CGH is at the image of the optic under test to map the optic uniformly onto the hologram. The CGH test of null lenses uses the

hologram at the farthest possible point from an image of the test object, at its focus. The resulting nonlinear mapping causes no problem in the test of the null lens because the light diffracted from the CGH travels back through the null corrector and gets re-mapped to create an image identical to that of a primary mirror. However, the CGH is not focused onto the detector so it must be oversized to avoid edge diffraction.

For the CGH test of null correctors for primary mirrors, the ideal place to put the hologram is at paraxial focus, where $h = 0$. The value of h must never go negative because that would put the CGH in the caustic where the rays are crossing and the mapping from x to r is not single-valued. For positive h, the CGH must become larger with more rings, and thus it becomes more expensive.

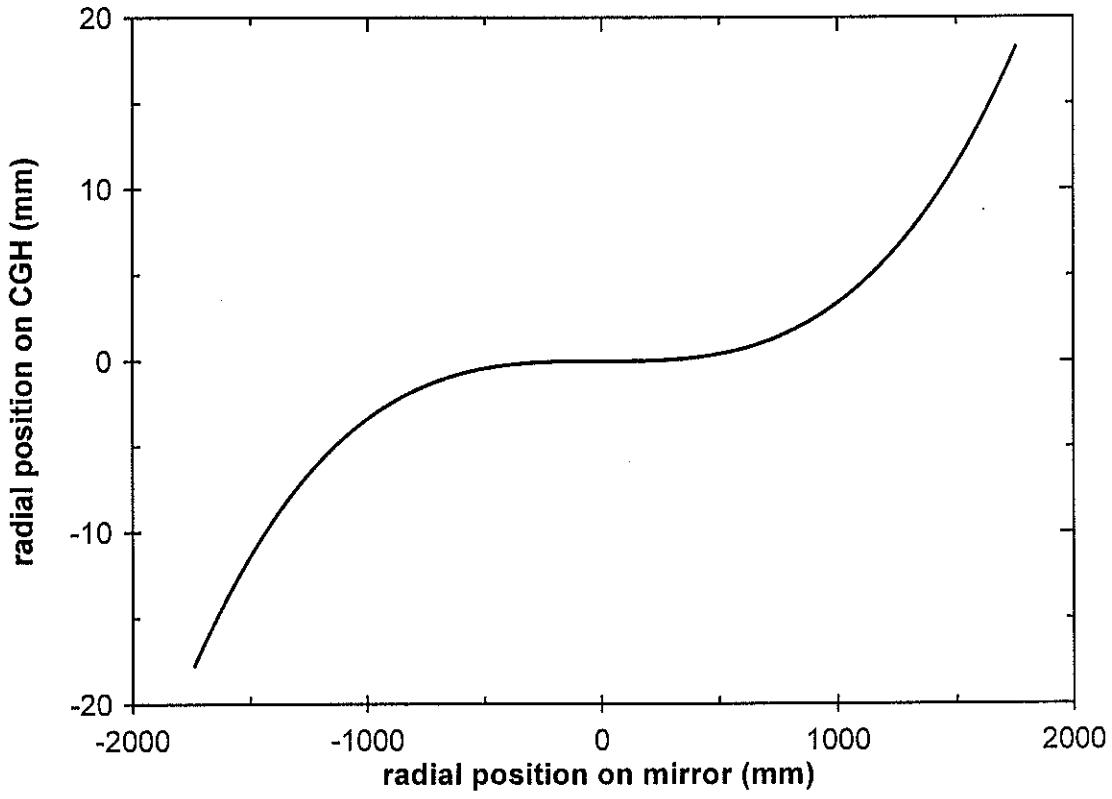

Figure 6.7. CGH mapping function showing the relationship between mirror position and position on hologram. This plot is for a CGH used in third order to test a null corrector for a 3.5-m $f/1.75$ primary mirror.

SERIES EXPANSION FOR ERROR ANALYSIS

For the error analysis, approximations were made by expanding the above equations into power series in r and truncating. The relationship between the radial position on the mirror r and the position on the CGH $x(r)$ is

$$\begin{aligned} x(r) = & \frac{h}{R} r \\ & + \frac{h + hK - KR}{2R^3} r^3 \\ & + \frac{3(1+K)(h + hK - KR)}{8R^5} r^5 + \ldots \end{aligned} \tag{6.15}$$

Likewise, the OPD is approximated by a similar series

$$\begin{aligned} OPD(r) = & \frac{-h}{2R^2} r^2 \\ & + \frac{-3h + K(-4h + 3R)}{8R^4} r^4 \\ & + \frac{-5h + K(-12h + 5R) + K^2(-8h + 7R)}{16R^6} r^6 + \ldots \end{aligned} \tag{6.16}$$

As an end-to-end check of the technique, it is useful to create a CGH of a sphere that can be accurately tested. This CGH can be specified and written in exactly the same manner as a null lens CGH, only $K = 0$ and h must take a positive value.

The truncated series representations used in the error analysis for both the CGH null lens test and the spherical CGH are given in Table 6.1. The relative error

due the series truncations are only a few percent for mirrors slower than $f/1$. Since the error terms themselves are quite small, this error is negligible.

Table 6.1. Approximations to relevant functions for error analysis

CGH to test null lens	Reference CGH of sphere
$h = 0$ $K \cong -1$	$K = 0$
$x(r) \cong \frac{-Kr^3}{2R^2}$	$x(r) \cong \frac{hr}{R}\left(1+\frac{r^2}{2R^2}\right)$
$\sin\theta \cong \frac{r}{R}\left(1+\frac{Kr^2}{2R^2}\right)$	$\sin\theta = \frac{r}{R}$
$spacing \cong \frac{m\lambda R}{2r}\left(1-\frac{Kr^2}{2R^2}\right)$	$spacing = \frac{m\lambda R}{2r}$
$\tan\theta \cong \frac{r}{R}$	$\tan\theta \cong \frac{r}{R}\left(1+\frac{r^2}{2R^2}\right)$
$OPD \cong -\frac{3Kr^4}{8R^3}$	$OPD \cong -\frac{hr^2}{2R^2}\left(1+\frac{3r^2}{4R^2}\right)$

It is interesting that this OPD for the null corrector test has minus three times the aspheric deviation of the primary mirror,

$$Surface\ Asphere \cong \frac{Kr^4}{8R^3}.$$

The surface aspheric departure represents the surface deviation from a reference sphere centered at paraxial focus. The above OPD is the path difference for a real normal ray that intersects the CGH plane.

CGH FABRICATION

The fabrication of CGH's using electron beam lithography is now quite common (Arnold 1989; Urquhart *et al.* 1989). There are firms that specialize in the encoding and printing of CGH's. They have software that evaluates a phase function, usually specified in terms of polynomial coefficients, to create a data file that will drive the plotter. This involves approximating the continuous fringes as chains of trapezoids that the plotter can write (Arnold 1988). The error in making this approximation is negligible if small enough trapezoids are used.

The fabrication of the holograms for testing the null correctors at SOML uses electron beam lithography to write a master, which is then printed to the final substrate. This allows the usual practice of writing the master onto a thin, pre-coated glass slide, while the final CGH transferred to a thick, optically flat glass substrate. This method can severely limit the accuracy of the CGH if the printing is flawed. For this reason, it may be preferable to have the final CGH written directly by the e-beam writer.

The CGH is contact printed by holding the master in direct contact with the photoresist-coated blank and exposing with collimated light. The master can be certified as accurate to ± 0.15 μm, and the errors from well-controlled contact printing are less than ± 0.1 μm (Everett 1993). Since it is difficult to verify the final printing to sub-micron accuracy, an error in the printing could go undetected, leading to an inaccurate optical test.

By using the CGH in third order, the number of rings required to test a null lens is reduced and the smallest feature size is increased by a factor of three, making the part easier to fabricate. To get the desired diffraction efficiency from the third

order, the CGH is made into a pure phase element by etching grooves and coating the entire surface with reflective aluminum.

The steps taken by the diffractive optics firm to produce the holograms for testing null correctors are the following:

1. Encode the phase function into machine language that will drive the e-beam writer.
2. Using electron beam lithography, write the grating pattern into electron resist on the master.
3. Process the exposed master to result in a chrome ring pattern. The exposed resist is dissolved leaving the pattern in resist. The unprotected chrome is then etched.
4. Contact print onto an optically flat substrate and process to result in a $\lambda/20$ flat with the chrome ring pattern on it. The final substrate is coated with chrome and photo resist. The master is held with its chrome pattern in close contact with the resist on the substrate. The pattern is exposed by flooding UV light through the master. The subsequent processing is identical to that in step 3.
5. Ion mill or acid etch to create $\lambda/4$ deep grooves. The chrome bands protect the glass under them.
6. Strip the chrome. This leaves only glass with concentric grooves etched into it.
7. Coat the glass with a thin layer of reflective aluminum.

Since no protective coating is applied, the aluminum will oxidize and is very susceptible to damage.

6.5. OPTIMIZATION OF DIFFRACTION EFFECTS

The holograms are designed to provide a 4% return into the Littrow order to match the intensity of the reference beam. In the Littrow configuration, the diffracted

light rays exactly retrace their path. A spatial filter is positioned at the focus from the Shack cube to reject stray diffractive orders. The size of this pinhole is optimized to provide adequate stray order rejection while passing all of the desired order.

The efficiency of the diffraction ruling is modeled using Fourier optics (Gaskill 1978) based on scalar diffraction theory. Using this method, the far-field diffraction pattern is found by taking the modulus squared of the Fourier transform of the complex amplitude. The light incident onto the ruling is assumed to have uniform intensity and phase, so the complex amplitude is given by the grating function. A general square grating that modulates both phase and amplitude will produce light with a complex amplitude shown in Fig. 6.8.

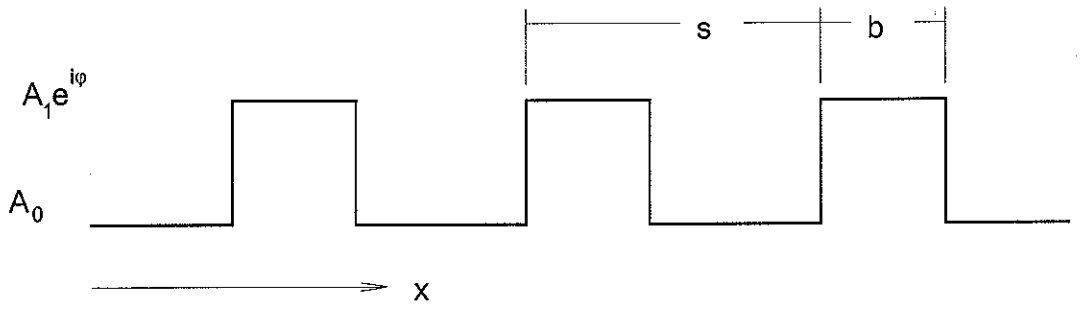

Figure 6.8. Complex amplitude of light modulated by diffraction grating.

The amplitude modulation is given by the square root of the intensity modulation. For example, reflective aluminum ($R = 0.9$) bands on bare glass ($R = 0.04$) would give A_0 of $\sqrt{0.04} = 0.2$, A_1 of $\sqrt{0.9} = 0.95$, and $\varphi = 0$.

Ignoring the finite extent of the ruling, the complex amplitude $u(x)$ is described mathematically, using Gaskill's notation, as

$$u(x) = A_0 + \left(A_1 e^{i\varphi} - A_0\right)\frac{1}{s}\,comb\left(\frac{x}{s}\right) * rect\left(\frac{x}{b}\right), \tag{6.17}$$

where, as illustrated in Fig. 6.8,

A_0, A_1 = amplitudes (square root of intensities) defined by the reflectance of the ruling

φ = phase shift in radians defined by groove etch depth of the diffraction ruling

b = width of a single line in the ruling

s = ruling period or center-to-center spacing.

For an etched ruling that is coated in aluminum and used in reflection, $A_0 = A_1 = \sqrt{0.9}$ and $\varphi = 2 \times 2\pi/\lambda \times depth$. The diffraction efficiency into the ± 1, ± 3, etc. orders is maximized for $\varphi = \pi$, or $\lambda/4$ etch depth.

The Fourier transform of the complex amplitude is

$$U(\xi) = A_0\delta(\xi) + \left(A_1 e^{i\varphi} - A_0\right)\frac{b}{s}\,s \times comb(s\xi) \times sinc(b\xi) \tag{6.18}$$

where ξ, the spatial frequency, is related to the angle of diffraction α by

$$\alpha = \lambda\xi\,. \tag{6.19}$$

The *comb* function gives non-zero values of U for discrete values of ξ, corresponding to the multiple orders of diffraction. These orders occur at integral multiples of 1/s,

$$\xi = \frac{m}{s}\,. \tag{6.20}$$

The relative power η in each order is computed by integrating the squared modulus of the function in Eq. (6.18) over ξ for each order defined by Eq. (6.20). Performing this integration and defining the duty cycle

$$D = \frac{b}{s}, \tag{6.21}$$

the diffraction efficiencies are found to be

$$\begin{aligned} \eta &= A_0^2(1-D)^2 + A_1^2 D^2 + 2A_0 A_1 D(1-D)\cos\varphi \quad (m=0) \\ \eta &= \left[A_0^2 + A_1^2 - 2A_0 A_1 \cos\varphi\right] D^2 sinc^2(mD) \qquad (m \neq 0) \end{aligned} \tag{6.22}$$

Also, the ratio of the imaginary to the real part of the complex amplitude gives the dependence of the phase ψ on duty cycle and amplitude and phase modulation. These relationships, given in Eq. (6.23), are used in a later analysis of the hologram errors:

$$\begin{aligned} \tan\psi &= \frac{A_1 D\sin\varphi}{A_0(1-D) + A_1 D\cos\varphi} \quad (m=0) \\ \tan\psi &= \frac{A_1\sin\varphi}{-A_0 + A_1\cos\varphi} \qquad (m \neq 0) \end{aligned} \tag{6.23}$$

For a reflection grating with D = 0.5, quarter-wave deep grooves, and an aluminum overcoat, the diffraction efficiency into several orders are given in Table 6.2.

Table 6.2. Diffraction efficiency for reflection CGH with Al coating, λ/4 grooves, and 50% duty cycle.

order $\pm m$	diffraction efficiency η into order m
0	0.000

1	0.365
2	0.000
3	0.041
4	0.000
5	0.015
6	0.000
7	0.008

The expressions in Eq. (6.22) were used to analyze the sensitivity of the diffraction efficiency to fabrication errors. Figure 6.9 gives the variation in diffraction efficiency with duty cycle and Fig. 6.10 shows the effect of errors in the etch depth.

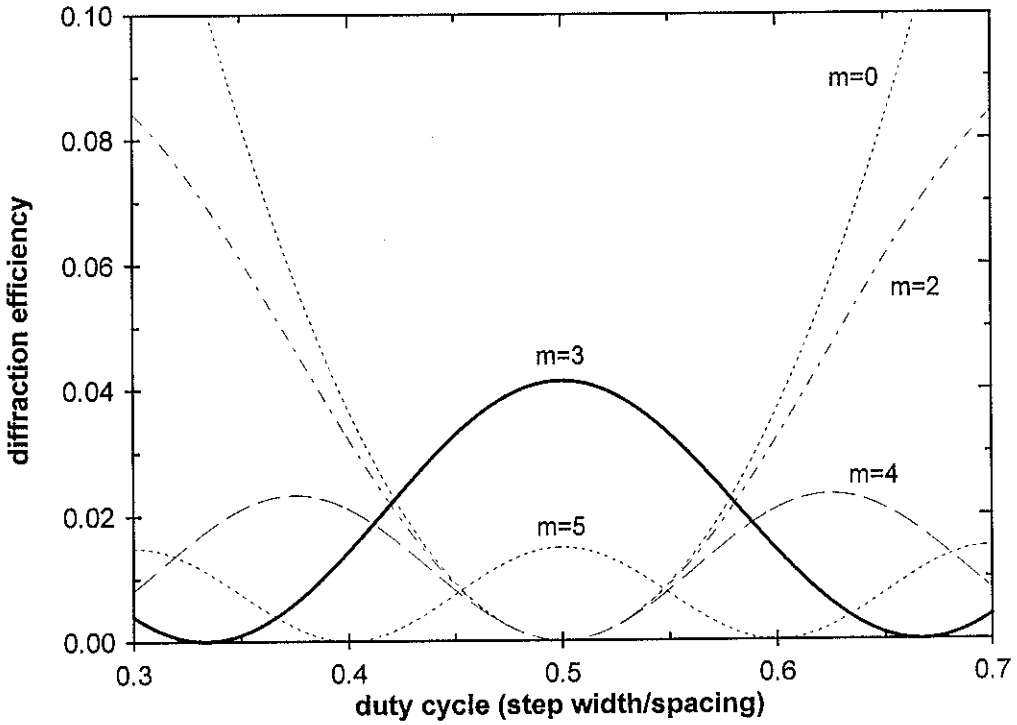

Figure 6.9. Variation in diffraction efficiency η as a function of duty cycle D for a binary phase reflective CGH with an aluminum coating

and quarter wave etch depth. The first-order curve, peaking at 37%, is not shown.

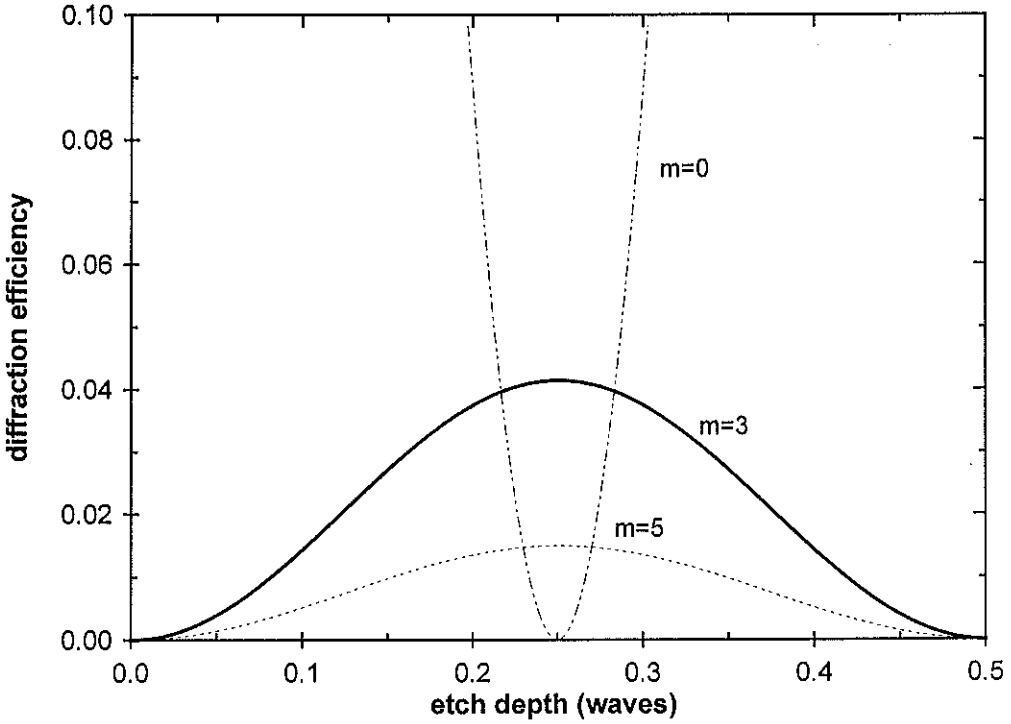

Figure 6.10. Variation in diffraction efficiency η as a function of etch depth for a binary phase reflective CGH with an aluminum coating and 50% duty cycle. All non-zero even orders have zero efficiency. The first-order curve, peaking at 37%, is not shown.

The size of the pinhole is optimized to reject the stray orders without limiting resolution. The pinhole is positioned at the center of curvature of the Shack cube where the light comes to a sharp focus. To find the relationship between pinhole size and order rejection, the null test was analyzed using lens design software. The zero-order diffraction from the CGH was simulated by placing a flat mirror at paraxial focus, where the CGH goes. The ray intercepts at the pinhole plane give the position of the zero-order ray. Since the angle of diffraction is proportional to the order number for small angles and the third-order diffraction is known to cross the axis at

the pinhole, all other orders are easily calculated. This was done for several rays corresponding to different radial positions on the mirror. The pinhole must be small enough that it blocks all but the desired order for the clear aperture tested.

Figure 6.11 shows how a stray order is blocked by the pinhole. The light from the desired order comes to a sharp focus at the pinhole. The unwanted orders are out of focus and aberrated so they do not make it through the aperture. Since an annular pupil is used, an out-of-focus stray order will cause an annular image at the aperture plane. As long as the pinhole is smaller than the inner diameter of this annulus, the light in this stray order will be completely blocked.

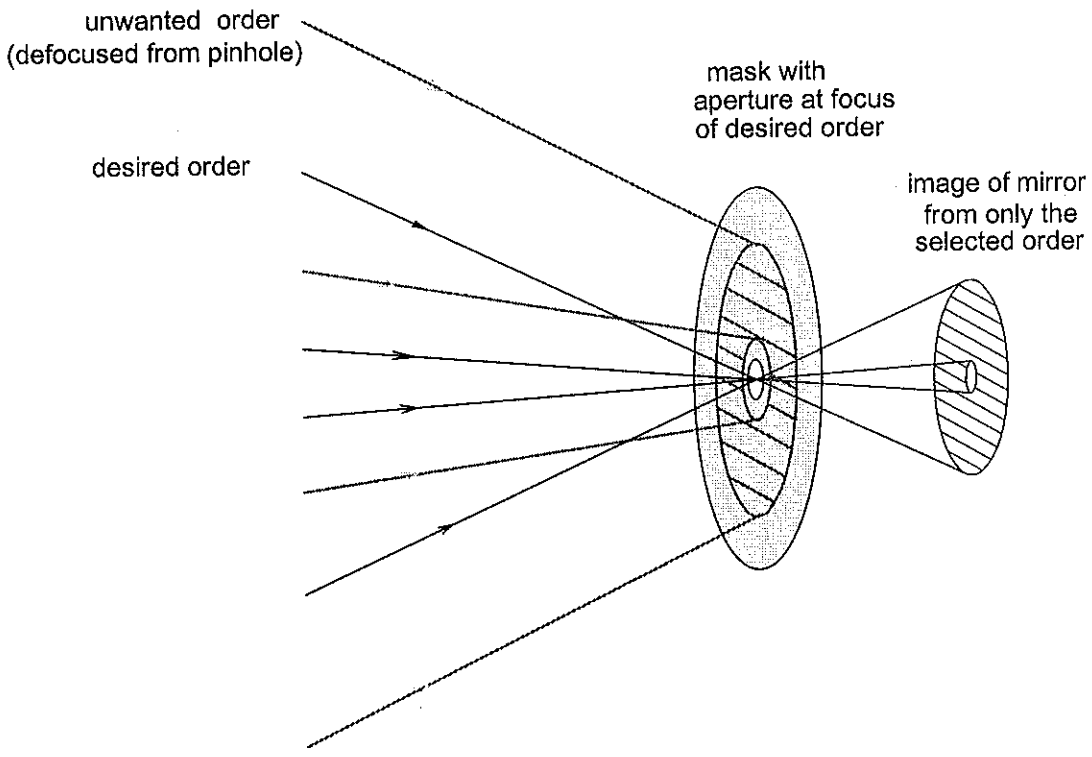

Figure 6.11. Rejection of stray diffraction orders. The order rejection relies on two principles. (1) The desired order comes to a sharp focus where all other orders are out of focus, and (2) An annular pupil is used. There is a central untested region that is blocked elsewhere.

The pinhole may not be made arbitrarily small however because it acts as a low-pass spatial filter with cutoff spatial frequency ξ_c derived using Fourier optics (Goodman 1968; Gaskill 1978) as

$$\xi_c = \frac{NA \times \phi_f}{\lambda D} , \tag{6.24}$$

where ξ_c = spatial frequency of cutoff (cycles per meter at mirror)

ϕ_f = pinhole diameter (μm)

λ = wavelength of light (μm)

D = diameter of primary (meters)

NA = final numerical aperture of converging light in which pinhole is used (equals the sine of the light cone half-angle).

For the null lens for the WIYN 3.5-m primary that uses a 0.332 *NA* beam, a 200-μm pinhole gives 30 cycle-per-meter resolution or 105 full cycles across the mirror diameter. This frequency optimally matches the Nyquist sampling rate determined by the digitization of 200 pixels across the mirror. This pinhole also completely rejects all but the desired orders of diffraction in the clear aperture.

Several high-order diffraction effects were examined and shown to be negligible. The CGH's are designed based on scalar diffraction theory, which is known to be approximate. Rigorous analysis has shown that the diffraction efficiency predicted by this approximation is accurate for rulings with spacings larger than several wavelengths (Moharam and Gaylord 1986; Kok and Gallagher 1988). The angle of the diffracted light predicted by the scalar theory is exact (Gemaux and Gallagher 1993). The phase retardation due to the angle of incidence and the complex

index of refraction of aluminum was analyzed and shown to be negligible. The phase retardation between the s- and the p- polarized light is 0.006λ for the extreme ray for a $f/1.75$ primary. The radial phase variation across the CGH due to the cosine effect in the grooves was also shown to be negligible. For quarter-wave deep grooves, this effect causes an error in W_{040} of only 0.000013λ for an $f/1.75$ primary.

6.6. ERROR ANALYSIS 1: ERRORS FROM FABRICATION OF CGH

The most obvious errors in the CGH null lens test come from the errors in the CGH itself. All of the possible error sources are evaluated and added to estimate the uncertainty in the CGH. The CGH errors can come from the substrate surface figure, e-beam writing errors, printing to the final substrate, or phase etching. They are separated as either figure or hologram errors depending on whether the phase error is caused by the surface reflection or diffraction. The figure errors affect the wavefront from all diffracted orders equally and the effects of the hologram distortion errors on the wavefronts are proportional to the order number. The hologram distortion does not affect the wavefront from the zero-order specular reflection. However, the variations in etch width and depth have a strong effect on the zero-order reflection, but a minimal effect on the other orders.

SURFACE FLATNESS

The figure error in the hologram surface adds a phase error to the diffracted wavefront that is twice the surface error of the CGH. The wavefront phase errors due to small-amplitude low-frequency figure errors are identical for all diffracted orders. In the absence of other errors, this fact would enable the direct measurement of the figure errors using a Fizeau interferometer with a flat reference. The measured figure

errors could then be subtracted from the null lens measurement. However, variations in the etch depth and duty cycle cause irregularities in the zero-order or specular wavefront that are much larger than those in the non-zero-order diffracted wavefronts. The flatness of the CGH substrate must be measured *before* the hologram is applied.

The flatness is measured using the real coordinates of the CGH, so a mapping transformation must be performed to give the resulting error in the null lens test. The nonlinear mapping between CGH and mirror coordinates is shown in Fig. 6.7 and described in Table 6.1. The equation for $x(r)$ in Table 6.1 may be used to transform the figure data from CGH to mirror coordinates. An additional transformation must be performed to correct for the imaging distortion in the null lens (See Sec. 4.6). This remapped surface figure may be subtracted from the data obtained when measuring the CGH with the null lens. An uncertainty in the hologram figure or in the mapping causes an uncertainty in the test of the null lens.

Since the null lens test is performed with the CGH rotated to many azimuthal orientations, non-axisymmetric errors in the CGH average out. The remaining rotationally symmetric surface errors may be expanded in a series and remapped using the relationship for $x(r)$ given in Table 6.1.

If the CGH figure error is written as a polynomial expansion

$$\Delta S = \sum_j a_j x^j$$

the wavefront error mapped into mirror coordinates is

$$\Delta W = 2\sum_j a_j \left(\frac{-KR}{2}\right)^j \left(\frac{r}{R}\right)^{3j} . \tag{6.25}$$

So power ($j = 2$) in the CGH surface ΔS gets mapped into sixth order spherical aberration wavefront error. In practice, the series approximation is not made because

it is more accurate and no more difficult to perform the transformation directly to the data.

The error in the null lens test due to the CGH surface flatness is quite small. The substrates are specified flat to λ/20 at 546 nm and the majority of this error is likely to be astigmatism that is removed from the null lens measurement by rotating the hologram.

HOLOGRAM DISTORTION

The most severe errors in this test are the hologram errors consisting of distortion in the ruling pattern. The distortion may be caused by limitations in the e-beam writing or in the printing onto the final substrate. Distortion causes an error in a diffracted wavefront given by Eq. (6.3). For the null lens test, this error is approximated to be

$$\Delta W = \frac{2\varepsilon_x r}{R}, \tag{6.26}$$

where as before,

ΔW = wavefront error (twice surface error in measurement)

ε_x = radial CGH error (actual radial position of groove - desired position)

r = virtual radial position in mirror coordinates

R = radius of curvature of primary mirror.

The error due to distortion is independent of the order m and wavelength λ.

The effect of the CGH error for the null lens test is analyzed by making the approximations in Table 6.1. The most significant radial error in the CGH is the

linear scale of the hologram which is the lowest-order distortion. A scale error C gives a shift in the pattern ε_x proportional to radial position

$$\varepsilon_x = Cx. \tag{6.27}$$

This causes the diffracted wavefront to have an error of

$$\Delta W = \frac{2r}{R} C\left(-\frac{Kr^3}{2R^2}\right) = -C\frac{Kr^4}{R^3} \tag{6.28}$$

which is simply spherical aberration W_{040}. The conic constant change in the primary mirror that would cause this W_{040} is

$$\begin{aligned} \Delta K &= \frac{4R^3}{r^4} \times W_{040}. \\ &= -4K \times C \end{aligned} \tag{6.29}$$

This result is interesting; it is only the linear component of the CGH distortion, which is a scale error, that causes an error in the measured conic constant. For a more general case, $\varepsilon_x(x)$ may be expanded into a series in x,

$$\varepsilon_x = \sum_j b_j x^j$$

and the resulting wavefront error is

$$\Delta W = 2\sum_j b_j \left(\frac{-KR}{2}\right)^j \left(\frac{r}{R}\right)^{3j+1}. \tag{6.30}$$

The first-order (magnification) term was shown above to introduce spherical aberration into the test. The zero order case is also interesting. If all of the rings are shifted radially an amount b_0, then the wavefront error would take a conical shape.

The magnitude of the hologram errors is estimated from knowledge of the encoding, writing, and printing process accuracy. The CGH encoding is performed with sufficient resolution to insure digitization errors less than the e-beam pixel size. The e-beam writers are verified to be accurate to ± 0.15 μm P-V. The accuracy of the printing depends on the method used and the expertise of the technician. Contact printing has been demonstrated to be accurate to ± 0.1 μm (Everett 1993) although larger errors are expected without using careful control of the process.

The form of the hologram errors determines the type of wavefront errors induced. Most of the encoding and writing errors occur over small spatial scales causing high frequency errors that are filtered out (Kathman *et al.* 1988). Since azimuthal errors average out when rotating the CGH, the error budget must only include spherical aberration. The magnitude of the third-order spherical aberration (which has a fourth-order dependence or r) is estimated by assuming the distortion can cause pure W_{040}. This translates into a scale error given by the maximum shift ε_x divided by the radius of the CGH. The resulting wavefront error is given by Eq. (6.28).

The higher-order spherical aberration is assumed to be much smaller than the low-order error described above. The holograms are written and printed using equipment for making integrated circuits, so the higher-order writing and printing errors should have no tendency to be axisymmetric. An upper limit on the magnitude of the higher-order errors may be obtained assuming all of the grating error occurs where period is minimal. Combining Eqs.(6.3) and (6.14) with the expressions from Table 6.1 and taking the worst case, the maximum wavefront error $\Delta W_{\max}$ is given by

$$\Delta W_{\max} = \frac{2r_{\max}}{R}\left(1 + \frac{Kr_{\max}^{\ 2}}{2R^2}\right) \times \varepsilon_{\max} . \tag{6.31}$$

For the CGH null lens test for a 3.5-m $f/1.75$ primary mirror, a 0.2-μm maximum hologram error can cause a maximum wavefront error of 56 nm.

Unlike most binary optics, these holograms require poor diffraction efficiency, so they can be fabricated using a single step. Binary optics typically use several masks sequentially to increase the diffraction efficiency (Swanson and Veldkamp 1988; Cox *et al.* 1990). With the use of a single mask, the difficulty and uncertainty of the mask alignment are avoided.

ETCHING ERRORS

Variations in the depth of the etched grooves and the ruling duty cycle must also be considered as potential error sources. The dependence of the wavefront phase on these terms, given in Eq. (6.23), shows a strange result for the zero-order diffraction. For diffraction into the zero order from quarter-wave deep grooves, very small variations in duty cycle or groove depth cause large, even discontinuous phase variations. Both the real and imaginary parts of the field amplitude are very small -- zero for the ideal case -- so the ratio of these terms, thus the phase, is poorly defined. The discontinuity in phase for $\lambda/4$ depth and 50% duty cycle is meaningless because there is no energy in this order.

It is apparent from Fig. 6.12 that small fluctuations in duty cycle and etch depth can cause a large diffracted phase variation for the zero-order light. This precludes accurate measurement of the surface flatness using the zero order reflection.

The substrate figure must be certified *before* the hologram is fabricated. The phase of the non-zero orders is unaffected by variations in duty cycle.

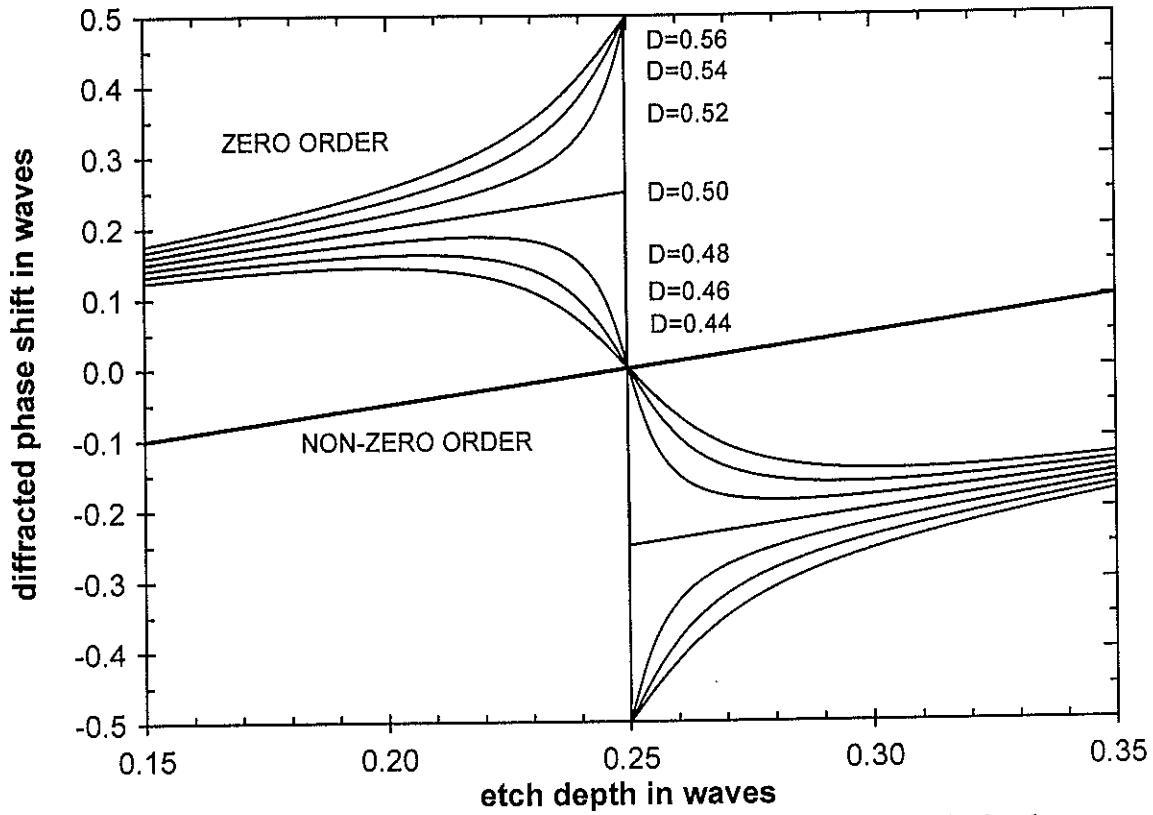

Figure 6.12. Dependence of diffracted phase variation on etch depth and duty cycle variations for a pure phase grating centered around the design values of D=0.5 and 0.25λ etch depth. The zero-order terms are shown as a set of curves with different duty cycles. The non-zero orders have no dependence on duty cycle.

For grooves nominally λ/4 deep, the wavefront variations are equal to the variations in etch depth. Groove depth variation of ±2% will give wavefront errors of ±λ/200.

6.7. ERROR ANALYSIS 2: ERRORS IN USE OF CGH

A CGH manufactured without figure or writing errors does not guarantee a perfect null lens test. The test of the null corrector will only give a null result for a flawless null lens and CGH that are designed for the same radius of curvature, conic constant, and wavelength of light. Also, a change in the temperature of the CGH will cause it to expand and induce spherical aberration. Since the CGH emulates a perfect primary mirror, the alignment does not significantly affect the test accuracy. Noise in the measurements due to vibration, seeing, random electronic noise, and digital round off errors are negligible in the average of many measurements.

The analysis of these effects is handled by treating the CGH as a plane surface that introduces a wavefront change of twice the single-pass OPD given in Table 6.1. This is a sensible thing to do because the ruling is known to introduce three waves of OPD per ring into the third order. Since the measurements are performed in terms of surface variations, this OPD is treated using an effective surface function S_{CGH} which is exactly half of the wavefront change. This surface function is equal to the single-pass OPD given in Table 6.1,

$$S_{CGH} = -\frac{3Kr^4}{8R^3} \tag{6.32}$$

where r is the virtual position at the mirror.

The null lens is designed to measure a mirror with a given radius R and conic constant K, but it will yield a null test for a family of surfaces. The actual shape of the surface depends on the distance to the primary being tested. The CGH test measures only the null corrector, so the measured errors must assume an R and K of the primary mirror. Ideally, the CGH is fabricated for exactly the R and K of the primary. If it is not, corrections to the data must be made for the known differences.

CONIC CONSTANT ERROR

There is a direct relationship between an error in the conic constant and spherical aberration in the null lens. Zernike polynomials are commonly used in interferometric measurement and analysis programs, so the spherical aberration in the surface will be represented by Z_8, the coefficient on Zernike polynomial #8. This polynomial equals $6\rho^4-6\rho^2+1$ where ρ is the normalized radial position. The equation for the surface asphere is differentiated, resulting in

$$\begin{aligned} Z_8 &= \frac{1}{6}\frac{Kr^4}{8R^3} \\ dZ_8 &= \frac{r^4}{48R^3}dK \\ dK &= \frac{48R^3}{r^4}dZ_8 \end{aligned} \tag{6.33}$$

where Z_8 = coefficient on Zernike polynomial #8 for surface asphere

dZ_8 = coefficient on Zernike polynomial #8 when measuring surface with null lens.

For a 3.5-m primary mirror with R = 12250 mm tested using a HeNe laser, $dK = 9.408dZ_8$ (with Z_8 in mm). If the mirror measurement shows dZ_8 = 32 nm, the deviation of the conic constant is +0.0003 from the desired value.

When analyzing data from a CGH null lens test, this relationship must be treated carefully to correctly determine the sign of dK. The spherical aberration measured with a CGH is the error in the null lens. If no spherical aberration is present in a measurement of a primary mirror using the null corrector, the mirror must have a figure error of *the opposite sign* that cancels out that of the null lens. So

for the measurement of a CGH with $\Delta K = K_{primary} - K_{CGH}$, the spherical aberration expected is given by Eq. (6.33)

$$\Delta Z_8 = -\frac{r^4}{48R^3} dK . \tag{6.34}$$

RADIUS OF CURVATURE ERROR

If the CGH and the null lens are designed for different values of R, the primary radius of curvature, the CGH null lens test will show spherical aberration. The relationship between the spherical aberration and R cannot be found directly from Eq. (6.32) since r is actually a function of R.. However, the ratio of r/R is equal to the sine of a ray angle coming from the null lens, so this ratio must not depend on R (since the null lens is determined independently of R). Substituting this into Eq.(6.32) and differentiating gives

$$\begin{aligned} S_{CGH} &= -\frac{3K\sin^4\theta}{8}R \\ \frac{dR}{R} &= -\frac{dK}{K} \end{aligned} . \tag{6.35}$$

So a CGH with $dR = 0.0001R$ will cause spherical aberration that has the same effect as a conic constant change of $+0.0001$ for a parabola. Using the above relationships between ΔK and ΔZ_8, the expected spherical aberration ΔZ_8 due to a small radius change in the null lens is

$$\Delta Z_8 = -\frac{Kr^4}{48R^4}\Delta R , \tag{6.36}$$

where ΔR is defined as $R - R_{CGH}$.

ERROR IN LASER WAVELENGTH

Since diffraction is a strongly wavelength dependent effect, a change in the laser wavelength would cause an error in the measurement. The wavelength of the laser light is dependent on the frequency of the transition for stimulated emission and the refractive index of the air. Using an unstabilized, single-mode gas laser, the frequency can take any value within the Doppler-broadened width of the gain curve. The refractive index of the air is easily calculated based on the temperature and pressure.

The function S_{CGH} is the effective surface corresponding to three waves per cycle at the design wavelength. So S_{CGH} in units of length is really a phase function times the wavelength of the light used. A change in the wavelength must cause a proportional change in S_{CGH},

$$\Delta S_{CGH} = S_{CGH}\frac{\Delta\lambda}{\lambda} = -\frac{3Kr^4}{8R^3}\frac{\Delta\lambda}{\lambda}. \tag{6.37}$$

This leads to

$$\Delta K = 3K\frac{\Delta\lambda}{\lambda} \tag{6.38}$$

and

$$\Delta Z_8 = -\frac{Kr^4}{16R^3}\frac{\Delta\lambda}{\lambda}. \tag{6.39}$$

A +2°C temperature change, causing a refractive index change of -2×10^{-6} (Edlén 1966), causes $\Delta\lambda/\lambda$ of $+2\times10^{-6}$. For testing a null lens for a 3.5-m $f/1.75$ paraboloidal primary mirror, this change in wavelength will cause spherical aberration with $\Delta Z_8 = +0.633$ nm.

ALIGNMENT OF CGH TO NULL LENS

The procedure for aligning the CGH to the null lens is identical to the alignment for the null test of primary mirrors. The lateral translation, axial translation, and tilt of the null lens are adjusted to eliminate tilt, focus, and coma from the interferogram. This is easily done to about an eighth of a fringe and the rest is subtracted in software.

The relationships between the CGH position and the wavefront returned were derived using the functions in Table 6.1 for the null lens test. Since the alignment is performed accurately by nulling the fringes, a first-order analysis is adequate.

Tilt of the CGH about its center by an angle α causes a surface variation $\Delta S = \alpha x$. This is mapped into coma, amounting to

$$\Delta S = \frac{-Kr^3 \cos\theta}{2R^2}\alpha, \tag{6.40}$$

where θ gives the azimuthal angle from the direction of the tilt.

This tilt also causes a shift in the mapping between the CGH and the mirror, but this is a higher order effect that has only 2% of the magnitude given in Eq. (6.40) for an $f/1.75$ primary.

The effect of a lateral shift of the CGH by Δx is analyzed by taking the derivative

$$\Delta S = \frac{dS_{CGH}}{dx}\Delta x. \tag{6.41}$$

This results in wavefront tilt corresponding to

$$\Delta S = \frac{-r\cos\theta}{R}\Delta x. \tag{6.42}$$

Axial motion Δz of the CGH causes two changes: a change in the optical path length (ΔOPL) and a change in the ray mapping onto the CGH. The path length change is computed geometrically and the effect of the remapping is calculated by differentiation of the CGH phase function. These two elements are given as

$$\begin{aligned} \Delta OPL &= -\frac{r^2}{2R^2}\Delta z \\ \frac{dS}{dx}dx &= -\frac{r^2}{R^2}\Delta z. \end{aligned} \tag{6.43}$$

The combination gives

$$\begin{aligned} \Delta S &= \frac{dS}{dx}dx - \Delta OPL \\ &= -\frac{r^2}{2R^2}\Delta z. \end{aligned} \tag{6.44}$$

The amounts of tilt, focus, and coma that are caused by misalignment of the null lens are identical for testing either the CGH or the primary mirror.

RANDOM MEASUREMENT ERRORS

The individual measurements of the CGH have small errors due to environmental effects, electronic noise and digital sampling. These errors become negligible in the average of many measurements since the errors are small in amplitude and uncorrelated. The environmental effects, caused by air motion in the optical path and vibration, are much smaller for the CGH test than they are for the

test of the primary mirror since the path length is so much shorter for the CGH test. For a null lens measurement consisting of 15 azimuthal rotations, 5 maps per angle, and 0.02λ rms random errors, the random component of error in the average is less than 1.5 nm rms, which is negligible.

6.8. ERROR ANALYSIS 3: ERRORS IN DATA REDUCTION

The last remaining type of error is due to possible errors in the interpretation of the data. This type of error is minimized for the null test -- a null result is absolute and requires no interpretation. The actual errors in the null lens and the CGH result in a non-zero figure measurement that must be evaluated. Also, known errors in the CGH that are subtracted from the data cause an uncertainty in the final map from uncertainties in the CGH errors and the mapping between these errors and the measured data.

The errors in the CGH are calculated in the coordinates at the real mirror. To subtract these from the data, the errors must be transformed into the data coordinates. This transformation requires knowing the imaging distortion of the null corrector and the exact relationship between the edge of the data and the edge of the mirror.

The imaging distortion of the null lens is measured to about $\pm 0.5\%$ and the edge is determined to within ± 1 pixel. A computer program was written to re-map the CGH errors according to the imaging distortion and then fit Zernike polynomial coefficients using least squares. The fitting error was directly assessed by simulating errors in the mapping function. For a null lens with -6.7% $\pm$ 0.5% distortion, ΔZ_8, gets mapped into

$$\begin{aligned} \Delta Z_8' &= (0.989 \pm 0.002)\Delta Z_8 \\ \Delta Z_{15}' &= (0.092 \pm 0.008)\Delta Z_8 \end{aligned} \tag{6.45}$$

where ΔZ_8 = coefficient of Zernike #8 in mirror coordinates from CGH errors

$\Delta Z_8'$ = coefficient of Zernike #8 in data coordinates from CGH errors

$\Delta Z_{15}'$ = coefficient of Zernike #15 in data coordinates from CGH errors

(Z_{15} is fifth-order spherical aberration: $20\rho^6 - 30\rho^4 + 12\rho^2 - 1$).

The position of the edge of the image is uncertain by 1 pixel, causing an additional uncertainty in the ΔZ_8 term. For a data map with 200 pixels across the mirror, the relative uncertainty *dr/r* is 1%. This causes an uncertainty in $\Delta Z_8'$ of 4% and an uncertainty in $\Delta Z_{15}'$ of 6%. The uncertainty in mapping the CGH error is independent of the uncertainty in the CGH error itself.

6.9. CONCLUSION

A null lens test using a computer-generated hologram is presented including a background on CGH testing, a detailed description of the CGH null test design and optimization, and a thorough error analysis. This new test works by using the null corrector to test a small circular hologram or zone plate placed at the paraxial focus of the null lens. The zone plate diffracts light back into the null corrector that precisely matches the light that would be reflected by a perfect primary mirror many meters away. An error measured when testing the hologram must be due to the null lens.

The CGH null lens test is used to certify a critical and precise instrument, so a thorough error analysis has been performed. The test has three types of error sources: errors in the CGH, errors in the implementation of the test, and errors in the interpretation of the results. An effort has been made to understand and minimize all three types of errors.

APPENDIX C

VISIBLE NULL CORRECTOR FOR A 6.5-m *f*/1.25 PRIMARY MIRROR: OPTICAL PRESCRIPTION AND TOLERANCE ANALYSIS

This appendix contains the optical prescription and error analysis for the null corrector designed for testing a 6.5-m *f*/1.25 primary mirror using visible laser light. The null corrector, shown in Fig. C.1 will be used to guide final polishing of the primary mirror. The error budget for the null corrector is analyzed using a structure function of the mirror surface. The structure function contributions from the null lens tolerances, after the removal of conic constant errors, are shown in Table C.1. The error analysis using rms wavefront is given in Table C.2.

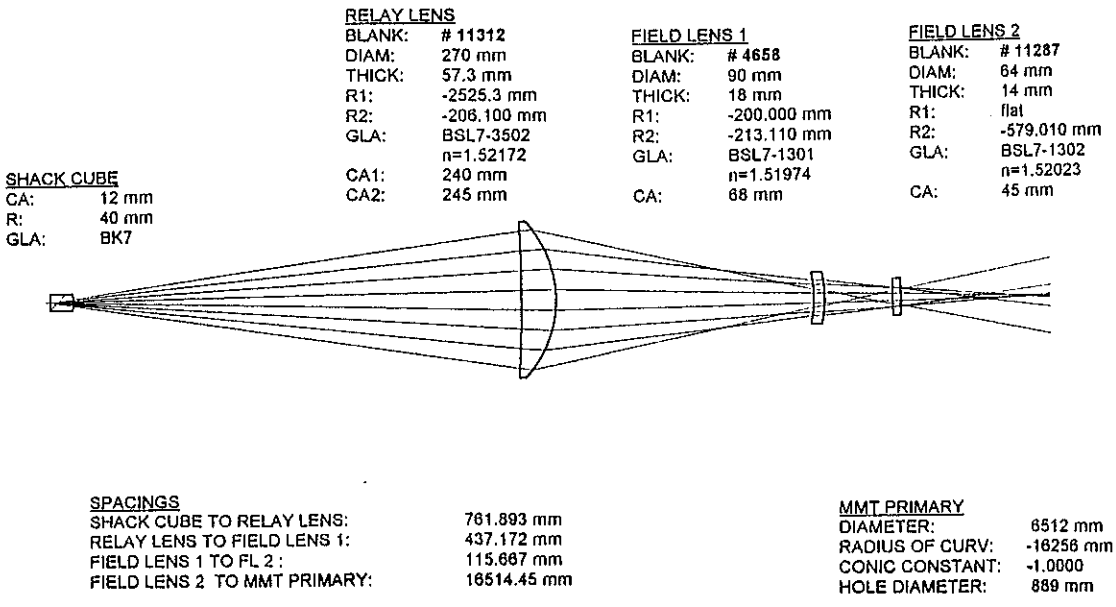

Figure C.1. Layout of the visible null corrector for the 6.5-m *f*/1.25 primary mirrors.

Table C.1. Table of tolerances showing the structure function for the null corrector

				STRUCTURE FUNCTIONS						
		Design		spatial scales in mm						
	units	value	tolerance	3256	1628	814	407	204	102	51
				rms wavefront difference in nm						
Shack Cube	mm	12								
Radius	mm	-40	0.005	0.30	0.26	0.12	0.23	0.20	0.12	0.06
Surface (rms)	nm		6.328	17.59	16.58	12.28	8.35	5.19	2.78	1.28
Runout	µm		5.000	1.98	1.64	2.11	1.14	0.89	0.62	0.34
Airspace	mm	761.893	0.020	1.21	1.04	0.47	0.90	0.80	0.48	0.26
Relay Lens :	mm	270								
Radius 1	mm	-2525.3	0.500	1.20	0.94	0.46	0.93	0.85	0.51	0.27
Thickness	mm	57.3	0.010	0.78	0.70	0.53	0.63	0.49	0.29	0.16
Radius 2	mm	-206.1	0.010	2.50	2.35	1.05	1.61	1.53	0.93	0.50
Surface 1 (rms)	nm		7.594	10.87	10.25	7.59	5.16	3.21	1.72	0.79
Surface 2 (rms)	nm		7.594	10.87	10.25	7.59	5.16	3.21	1.72	0.79
Index of refraction		1.52172	1.00E-5	1.13	0.99	0.12	0.74	0.76	0.46	0.25
Index Inhomogen	rms		1.72E-7	27.79	13.90	6.95	3.47	1.74	0.87	0.43
Runout surface 1	µm		10.000	1.68	1.54	2.24	1.21	0.96	0.67	0.36
Runout surface 2	µm		10.000	2.67	2.21	2.71	1.56	0.87	0.64	0.35
Airspace	mm	437.172	0.020	1.86	0.47	1.46	1.73	1.77	1.07	0.56
Field Lens 1:	mm	90								
Radius 1	mm	-200	0.005	7.68	7.92	5.52	4.81	3.93	2.36	1.29
Thickness	mm	18	0.005	1.48	3.28	3.63	1.36	2.12	1.31	0.68
Radius 2	mm	-213.11	0.005	3.30	4.96	4.85	0.66	2.27	1.41	0.71
Surface 1 (rms)	nm		7.594	10.87	10.25	7.59	5.16	3.21	1.72	0.79
Surface 2 (rms)	nm		7.594	10.87	10.25	7.59	5.16	3.21	1.72	0.79
Index of refraction		1.51974	1.00E-5	0.28	0.18	0.49	0.26	0.24	0.16	0.08
Index Inhomogen	rms		1.20E-7	6.09	3.05	1.52	0.76	0.38	0.19	0.10
Runout surface 1	µm		5.000	38.75	27.06	20.12	13.98	8.28	4.57	2.41
Runout surface 2	µm		5.000	33.66	24.31	18.29	12.77	7.66	4.24	2.23
Airspace	mm	115.667	0.010	1.77	1.28	0.95	1.31	1.34	0.81	0.43
Field Lens 2:	mm	64								
Curvature 1	/mm	0	1.25E-7	6.46	8.31	7.45	2.83	2.02	1.32	0.60
Thickness	mm	14	0.010	1.51	1.23	0.41	1.08	1.05	0.64	0.34
Radius 2	mm	-579.01	0.010	1.86	0.64	1.69	1.56	1.69	1.03	0.54
Surface 1 (rms)	nm		7.594	10.87	10.25	7.59	5.16	3.21	1.72	0.79
Surface 2 (rms)	nm		7.594	10.87	10.25	7.59	5.16	3.21	1.72	0.79
Index of refraction		1.52023	1.00E-5	4.00	3.94	2.31	2.53	2.24	1.36	0.73
Index Inhomogen	rms		1.20E-7	4.74	2.37	1.18	0.59	0.30	0.15	0.07
Runout surface 1	µm		5.000	20.73	14.64	10.82	8.05	5.25	3.03	1.65
Runout surface 2	µm		5.000	24.75	16.62	11.53	8.02	4.99	2.81	1.49
Airspace	mm	16514.4	1.000	1.07	0.94	0.37	0.63	0.70	0.43	0.23
MMT Primary	mm	6512								
Radius	mm	16256	1.000							
Design Residual	λ	0	0.008	6.77	6.64	7.84	6.26	4.22	2.35	1.20
Worst Case				290.85	231.47	174.99	120.94	83.95	47.92	24.35
RSS WVFRONT				75.77	56.37	41.86	28.78	18.44	10.34	5.30
RSS SURFACE				**37.89**	**28.18**	**20.93**	**14.39**	**9.22**	**5.17**	**2.65**

Table C.2. Table of tolerances showing the dependence of the rms wavefront and conic constant on the fabrication tolerances.

	units	Design value	tolerance	Conic Constant error	Wavefront rms at 514.5 nm
Shack Cube	mm	12			
Radius	mm	-40	0.005	0.000005	0.0006
Surface Irregularity (rms)	wv HeNe		0.010		0.0246
Runout	µm		5.000	0.000000	0.0013
Airspace	mm	761.893	0.020	0.000018	0.0017
Relay Lens :	mm	270			
Radius 1	mm	-2525.3	0.500	0.000019	0.0016
Thickness	mm	57.3	0.010	0.000008	0.0011
Radius 2	mm	-206.1	0.010	0.000011	0.0030
Surface 1 Irregularity (rms)	wv HeNe		0.012		0.0154
Surface 2 Irregularity (rms)	wv HeNe		0.012		0.0154
Index of refraction		1.52172	1.00E-5	0.000025	0.0013
Index Inhomogeneity	rms dn		1.72E-7		0.0383
Runout surface 1	µm		10.000	0.000000	0.0026
Runout surface 2	µm		10.000	0.000000	0.0019
Airspace	mm	437.172	0.020	0.000071	0.0045
Field Lens 1:	mm	90			
Radius 1	mm	-200	0.005	0.000034	0.0105
Thickness	mm	18	0.005	0.000025	0.0079
Radius 2	mm	-213.11	0.005	0.000029	0.0101
Surface 1 Irregularity (rms)	wv HeNe		0.012		0.0153
Surface 2 Irregularity (rms)	wv HeNe		0.012		0.0153
Index of refraction		1.51974	1.00E-5	0.000001	0.0002
Index Inhomogeneity	rms dn		1.20E-7		0.0084
Runout surface 1	µm		5.000	0.000000	0.0300
Runout surface 2	µm		5.000	0.000000	0.0308
Airspace	mm	115.667	0.010	0.000036	0.0032
Field Lens 2:	mm	64			
Curvature 1	/mm	0	1.25E-7	0.000009	0.0147
Thickness	mm	14	0.010	0.000023	0.0023
Radius 2	mm	-579.01	0.010	0.000002	0.0046
Surface 1 Irregularity (rms)	wv HeNe		0.012		0.0154
Surface 2 Irregularity (rms)	wv HeNe		0.012		0.0154
Index of refraction		1.52023	1.00E-5	0.000002	0.0051
Index Inhomogeneity	rms dn		1.20E-7		0.0065
Runout surface 1	µm		5.000	0.000000	0.0140
Runout surface 2	µm		5.000	0.000000	0.0184
Airspace	mm	16514.45	1.000	0.000060	0.0011
MMT Primary mirror	mm	6512			
Radius	mm	16256	1.000		
Null Corrector residual	waves	0	0.008	0.000000	0.0079
Worst Case				0.000377	0.3503
RSS				**0.000121**	**0.0815**

APPENDIX D

INFRARED NULL CORRECTORS USING ASPHERIC SURFACES: OPTICAL PRESCRIPTION AND TOLERANCE ANALYSIS

This appendix contains the optical prescriptions for two IR null lenses that each use a single aspheric surface. The first optical design, shown in Fig. D.1, is of limited practical value because of its extreme sensitivity to manufacturing errors. The second null corrector, shown in Fig D.2, will be used to test the MMT primary mirror. A complete tolerance table for this null corrector is given in Table D.1.

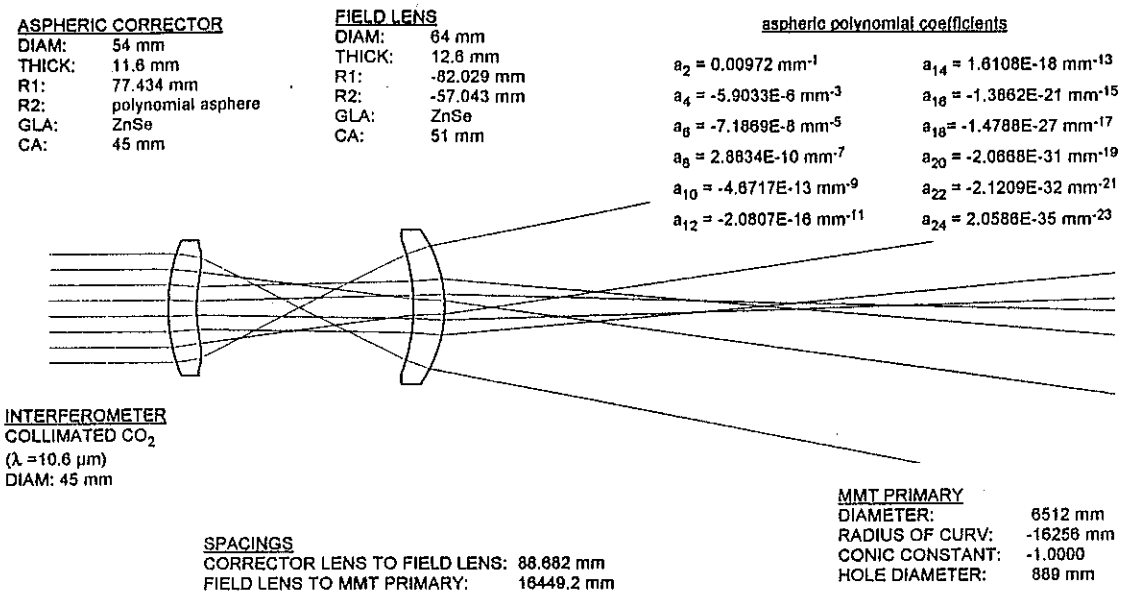

Figure D.1. Layout with prescription of an interesting infrared null corrector for a 6.5-m $f/1.25$ primary mirror.

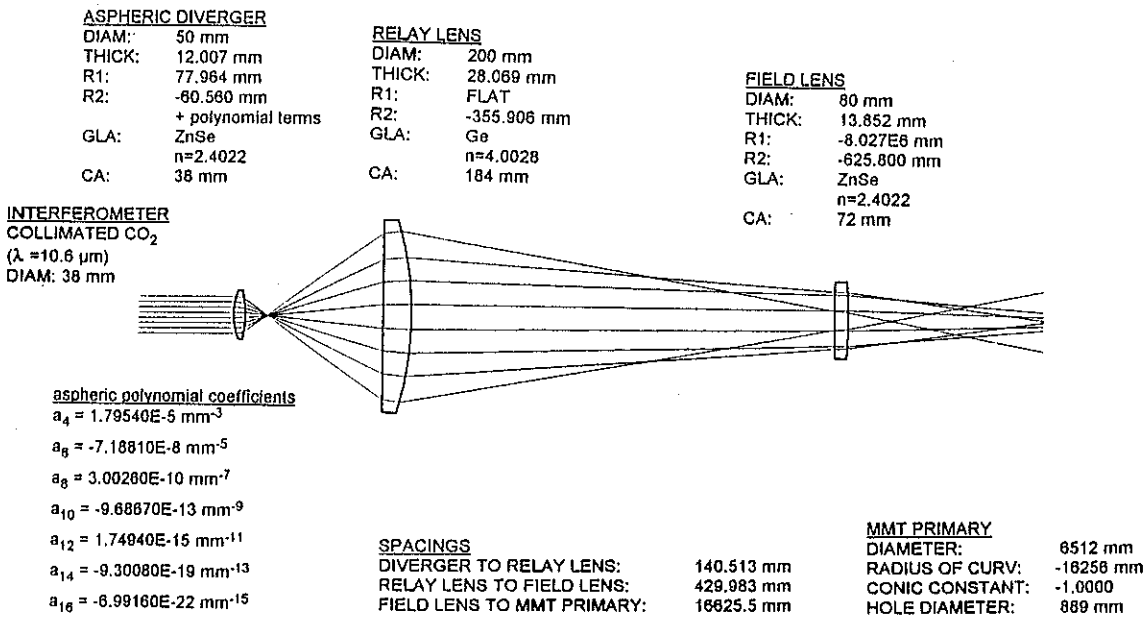

Figure D.2. Layout with prescription of the infrared null corrector that will be used for testing the 6.5-m $f/1.25$ primary mirrors.

Table D.1. Table of tolerances for the MMT IR null corrector.

	units	Design value	tolerance	Conic Constant error	Wavefront rms (at 10.6 μm)
Interferometer	mm	38			
Power	μm	0	0.000	0.000000	0.0000
Reference surface (rms)	wv HeNe		0.01	0.000000	0.0012
Alignment w/null	deg		0.100	0.000000	0.0018
Aspheric Diverger	mm	50			
Radius 1	mm	77.964	0.05	0.000020	0.0032
Thickness	mm	12.007	0.04	0.000000	0.0016
Radius 2	mm	-60.56	0.025	0.000012	0.0028
Surface 1 Irregularity (rms)	wv HeNe		0.5	0.000000	0.0837
Surface 2 Irregularity (rms)	wv HeNe		0.1	0.000000	0.0167
Index of refraction (ZnSe)		2.4022	0.0005	0.000006	0.0031
Index Inhomogeneity	rms dn		3.00E-06	0.000000	0.0068
Runout surface 1	μm		50	0.000000	0.0014
Runout surface 2	μm		50	0.000000	0.0056
Decenter surface 2	μm		50	0.000000	0.0153
Airspace	mm	140.513	0.050	0.000068	0.0089
Relay Lens :	mm	200			
Curvature 1	/mm	0	5.00E-07	0.000030	0.0034
Thickness	mm	28.069	0.050	0.000023	0.0026
Radius 2	mm	-355.906	0.100	0.000036	0.0069
Surface 1 Irregularity (rms)	wv HeNe		0.1	0.000000	0.0359
Surface 2 Irregularity (rms)	wv HeNe		0.1	0.000000	0.0359
Index of refraction (Germanium)		4.0028	1.00E-3	0.000038	0.0066
Index Inhomogeneity	rms dn		5.00E-5		0.2648
Runout surface 1	μm		50	0.000000	0.0220
Runout surface 2	μm		50	0.000000	0.0337
Airspace	mm	429.983	0.100	0.000062	0.0056
Field Lens :	mm	80			
Curvature 1	/mm	1.25E-07	1.00E-6	0.000077	0.0139
Thickness	mm	13.852	0.020	0.000005	0.0005
Radius 2	mm	-625.8	0.100	0.000020	0.0037
Surface 1 Irregularity (rms)	wv HeNe		0.1	0.000000	0.0167
Surface 2 Irregularity (rms)	wv HeNe		0.1	0.000000	0.0167
Index of refraction (ZnSe)		2.4022	0.0005	0.000044	0.0081
Index Inhomogeneity	rms dn		3.00E-06	0.000000	0.0078
Runout surface 1	μm	50	50	0.000000	0.0096
Runout surface 2	μm	50	50	0.000000	0.0147
Airspace	mm	16625.5	1.000	0.000060	0.0000
MMT Primary mirror	mm	6512			
Radius	mm	16256	1.000		
Null Corrector residual	waves	0	0.008	0.000000	0.0076
Worst Case				**0.000500**	**0.6686**
RSS				**0.000158**	**0.2888**

Null test optics for the MMT and Magellan 6.5-m $f/1.25$ primary mirrors

J. H. Burge, D. S. Anderson, D. A. Ketelsen, and S. C. West

Steward Observatory Mirror Lab
University of Arizona
Tucson, Arizona 85721

ABSTRACT

The instruments used to interferometrically measure the optical surfaces of the 6.5-m $f/1.25$ primary mirrors for the MMT conversion and Magellan Telescopes must compensate over 800 μm surface departure from the best fitting sphere. The errors in the optical test must not contribute more than 0.04 arc seconds FWHM to the final image and the conic constant must be held to 0.01%. This paper presents the design, analysis, fabrication, and certification of the instruments used to measure these giant mirrors to such high accuracy.

1. INTRODUCTION

Primary mirrors for modern telescopes are tested interferometrically from the center of curvature using null correctors (see Fig. 1). The null corrector, or null lens, compensates for the asphericity of the mirror surface. Interferometric testing with a null lens allows an accurate, high-resolution measurement of the entire surface that can be made in several minutes. Two instruments are being built for interferometric measurements of the 6.5-m mirrors at the Steward Observatory Mirror Lab (SOML). An infrared interferometer with a germanium and ZnSe null corrector will test the ground surface to monitor loose-abrasive grinding. The polished surface will be measured with green laser light using a Shack cube interferometer co-aligned with a BK7 null corrector. Both the infrared and visible systems have been carefully designed to give excellent performance in terms of wavefront correction, alignment sensitivity, imaging of the mirror to the detector, diffraction effects, ghost reflections, and ease of use. The lenses for these instruments are fabricated and measured precisely. The accurate alignment and stable support of these lenses require a well designed and constructed mechanical system. The mounting and alignment methods used for the new null correctors follow from the experience of building similar, smaller instruments at Steward Observatory.[1]

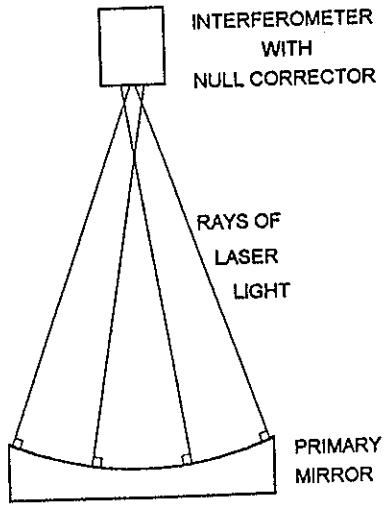

Figure 1. Schematic drawing of null test.

An optical test for measuring null correctors has been developed that uses a rotationally symmetric computer-generated hologram (CGH) to synthesize the wavefront that would be reflected by a perfect primary mirror. The test of a null lens is performed by measuring the CGH through the null corrector. Since the CGH is made independently from the null corrector, agreement between the null lens and the CGH indicate that both the null lens and the CGH are correct. This test is planned for both null correctors for the 6.5-m mirrors.

in *Advanced Technology Optical Telescopes V*, L. M. Stepp, Editor, Proc. SPIE 2199, in press (1994).

2. INTERFEROMETRIC METROLOGY USING NULL CORRECTORS

2.1 DESCRIPTION OF NULL TEST

The interferometric null test uses interference between light that has been reflected from the mirror, and light from a reference surface. The interferometer creates a spherical wavefront of laser light that is split into a reference and a test beam. The test beam travels through the null corrector, reflects off the mirror under test, and travels back through the null corrector into the interferometer. The test is autostigmatic -- the light retraces its path to form a point image coincident with the source point. The reference beam is reflected off a high-quality spherical or plano surface. The test beam is recombined with the reference beam causing an interference fringe pattern that corresponds to the difference between the two wavefronts. The fringe pattern is imaged onto a detector for analysis. By simultaneously shifting the reference beam and measuring the change in intensity at each pixel of the image, the phase difference, which is proportional to the surface error of the mirror, is calculated at each sampled location.

The null corrector is designed to modify the spherical wavefront from the interferometer to produce a wavefront that matches the desired aspheric shape of the mirror. If both the null lens and the mirror are perfect, this test wavefront will exactly match the reference wavefront. The resulting interference pattern will show no variation, giving a "null" result (no surface error). If the mirror does have figure errors, they will be imparted to the reflected wavefront and show up in the interference pattern. Errors in the reflected wavefront are exactly twice the size of the errors in the mirror. It is important to note that any error in the null corrector will cause a shape change in the test wavefront that will be interpreted as a figure error in the mirror. The null test simply measures how well the mirror fits the template created by the null corrector. It requires additional testing to determine the absolute accuracy of this template.

Of the several types of null correctors shown in Fig. 2, the Offner null lens is most commonly used for large modern primary mirrors because it allows the measurement of fast primaries to high accuracy and with reasonable manufacturing tolerances. This null corrector consists of a large relay lens and a smaller field lens. The design principle of the null corrector uses the field lens to image the primary mirror onto the relay lens. The power and shape of the relay lens are chosen to introduce spherical aberration that compensates the asphericity of the primary mirror. The optimization of the two-element Offner null corrector is discussed by Offner[5], Holleran[6], Puryaev and Shandin[7], Moya and Landgrave[8], Sasian[9,10], DeVoe[11], Offner and Malacara[12], and Shafer[13].

The design of the null test requires more than an accurate null corrector. The instruments are complex optical systems with illumination, wavefront correction, and imaging optics. The wavefront correction is performed by the null lens. The illumination optics project a laser beam through a spatial filter to give a well-conditioned wavefront. The imaging optics project the interference pattern as a scaled image of the primary mirror onto the detector plane.

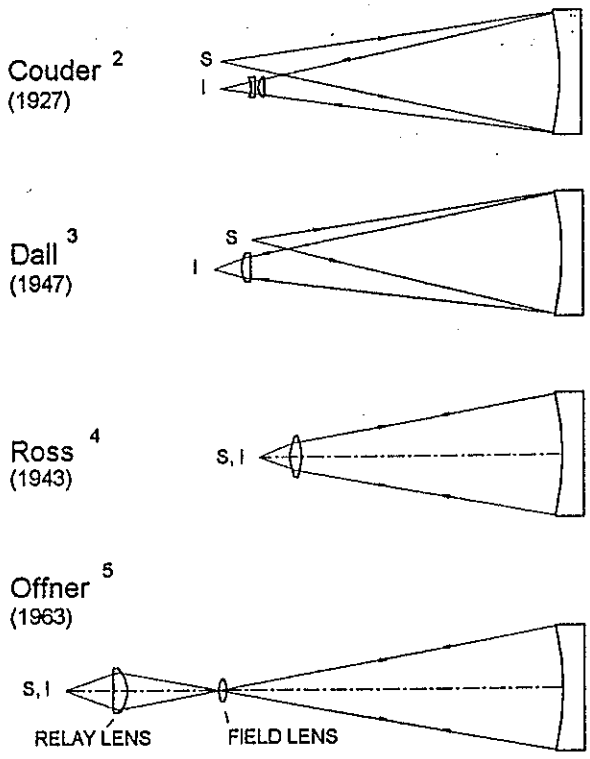

Figure 2. Types of refractive null correctors used for testing primary mirrors.[2,3,4,5] These drawings are schematic and not to scale.

2.2 IMAGING REQUIREMENTS

During grinding and polishing, the data from the infrared and visible interferometers are used to direct the figuring. It is important to minimize the mapping distortion of the mirror through the null lens. The imaging distortion causes two problems in the data analysis; it causes small surface defects to appear shifted radially and it re-maps low order errors from alignment (focus, and coma) into higher order errors. A discussion of interferometric measurement errors introduced by small amounts of distortion is given by Selberg[14] and the details of the effects of distortion in the null test are given by Burge[1]. The infrared null lens

was designed to have minimal mapping error and the visible system uses relay optics to correct the distortion introduced by the null lens.

Improper imaging causes diffraction "ripples" in the measured phase and causes the edge of the mirror to appear flawed. This effect, and other errors from diffraction, are minimized by focusing the mirror onto the detector array. Both of the interferometers use apertures at intermediate images of the primary to help define the focus. Also, a rotating ground glass disk correctly positioned in the visible system eliminates Fresnel noise, which is caused by scatter of the coherent laser light from dust on the lens surfaces. Both null correctors were designed to avoid ghost reflections that can cause troublesome spurious fringes.

2.3 ALIGNMENT OF TEST OPTICS WITH PRIMARY MIRROR

Since this is an autostigmatic test, the shape of the wavefront created by the null corrector defines the shape of the mirror. For a given null lens and spacing to the primary mirror, the shape of the mirror is fully determined by the shape of the wavefront. It is easy in practice to align the null lens with respect to the mirror because the different alignment degrees of freedom cause distinct changes in the interference pattern. To find the correct null lens position and orientation with respect to the mirror, the null lens is first positioned approximately to get the light to reach the detector. Fine adjustments are made to eliminate the fringes of tilt, focus and coma. Interferograms of these characteristic aberrations are shown in Fig. 3. Lateral translation of the null lens causes straight tilt fringes in the interferogram. Vertical translation along the axis causes focus in the interferogram. Rotation of the null corrector about the paraxial center of curvature causes coma in the interferogram. Since it is easy to differentiate tilt, coma, and focus in an interferogram by inspection, the alignment is done quickly and easily.

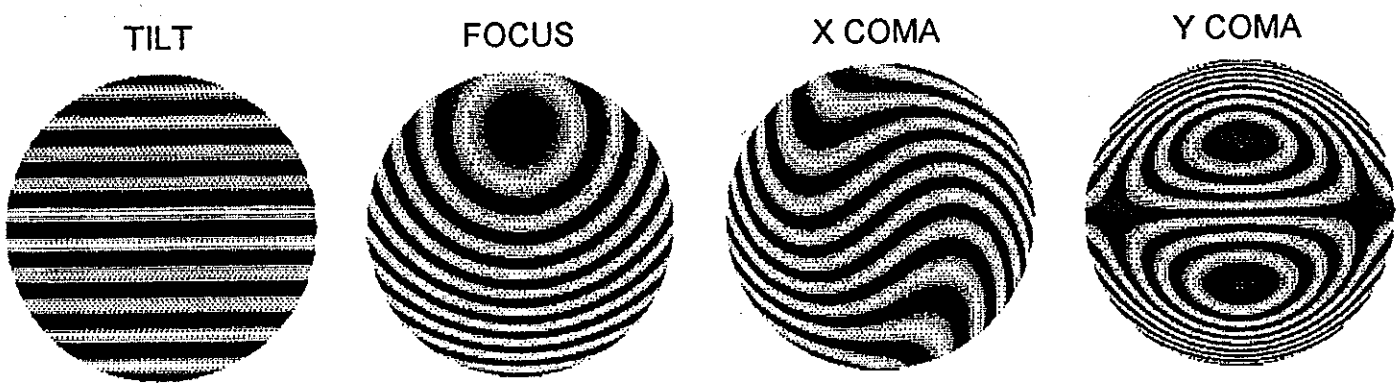

Figure 3. Interferograms showing alignment errors of tilt, focus, and coma. Some tilt has been added to the focus and coma.

A small amount of residual alignment error always exists and must be removed in the data analysis. About a tenth of a fringe of tilt, focus, or coma often remains after alignment. Any small mechanical instabilities will also cause small variations of these aberrations. Since tilt, focus, or coma measured in the mirror comes from test misalignment and because these aberrations do not affect the telescope operation, they are always removed in the data analysis. These low-order terms are easily removed by first fitting Zernike polynomials to the raw data and then subtracting the appropriate terms from the data.

A tolerance is imposed on the primary radius of curvature to insure that the null lens is used at the correct distance from the primary mirror. The null corrector creates a wavefront that propagates to fit the desired shape of the mirror. Since the wavefront changes as it propagates, there is a family of different surfaces that will give a null test, only one of which has the desired shape. Each member of the family can be described to fourth-order in radial position r by specifying a radius of curvature R and conic constant K. In practice, the null lens is moved axially to eliminate power in the reflected wavefront. The distance at which this condition is satisfied depends on R. Therefore the conic constant of the surface matching the wavefront depends on R. The change in K is related to the change in R by

$$\frac{\Delta K}{K} = -\frac{\Delta R}{R}. \tag{1}$$

The radius of curvature R is inferred from a direct measurement of the distance between the null corrector and the primary mirror. The optician monitors this distance and designs the grinding and polishing strokes to keep the radius within tolerance.

The null test is also insensitive to optical surface decentration and tilt with respect to the axis defined by the null corrector. These pose no real problem as long as the decentration and wedge of the optical surface with respect to the 6.5-m blank are less than 1 mm, which can be accommodated in the telescope. The wedge is measured by rotating the mirror about the mechanical reference axis, and measuring runout in the optical surface. The decentration is determined from the amount of coma seen in the null test when the mirror is rotated about is mechanical axis. The centration and wedge of the optical surface are largely determined during generating. Since little material is removed during grinding and polishing, only small changes are made in the mechanical properties of the mirrors.

2.4. ENVIRONMENTAL EFFECTS

Since the measurements of the optical surfaces are performed using instruments many meters away, environmental effects can cause significant errors. Variations in air density can cause both random and systematic errors. Motion of the interferometer or the mirror due to vibration makes phase shifting interferometry difficult and introduces random errors in the measurement. The random errors are reduced to an acceptable level by averaging many measurements, but systematic errors remain and degrade the test accuracy.

The random testing errors are minimized by the design of the test facility and further reduced by averaging. Vibration and air motion (seeing) are the dominant sources of random variations in the testing of large optics. These errors are kept as small as possible by using a large, well-controlled lab and vibration-isolated test tower. The remaining random measurement errors are reduced by averaging large numbers of measurements. The error in the average due to the random, uncorrelated effects decreases as the square root of the number of measurements in the average.

Measurement errors due to vibration are minimized by using an isolated test tower, short integration times, and testing on a null fringe. The testing of primary mirrors at Steward Observatory is performed on a rigid test tower that is isolated from ground vibrations by pneumatic supports (see Fig. 4). This test tower is 24 meters tall and weighs 400 tons. It moves as a rigid body with a resonance of about 1.2 Hz, and lowest internal mode is at 9.5 Hz. The tower isolation reduces the vibration problem to a level that allows phase shifting interferometry, although with some difficulty. The use of a shuttered CCD camera that captures images using very short exposures freezes out fringe vibration during each frame. However, the relative motion between the mirror and the interferometer between frames introduces a measurement error. The error in the phase computation due to vibration is roughly proportional to the spatial phase variation of the surface under test. For a good surface with the system aligned on null fringe, the test surface shows very little spatial variation so the effects of vibration are minimized. A great attribute of the null test is that the testing becomes more accurate as the figure of the mirror improves.

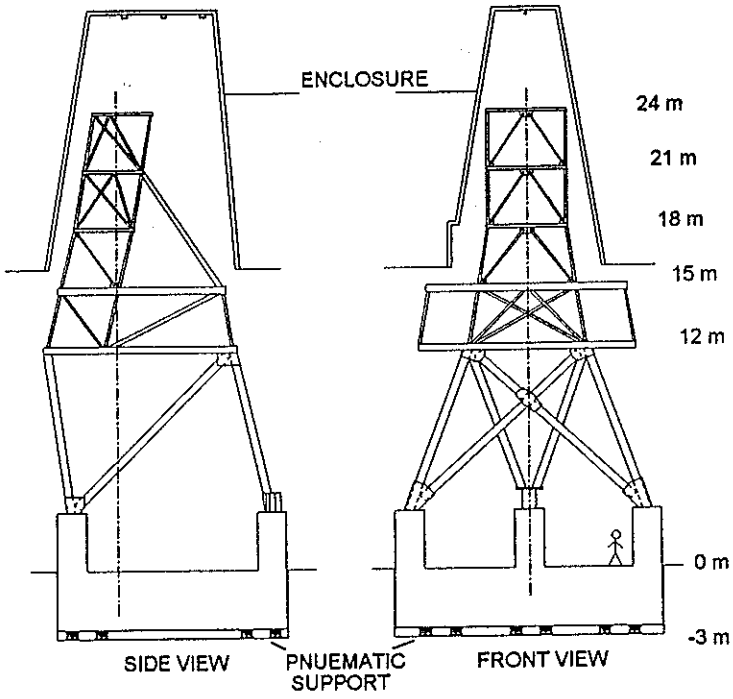

Figure 4. Isolated test tower at Steward Observatory Mirror Lab. The entire 400-ton concrete and steel structure is supported by 40 air-filled isolators. Drawing by E. Anderson.

The atmospheric seeing, or wavefront distortion due to air motion, causes random errors in the surface measurement. Air has refractive index variations proportional to density, thus temperature fluctuations. If a mass of cold, dense air floats over the mir-

ror during a test, the test wavefront will be distorted and the measurement of the surface will indicate a low area on the mirror. The tendency to form these air masses is minimized by using a large lab with well-mixed air and minimal heat (or cold) loading. Eliminating the seeing problem by performing the test in a vacuum chamber[15,16] would be extremely expensive and difficult to implement for large mirrors.

An important point demonstrated by Martin *et al.*[17] is that the random testing errors are distributed where the mirror specification has room for them. The mirror specification allows larger errors at low spatial frequency than high frequency. The random testing errors tend to have mainly low frequency variation while the final mirror surface has very little large-scale variation. The combination of the surface errors at small scales and the measurement errors at large scales easily meets the telescope requirements.

The random seeing averages out, but there may also be systematic density variations that would lead to erroneous measurements. Once the air handlers in the room are turned off, any warm air rises creating a stable vertical gradient. Also, a heat source on one side of the room will cause a stable horizontal density gradient. The effect of the horizontal gradient is measured by rotating the mirror, but there is no such test for the vertical gradient.

The vertical stratification of the air causes a focal length change and a small amount of spherical aberration or change in conic constant. To quantify the effect of a vertical gradient, a computer simulation of the null test was performed, modeling the refractive index gradient of the air using discrete steps. The null test for the 6.5-m $f/1.25$ primary was simulated, setting the number of steps to be large enough that a further decrease in step size did not change the result. Assuming a perfect null corrector at the correct spacing, the resulting power and spherical aberration cause a change in the primary radius R and conic constant K of

$$\Delta K \cong -3.5 \cdot \Delta n$$
$$\frac{\Delta R}{R} = \frac{\Delta n}{2} \qquad (2)$$

where Δn = total refractive index difference (mirror to null lens).

The temperature at SOML was measured to have a variation of about 0.5° C from the tower to the shop floor. Since the refractive index of air changes by 1.0×10^{-6} per °C[18], the temperature gradient at SOML causes a conic constant error of less than 2 ppm (parts-per-million) and a radius error of less than 0.3 ppm. Even if this effect was several times more severe, it would remain negligible compared to the null corrector uncertainty of 80 ppm.

A different thermal effect is possible where the deep dish formed by the fast primary mirror holds a stable layer of cool air. A ray-trace simulation of this effect leads to

$$\Delta K \cong -4\Delta n$$
$$\frac{\Delta R}{R} = \Delta n \qquad (3)$$

where Δn is the refractive index of the air held in the mirror. This effect is minimized by allowing air to flow through the center hole of the mirror.

3. NULL CORRECTOR FOR FIGURE MEASUREMENTS USING INFRARED LIGHT

An infrared null corrector has been fabricated that uses germanium and ZnSe lenses with a single diamond-turned aspheric surface. The null corrector, shown in Fig. 5, consists of three lenses: an aspheric ZnSe diverger, a plano-convex germanium relay lens, and a plano-convex ZnSe field lens. The optical design uses the aspheric surface to give a near-perfect wavefront error of 0.0014 λ rms and mapping error less than 1.3%. The aspheric surface for this null corrector was diamond turned and measured with a profilometer. The surface deviates from the best-fit sphere by 160 μm and was determined to be correct to ±0.2 μm. The null corrector will be mounted horizontally and aligned to the collimated output from a Twyman-Green interferometer. The interferometer uses a CO_2 laser operating at 10.6 μm, a PZT-shifted reference mirror, and a pyroelectric vidicon detector.[19] The

relative alignment between the system and the primary mirror will be performed by translating the interferometer-null corrector in three directions and steering the beam with a fold flat. The fold flat is positioned 2/3 of the distance from the paraxial to the marginal focus, so tilting the mirror causes a change in pure Zernike coma.

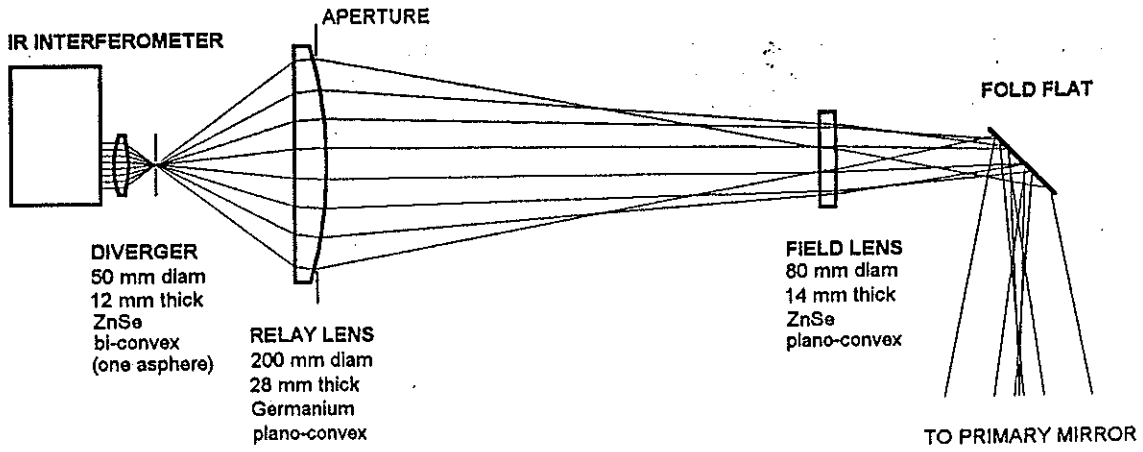

Figure 5. Infrared null corrector for the testing of a 6.5-m *f*/1.25 paraboloidal primary mirrors. This design is optimized for wavefront correction, imaging distortion, alignment tolerances, and ghost reflections.

This null corrector was designed to give excellent imaging performance with no troublesome ghost reflections. In order to avoid the diffraction problems associated with infrared interferometry, the image of the primary mirror is carefully focused onto the vidicon detector. To facilitate this, the null corrector creates a real image of the primary mirror very near the large relay lens, where a circular aperture will be accurately placed to provide a sharp aperture to define the focus. To minimize ghost reflections, the null lens was designed to avoid surfaces with near-normal ray incidence.

The elements in this null lens are the smallest that will work when aligned to machine tolerances (±50 μm over 200 mm). The lenses were carefully made free of wedge so that they can be mounted in a simple accurately machined cell for alignment and spacing. A thorough tolerance analysis of the system indicates that the null lens will contribute surface measurement errors of 1.5 μm rms. Most of this error is due to refractive index inhomogeneity of the large germanium lens. The uncertainty of the conic constant in this null lens due to the manufacturing tolerances is ±0.00016, nearly meeting the final telescope specification of ±0.0001. We plan to check the quality of the entire null lens assembly with a computer-generated hologram.

4. NULL CORRECTOR FOR FIGURE MEASUREMENTS USING VISIBLE LIGHT

4.1 OPTICAL DESIGN

A visible null corrector with a sophisticated imaging system is being built for measuring the 6.5-m *f*/1.25 primary mirrors. The interferometer uses a frequency doubled YAG laser operating at 532 nm, a PZT-shifted Shack cube interferometer, imaging optics, and shuttered CCD detector. The Shack cube, null lens, and imaging optics will be precisely aligned on a single rigid truss. The laser light will be fed into the system through a single mode optical fiber.

The Shack cube interferometer[20] is used because of its simplicity and ease of alignment. The Shack cube, shown in Fig. 6, is fabricated with a small pinhole at the center of curvature of the reference surface. The mechanical alignment of the cube to the null corrector requires only that this one spherical surface be in the cor-

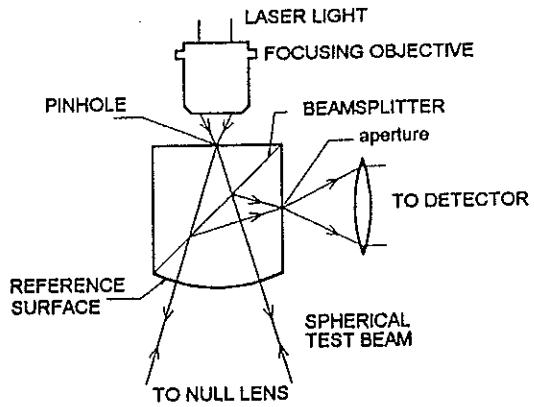

Figure 6. The Shack cube interferometer.

rect place. The interferometer is phase shifted by driving the cube and objective with PZT actuators.[21] The Shack cube and null corrector are easily integrated into a single rigid unit.

The null corrector shown in Fig. 7 consists of the Shack-cube and three BK7 lenses: a relay lens, and two field lenses. The optical design gives a wavefront error of 4 nm rms (Fig. 7) and maximum mapping error of almost 5%. The null corrector will be mounted vertically to precise tolerances using the method described by West *et al.*[22] The relative alignment between the system and the mirror will be performed by translating the entire unit in three directions and rotating about two flex-pivot axes. As in the IR test, the lateral rotation is performed about an axis 2/3 of the way from paraxial to marginal focus to decouple wavefront tilt from the alignment. The test alignment will be controlled from a remote testing station.

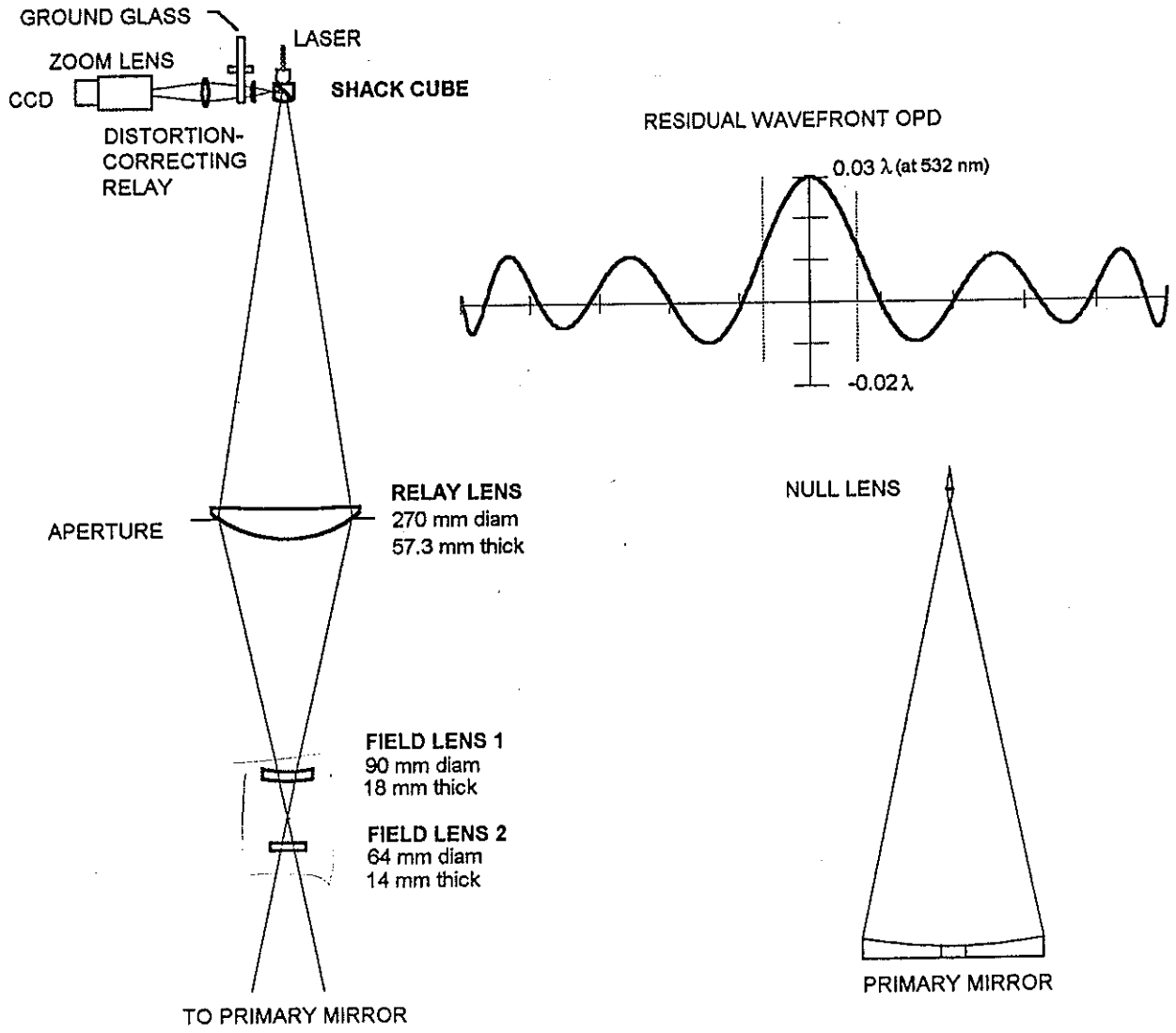

Figure 7. Optical layout of the visible null lens for 6.5-m *f*/1.25 primary mirrors with Shack cube interferometer and distortion-correcting relay. The insets show the residual wavefront and the scale of the null lens with the 6.5-m mirror.

The imaging distortion induced by the null lens is corrected with the relay optics that are shown in Fig. 7. A plot of the mapping error is shown in Fig. 8. This two-lens relay not only corrects the mapping error, but it projects the image of the primary to infinity. This allows the use of a standard zoom lens to re-image the pupil at varying magnification. The re-imaging system consists of a 6X zoom lens fixed to the CCD camera that is mounted on a tip-tilt stage. All of the controls will be operated remotely to allow the optician to magnify the image and to look with increased resolution anywhere on the mirror. High resolution (~6 mm pixels at the mirror) will then be attained for sub-aperture testing without increasing the array size.

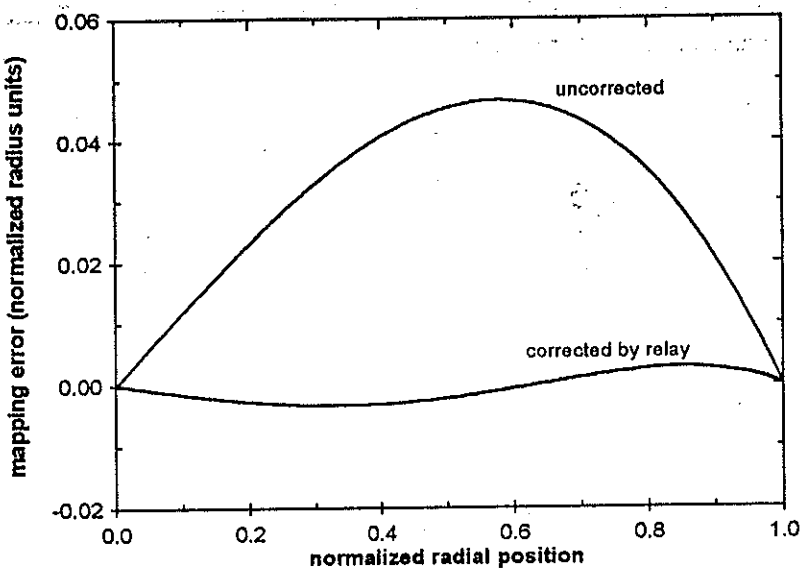

Figure 8. Mapping error for the null lens for testing the 6.5-m *f*/1.25 primary mirror.

4.2 FABRICATION OF VISIBLE NULL CORRECTOR

The lenses, which are made from H5 quality BK7 glass (from Ohara and Schott), are being figured to high quality at Steward Observatory. The spherical surfaces are measured using phase shifting interferometry and the radii are measured using a Fizeau interferometer and lens bench. The lenses are fabricated and measured to a few microns, then the spacings are re-optimized based on the as-fabricated lens dimensions.

The fast surface of the relay lens is measured using a test plate with an interesting illumination scheme shown in Fig. 9. The concave test plate is measured using a Fizeau interferometer with an *f*/0.6 diverger. The diverger reference surface quality is determined by measuring a precision ball at many rotation angles. The convex surface of the relay lens is then measured with this test plate using the Fizeau and diverger only for illumination and imaging. An imaging element is fit to the relay lens with the outer surface nearly concentric with the test plate. For the relay lens measurement, there are four nearly concentric surfaces. To avoid spurious fringes, the Fizeau reference and the imager surface are tilted and the reflections from these surfaces are blocked. The test plate is pushed and phase shifting interferometry is used to allow a high resolution measurement.

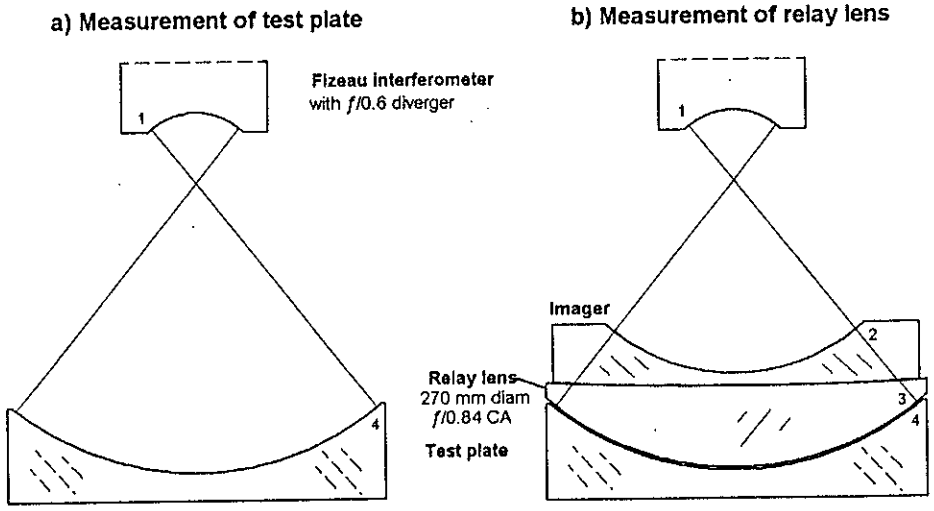

Figure 9. Measurement of the fast convex surface on the relay lens using a test plate. a) The concave test plate is measured using a Fizeau interferometer. b) The fast convex surface (3) is measured against the test plate (4). For this measurement, surfaces 1 and 2 are tilted so the reflections from these surfaces can be blocked.

The performance of the null test requires accurate and stable alignment of the lenses. The alignment procedure used at Steward Observatory for null correctors for highly aspheric mirrors is described by West *et al.* (1992). Using this method, the null lens is aligned onto an Invar frame that provides stability and rigidity. The entire null lens is rotated about a precisely maintained axis and the runout (or wobble) of each surface is mechanically measured and reduced to less than 5 μm. The spacings between the elements are measured using special metering rods and set to an accuracy of about 3 μm. The rigid assembly is mounted to a set of stages that provide translation in *x*, *y*, and *z* and rotation about the lateral axes for alignment to the primary mirror. A layout of a previously built null corrector for a 3.5-m mirror is shown in Fig. 10.

The null corrector for the 6.5-m mirrors will be much stiffer that those for the 3.5-m mirrors to reduce problems with vibration. It will be supported at a stiff point in the test tower for the same reason. Additionally, we are also pursuing two methods of testing in the presence of vibration: using a fast camera to take the data quickly enough to freeze out the vibration, and an active fringe tracker.

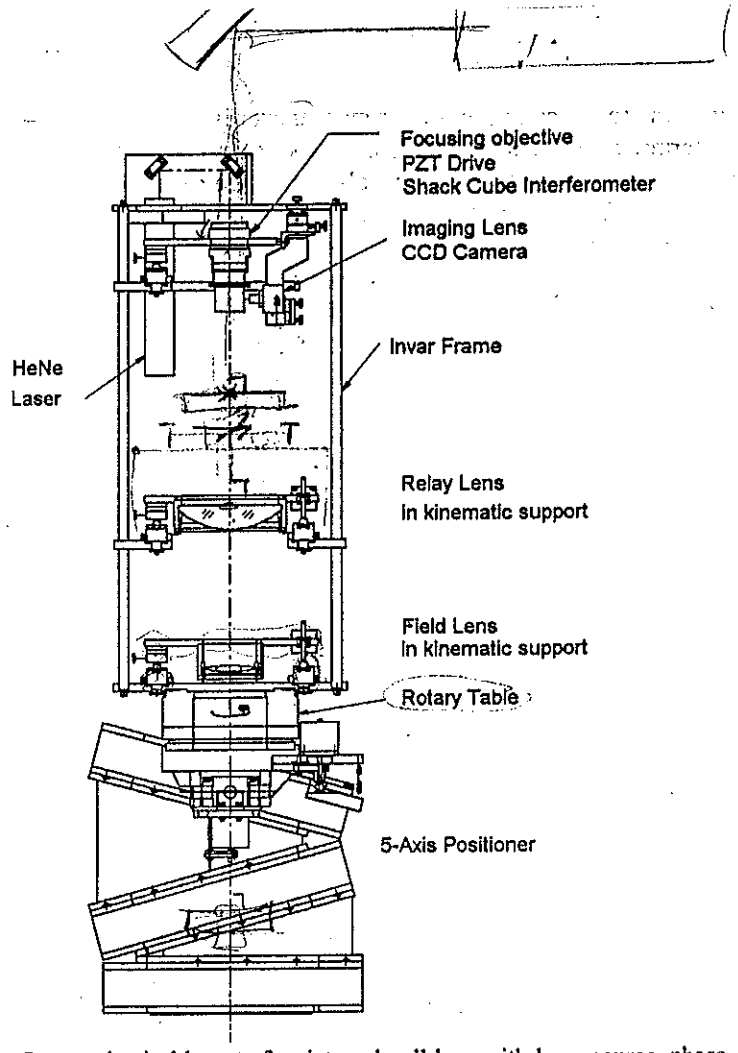

Figure 10. Optomechanical layout of an integral null lens with laser source, phase shifting Shack cube interferometer, imaging system, and 5-DOF positioner. Drawing by D. Murguic.

4.3 TOLERANCE ANALYSIS

Since the null corrector is used as a reference for fabricating the primary mirrors, a thorough tolerance analysis is required to determine the expected accuracy of the test. In this analysis, a table of sensitivities is created showing the performance degradation for small null lens errors, as determined by computer simulation. The effects of the surface figure irregularity and refractive index inhomogeneity are calculated directly (See Table 1). For small errors, the system degradation is assumed to vary linearly with the errors. The sensitivities are then multiplied by expected errors to compute the degradation in system accuracy. This information was used to adjust the tolerances based on the fabrication and alignment process and the required system performance.

Table 1. Contribution to wavefront from surface figures and index inhomogeneity.

Source	Amount	Typical value	Wavefront contribution (rms)
Shack cube rms surface irregularity	ΔS_{SC}	6 nm	$2\ \Delta S_{SC}$
Lens rms surface figure	ΔS_L	8 nm	$2\ (n\text{-}1)\ \Delta S_L$
Lens rms index inhomogeneity	Δn	0.12×10^{-6}	$2\ \Delta n \times$ *thickness*

Since the specification on the primary mirror is in terms of structure functions,[23] the error analysis of the null corrector also uses the functions. The tolerance analysis of the interferometric test was performed by computing structure functions for all of the independent parameters in the system and adding them[1]. Structure functions derived from direct dimensions (spacings, curvatures, refractive index, misalignments, etc.) were computed by ray-trace simulation and analysis of the system. Structure functions from the surface figures of the optical elements were estimated using data from finished optical surfaces. Refractive index inhomogeneity structure functions were estimated for H5 quality glass using melt data and assuming a linear dependence of rms phase difference on point separation. The structure functions from all parameters in the null test are added to give the total test optics structure function. The analysis does not take into account the ability to measure and remove errors in the null lens using the CGH null lens test.

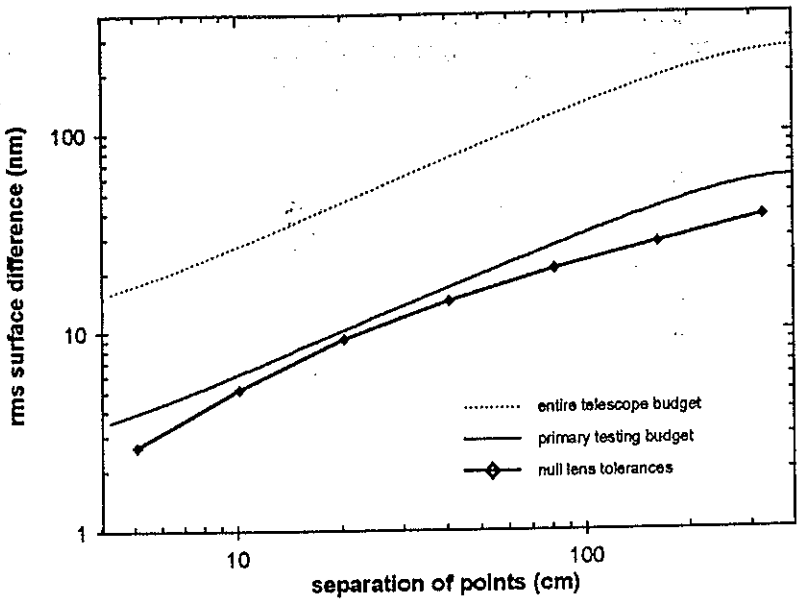

Figure 11. Structure function from the error analysis of the visible null corrector for the 6.5-m *f*/1.25 primary. The telescope and test optics specifications are based on a tilt-corrected Kolmogorov model of the atmosphere with a relaxation at small spatial scales.

The telescope error budget allots primary mirror testing a structure function corresponding to r_0 of 270 cm with 0.04 arc-sec FWHM atmospheric seeing. The tolerance analysis shows that the null corrector will meet this at all spatial scales, with a net uncertainty in the measurement of 21 nm rms. The resulting structure function for the null lens optics is shown in Fig 11.

Distinct from the structure function requirement is a tolerance on the conic constant of the primary. The null lens described introduces an uncertainty of the conic constant of ±0.00009. Also, the analysis does not take into account the ability to measure and remove errors in the null lens using a rotation test or the CGH null lens test.

5. NULL CORRECTOR CERTIFICATION WITH COMPUTER-GENERATED HOLOGRAMS

However apparently well made, there is always a small possibility that the null correctors can be flawed. If undetected, a null corrector error would result in the final shape of the mirror being incorrect. Two recent telescopes had their primary mirrors made to the wrong shape because of errors in the null correctors -- the Hubble Space Telescope[24] and the New Technology Telescope.[25] If accurate testing of the null correctors had been performed, the errors would have been discovered and corrected in the shop. Instead, the errors were not discovered until the finished mirrors were in their telescopes on a mountain top or in orbit.

An optical test using computer-generated holograms is planned to test and qualify the null correctors for the 6.5-m primary mirrors. The technique employs a rotationally symmetric computer-generated hologram (CGH) that tests the null corrector directly by synthesizing a wavefront that would be returned by a perfect primary mirror. The test, which is quick and highly accurate, has been demonstrated on null correctors for two 3.5-m primary mirrors[1,26].

5.1 DESCRIPTION OF CGH TEST OF NULL LENS

In the CGH null lens test, a custom manufactured hologram is illuminated by the laser light from the null lens. The hologram is made so it will diffract light back into the null corrector to appear as if it were a perfect primary mirror. The test is insensitive to alignment errors and uses no optics other than the hologram. Since the null corrector and CGH are fabricated independently, agreement between the two indicates a high probability that both are correct.

The hologram is simply a circular grating or zone plate fabricated onto a flat glass substrate. The CGH for the visible null test is fabricated using electron beam lithography that has been developed for the production of integrated circuits. The final hologram will be a relief grating with quarter-wave deep grooves and will be used at third order. The infrared hologram will be made using a less accurate and less-expensive optical writer. This CGH will use chrome rings on bare glass and be used at first order. For both tests, the required spacing of the rings is determined by the mirror surface that the hologram replaces and the laser wavelength. The groove depth and ring width are optimized to minimize fabrication costs, while giving the correct intensity of the diffracted light.

A layout of the CGH null test, shown in Fig. 12, depicts the null lens and CGH. No modifications are made to the null lens to perform this test. The null corrector tests the hologram exactly as if a real mirror was being measured.

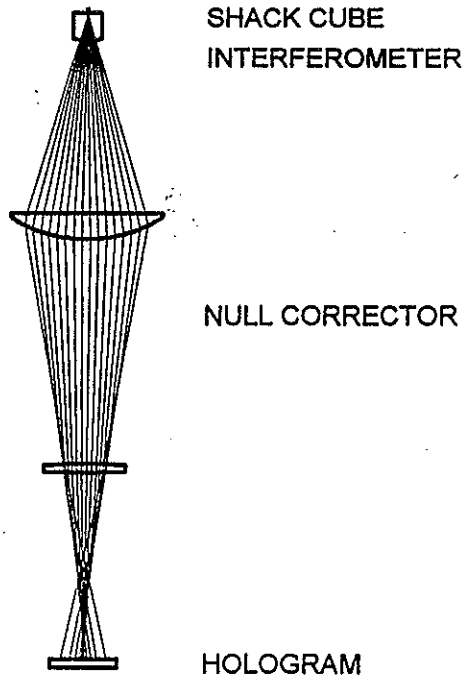

Figure 12. Layout of CGH test of null lens. The use of the CGH involves simply positioning the hologram at the correct location and making the measurement as if the mirror itself was being tested.

5.2 HOLOGRAM FABRICATION

The CGH null lens test is planned for all of the telescope projects at Steward Observatory. The computer-generated hologram for visible testing will be 136 mm in diameter and will consist of 12797 grooves, spaced as small as 4 μm. This is within the realm of existing lithographic technology, but it will be difficult and expensive to fabricate. This hologram will be directly e-beam written on the final substrate that is 7 inches square and 0.25 inches thick. This substrate will be polished flat to λ/10 as it is supported on a master flat. An error budget for this test indicates a measurement accuracy of ±40 ppm for the conic constant.[1]

A prototype of this hologram will be fabricated before the full CGH is made. This prototype, consisting of only a narrow diametrical slice across the circular hologram, will allow a test of the fabrication technique that requires only a small fraction of the cost of the full hologram. This diametrical slice will be useful for measuring spherical aberration in the null lens.

The accuracy requirements on the infrared hologram are not so severe, allowing it to be written on an optical writer. The infrared hologram will consist of 1928 chrome rings, with spacing as small as 13 μm. The pattern may be written using a writer developed at the Optical Sciences Center (University of Arizona) for the fabrication of chrome-on-glass zone plates for measuring convex aspheres up to 12 inches across.

6. CONCLUSION

The null correctors for the 6.5-m *f*/1.25 primary mirrors represent a significant advance in the field of metrology for large astronomical optics. The ability to fabricate null correctors, even for mild aspheres, is questioned by many astronomers. We have developed the techniques for designing, analyzing, fabricating, and certifying instruments for interferometric measuring large, fast primary mirrors. These null test instruments will provide rapid, accurate surface measurements to enable efficient stressed-lap figuring of the most challenging primary mirrors in the history of astronomy.

REFERENCES

1 J. H. Burge, *Advanced Techniques for Measuring Primary Mirrors for Astronomical Telescopes*, Ph. D. Dissertation, Optical Sciences, University of Arizona (1993).

2 A. Couder, "Procédé d'examen d'un miroir concave non-sphérique," Rev. Opt. Theor. Instrum., 6,49-55 (1927).

3 H. E. Dall, "A null test for paraboloids," J. Br. Astron. Assoc. **57**, 201-205 (1947).

4 F. E. Ross, "Parabolizing mirrors without a flat," Astrophys. J. **98**, 341-346 (1943).

5 A. Offner, "A null corrector for paraboloidal mirrors," Appl. Opt **2**, 153-155 (1963).

6 R. T. Holleran, "An algebraic solution for the small lens null compensator," Appl. Opt. **7**, 137-144 (1968).

7 D. T. Puryayev. and N. S. Shandin, "Design of lens compensators for testing the concave astronomical mirrors of large telescopes," Sov. J. Opt. Technol. **46**, 207-209 (1979).

8 J. R. Moya. and J. E. A. Landgrave, "Third-order design of refractive Offner compensators,"Appl. Opt. **26**, 2667-2672 (1987).

9 J. M. Sasian, "Design of null lens correctors for the testing of astronomical optics," Opt. Eng. **27**, 1051-1056 (1988).

10 J. M. Sasian, "Optimum configuration of the Offner null corrector: testing an F/1 paraboloid," in *Surface Characterization and Testing II*, J. E. Greivenkamp and M. Young, eds., Proc. SPIE **1164**, 8-17 (1989).

11 C. E. DeVoe, "Limitations on aspheric surface testing with simple null correctors," Master Thesis, Optical Sciences Center, University of Arizona, Tucson, AZ (1989).

12 A. Offner, and D. Malacara, "Null tests using compensators," in *Optical Shop Testing*, D. Malacara, ed., (Wiley, New York, 1992) pp. 427-454.

13 D. Shafer, "Null lens design techniques," Appl. Opt. **31**, 2184-2188 (1992).

14 L. A. Selberg, "Interferometer accuracy and precision," in *Metrology; Figure and Finish*, B. Truax, ed., Proc. SPIE **749**, 8-18 (1987).

15 R. J. Wollensak and C. A. Rose, "Fabrication and test of 1.8-meter (71-inch) diameter, high-quality U.L.E.™ mirror," *The Space Telescope*, NASA SP-392, 123-134 (1976).

16 T. A. Facey, A. L. Nonnenmacher, D. P. Chadwick, "Fabrication of large aperture mirrors for astronomical telescopes," in *Advanced Technology Optical Telescopes IV*, L. D. Barr, ed., Proc. SPIE **1236**, 597-604 (1990).

17 H. M. Martin, J. H. Burge, and S. C. West, "Environmental effects in the testing of large astronomical mirrors," in *Precision Interferometric Metrology* (The American Society for Precision Engineering, Raleigh NC, 1992) Proc. ASPE **5**, pp. 72-75

18 B. Edlén,"The refractive index of air," Metrologia **2**, 71-80 (1966).

19 H. P. Stahl. and D. Ketelsen, "Aspheric figure generation using feedback from an infrared phase-shifting interferometer," in *Large Optics Technology*, G. M. Sanger, ed., Proc. SPIE **571**, 22-29 (1985).

20 R. V. Shack. and G. W. Hopkins, "The Shack interferometer," Opt. Eng. **18**, 226-228 (1979).

21 C. L. Koliopolis and D. S. Anderson, "High resolution phase measurements of optical surfaces," in *Ultraprecision Machining and Automated Fabrication of Optics*, D. L. Decker and R. A. Jones, eds., Proc. SPIE **676**, 90-93 (1986).

22 S. C. West, J. H. Burge, R. S. Young, D. S. Anderson, C. Murguic, D. A. Ketelsen, and H. M. Martin, "Optical metrology of two large highly aspheric telescope mirrors," Appl. Opt. **31**, 7191-7197 (1992).

23 J. M. Hill, "Optical design, error budget, and specifications for the Columbus Project Telescope," in *Advanced Technology Telescopes IV*, L. D. Barr, ed., Proc. SPIE **1236**, 86-107 (1990).

24 L. Allen, J. R. P. Angel, J. D. Mongus, G. A. Rodney, R. R. Shannon, C. P. Spoelhof, "The Hubble Space Telescope oprical systems failure report," NASA Report. Nov., 1990.

25 R. N. Wilson, F. Franza, L. Noethe, and G. Andreoni, "Active optics IV. Set up and performance of the optics of the ESO New Technology Telescope (NTT) in the observatory," J. Mod. Optics **38**, 219-243 (1991).

26 J. H. Burge, "Certification of null correctors for primary mirrors," in *Advanced Optical Manufacturing and Testing IV*, J. Doherty, Editor, Proc. SPIE **1994**, 248-259 (1993).

MMTHeNe Hologram
(Description of fabrication process)

1. Substrate:

Diameter - 151 mm
Thickness - 21 mm
Quality - see Figure 1

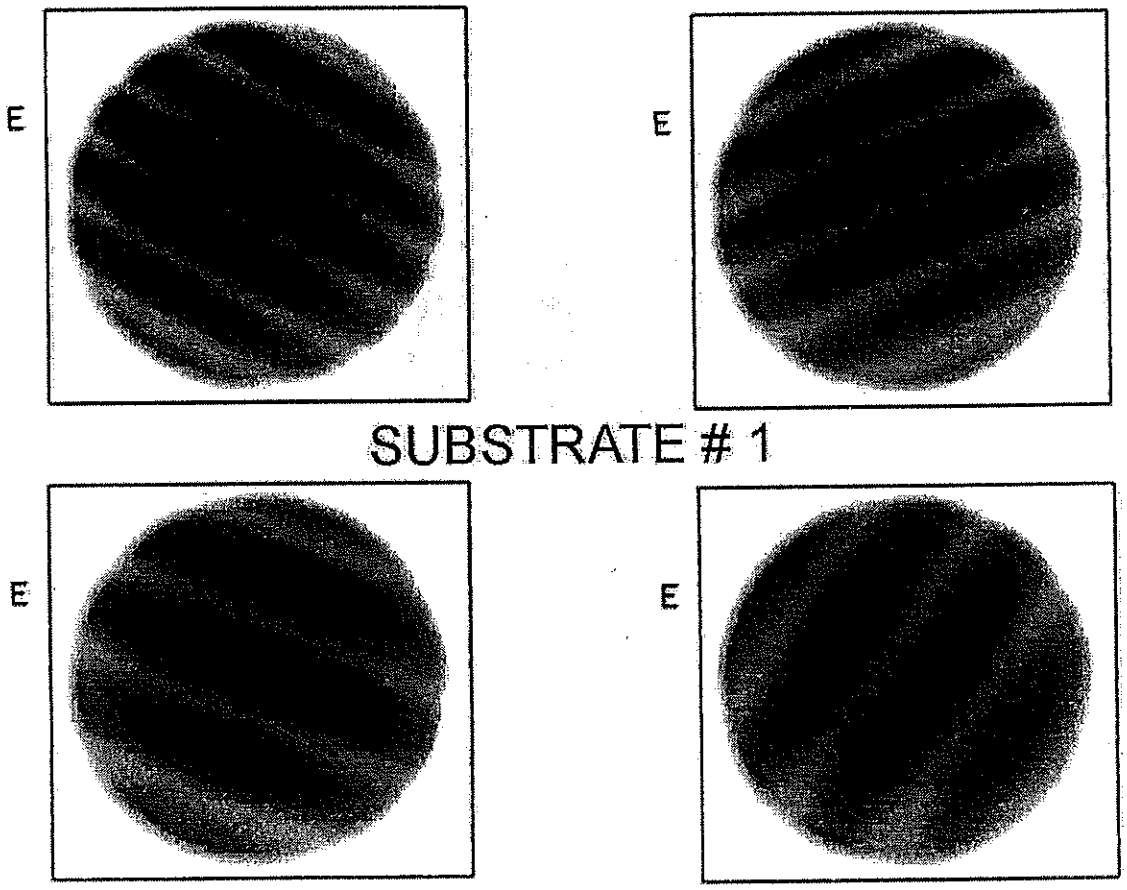

Figure 1. Interferograms (Zygo) of 145 mm working field of substrate with chromium film.

2. Hologram composition.

1.	Test rings for centering:	R_{min} =0 μm,	R_{max} = 30 μm
2.	Zone plate structure (MMTHENE.DAT):	R_{min} =51.08 μm,	R_{max} = 67996.28 μm
3.	Mark of ruler direction, see letter "R":	R_{min} = 68100 μm,	R_{max} = 68200 μm
4.	Test 1 μm ring (MMTRING.DAT):	R_{min} =68500μm,	R_{max} = 68501 μm
5.	Caption (MMTHENE.TXT):	R_{min} =69000 μm,	R_{max} = 70000 μm
6.	Power tests: #1 (usual, rings)	R_{max} =70150 μm (P_{max}=1000, P_{step}=20, Pitch=1.6 μm)	
	#2 (photoelectric)	R_{max} =70300μm	

3. Writing conditions.

Laser interferometer wavelength (in vacuum) - 632.990989 nm /tested by Iodine sell/
Temperature - 17.9 C°.
Air pressure - 1003 Pa.

Time of main zone plate writing - 6 hours.

4. Center.

Ring with 30 μm diameter was used for aligning all structures of hologram.

5. Ruler.

A ruler was written directly before of the main zone plate writing. Value of a scale division is 5 mm. The size of ruler graduation lines areas- 10 x10 μm. Time of ruler writing was about 1 min.

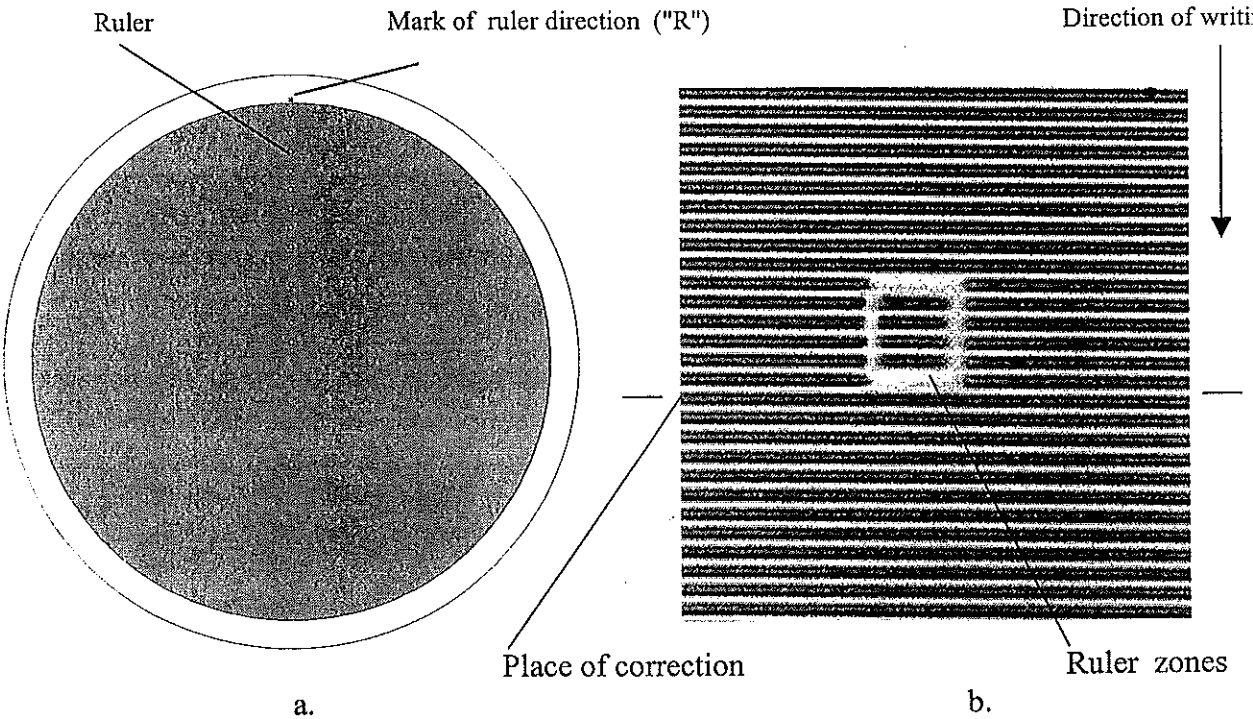

Figure 2. Ruler location (a) and fragment of microphotograph (b) of graduation lines area

6. Periodical correction of radial coordinate at main zone plate writing.

Periodical corrections were made each 5 mm of writing on radial direction. Corrections were made after writing the ruler graduation lines areas.

Periodic correction data (μm):

Center shift=-0.106104 R=64998.70896
Center shift=-0.090036 R=59998.245427
Center shift=-0.039557 R=54997.940098
Center shift=-0.085879 R=49997.634769
Center shift=-0.047216 R=44997.448094
Center shift=-0.074193 R=39997.221867
Center shift=-0.034966 R=34998.063524
Center shift=-0.032385 R=29997.006722
Center shift=-0.023705 R=24997.373764
Center shift=-0.085339 R=19997.661704
Center shift=-0.027825 R=14997.751887
Center shift=-0.006127 R=9995.192138
Center shift=-0.048754 R=4996.547961

Center shift=-0.026891 R=0

7. **Trajectory of rotation.**

Trajectory of spindle rotation was measured before writing process.

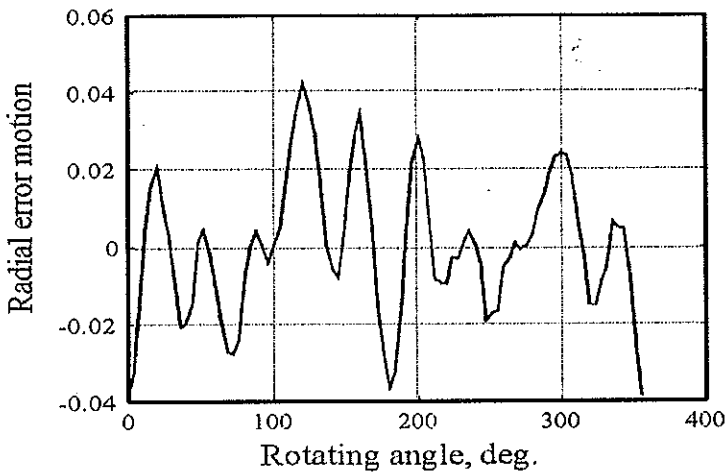

Figure 3. Trajectory of spindle rotation. Radial errors are no more 0.04μm.

Alexander Poleshchuk

Laboratory of Laser Technology,
Institute of Automation and Electrometry
SB RAS, Novosibirsk 630090, Russia
Phone: +007 3832 333091
e-mail: alexp@okibox.iae.nsk.su